UNIVERSITY OF CALIFORNIA

Los Angeles

Elucidating the role of Zinc-finger protein 36 in endothelial angiogenic response

A dissertation submitted in partial satisfaction of the requirements for the degree Doctor of Philosophy in Molecular, Cellular and Integrative Physiology

by

Hannah Louise Sunshine

2023

ABSTRACT OF THE DISSERTATION

Elucidating the role of Zinc-finger protein 36

in endothelial angiogenic response

by

Hannah Louise Sunshine

Doctor of Philosophy in Molecular, Cellular and Integrative Physiology

University of California, Los Angeles, 2023

Professor Thomas Aguiar Vallim, Co-Chair

Professor M. Luisa Iruela-Arispe, Co-Chair

Throughout the vascular tree, endothelial cells function as the interface between circulation and underlying tissues. They act not only as gatekeepers but are also designed to gauge and adapt to circulating factors for regulation of vascular tone, development, and repair. The severity of many diseases, such as cardiovascular disease and diabetes, hinge on endothelial function and the ability to initiate vascularization of hypoxic tissues. Vascular morphogenesis requires a delicate molecular gradient of Notch signaling in endothelial cells to pattern correct angiogenic sprouting. This process is controlled, at least in part, by the distribution of ligands (Dll4 and Jagged1). How Jagged1 (Jag1) expression is compartmentalized in the vascular plexus remains unclear. Understanding the molecular regulators for this process can help our understanding of drivers toward endothelial dysfunction.

Here, we showed that mRNA decay protein Zinc-finger protein 36 (ZFP36) is robustly induced *in vitro* in various human primary endothelial cells (ECs) downstream of canonical vascular endothelial growth factor (VEGF) signaling. This induction, observed at the mRNA and protein level, is uniquely specific to ZFP36 and not shared by other family members ZFP36L1 nor

ZFP36L2, which have already been linked to vascular development. This induction was also observed to be primarily facilitated through VEGF receptor 2 (VR2) as receptor inhibition blunted ZFP36 induction. We identified *Jag1* mRNA as direct target of zinc finger protein 36 (ZFP36) via crosslinking-immunoprecipitation and verified conserved Jag1 regulation in human primary ECs. Human ECs lacking *ZFP36* achieved with CRISPR KO, displayed high levels of JAG1 and increased angiogenic sprouting *in vitro*. Similarly, in mice with tamoxifen induced endothelial specific vascular endothelial-cadherin Cre-mediated KO of *Zfp36,* endothelial cells displayed mispatterned and increased levels of JAG1 in the developing retinal vascular plexus. Abnormal levels of JAG1 at the sprouting front altered Notch1 signaling, increasing the number of tip cells; a phenotype that was rescued by crossing the EC specific *Zfp36* KO with *Jag1* KO mice to achieve haploinsufficiency of *Jag1*.

Additionally, we tested the significance of ZFP36 induction in the broad context of molecular drivers of endothelial plasticity: metabolism, kinase signaling, and shear stress. We were unable to confirm several metabolic targets identified in mouse embryonic fibroblasts (MEFs) in our human primary ECs *in vitro*. However, conserved sensitivity to changes in kinase activity, confirmed through inhibitor studies, suggests that these discrepancies in targets could be a result of cell specific targets for ZFP36 mRNA binding and regulation. Microenvironment can further play a role in ZFP36 mediated endothelial transcript regulation as we show that shear stress is able to suppress overall ZFP36 expression.

Our findings reveal an important feedforward loop, whereby VEGF stimulates ZFP36, consequently suppressing *Jag1* to enable adequate levels of Notch signaling during sprouting angiogenesis.

The dissertation of Hannah Louise Sunshine is approved.

Heather R. Christofk

Peter John Tontonoz

Thomas Aguiar Vallim, Committee Co-Chair

M. Luisa Iruela-Arispe, Committee Co-Chair

University of California, Los Angeles

2023

To my beloved family near and far.

To my love.

TABLE OF CONTENTS

LIST OF FIGURES

LIST OF TABLES

ACKNOWLEDGMENTS

I would like to thank Dr. Luisa Iruela-Arispe for her mentorship and guidance throughout my Ph.D. journey. Your enthusiasm for even my smallest accomplishments and your support during personal crises helped me persevere through my most difficult days.

I would like to thank my committee co-chair and members, Dr. Thomas Vallim, Dr. Heather Christofk and Dr. Peter Tontonoz. Your insightful critiques, feedback, and collaborations have propelled this project forward in immense ways. I appreciate all the time you have devoted to helping me shape my thesis work.

Thank you to all the Arispe lab members for giving me a sense of family while mine were far away.

I would also like to thank my husband Andrew Fields and the rest of my family, who supported my dream of pursuing my Ph.D. and kept me grounded during every high and low. I could not have done this without them.

Chapter 2 and 3 were adapted from Sunshine et al (2023, in press) “Endothelial Jagged1 levels and distribution are post-transcriptionally controlled by ZFP36 decay proteins.” We would like to thank the Broad Stem Cell Research Center (BSCRC) and Jonsson Comprehensive Cancer Center (JCCC) at UCLA for sequencing libraries, Feinberg School of Medicine, and the Robert H. Lurie Comprehensive Cancer Center (RHLCCC) and associated core facilities at Northwestern University (supported by the Cancer Center Support grant NCI CA060553): the Mouse Histology and Phenotyping Core, RHLCCC Flow Cytometry Facility, and the Center for Advanced Microscopy. A special thanks to Michelle Steel and Snezana Mirkov for managing animal colonies and for assistance with husbandry and animal experiments. We thank the members of the Arispe lab and the Feinberg Cardiovascular and Renal Research Institute at Northwestern University for extensive discussions. CS was supported by the Lurie Cancer Center AP Capstone High School Research Program and efforts were generously and tirelessly

facilitated by CPS teacher Gerry Gonzalez. This work was supported by grants from the National Institutes of Health to MLIA (R35HL140014). Additional funding to HLS was provided by support from Ruth L. Kirschstein National Research Service Awards (GM007185 & T32HL069766) and Whitcome Pre-doctoral Fellowship in Molecular Biology (UCLA).

Chapter 4 is unpublished data. It reflects work performed primarily by Hannah Sunshine. We thank the members of the Arispe lab and the Feinberg Cardiovascular and Renal Research Institute at Northwestern University for extensive discussions. A special thanks to Dr. Arthur Prindle for access to Seahorse XF96 instrumentation and Giangela Stokes for assistance with lambda phosphatase assay validation. This work was also supported by grants from the National Institutes of Health to MLIA (R35HL140014) and additional funding to HLS provided by support from Ruth L. Kirschstein National Research Service Awards (GM007185 & T32HL069766) and Whitcome Pre-doctoral Fellowship in Molecular Biology (UCLA).

VITA

Education

University of California, Los Angeles – Los Angeles, CA

PhD Candidate, *Molecular*, *Cellular*, *and Integrative Physiology* — Sept 2015 – present

California State University, Fullerton – Fullerton, CA

BS, *Cellular and Developmental Biology - magna cum laude* — Aug 2007 - May 2012

Honors and awards

Ruth L. Kirschstein National Research Service Award (T32HL069766)	2019 - 2022
Whitcome Pre-doctoral Fellowship in Molecular Biology	2017 - 2018
Ruth L. Kirschstein National Research Service Award (GM007185)	2016 - 2017
Dean's List – CSU, Fullerton	2007 - 2012
Minority Health and Health Disparities International Research Training Program	2011

Employment & professional activities

North American Vascular Biology Organization, *Member*	2022 - present
American Heart Association, *Member*	2019 - 2020
Association for Multi-Ethnic Bioscientists' Advancement (AMEBA), *Member*	2018 - 2019
UCLA Entering Mentoring Training Program, *Certification*	2017
Advancing Women in Science and Engineering (AWiSE), *Member*	2015 - 2019
Prodo Laboratories/Scharp Technologies, *Research Associate II*	2012 - 2015

Teaching Experience

University of California, Los Angeles – Los Angeles, CA — Fall 2017, Fall 2018

Teaching Assistant, Biology of Cells (MCDB 165A)

Research Mentorship

Chloe Symons (Capstone scholar)	June 2022 – April 2023
Jack Li (MSTP)	Summer 2022
Giangela Stokes (Graduate)	Spring 2022
Lenore Yalom (Graduate)	Spring 2020
Winnie Liu (Undergraduate)	Jan 2018 – March 2019
Max Yang (Undergraduate)	Aug 2017 – Jan 2018

Conference Presentations

Northwestern Cell & Developmental Biology Departmental Retreat – Chicago Botanical Gardens, Glencoe, IL – Sept 21, 2023

22nd International Vascular Biology Meeting (IVBM) – Oakland, CA – Oct 13-17, 2022

Northwestern Cell & Developmental Biology Departmental Retreat –Chicago, IL – Oct 4-5, 2022

Gordon Research Seminar and Conference – Notch Signaling in Development, Regeneration and Disease - Bates College, Lewiston, Maine – July 16-22, 2022

Chicago Regional Cardiovascular Research Symposium – Loyola University, Chicago, IL - March 2022 – *Awarded prize for excellent poster*

16th Annual Lewis Landsberg Research Day – Chicago, IL - Nov 2021

UCLA Molecular, Cellular, and Integrative Physiology Annual Retreat – Malibu, CA – Feb 9, 2019

UCLA Cardiovascular Symposium - Los Angeles, CA – October 2018

Publications

Sunshine, H.L., Cicchetto, A.C., Kaczor-Urbanowicz, K.E., Ma, F., Pi, D., Symons, C., Turner, M., Shukla, V., Chrisofk, H.R., Vallim, T.A., Iruela-Arispe, M. L. Endothelial Jagged1 levels and distribution are post-transcriptionally controlled by ZFP36 decay proteins. Cell Rep – *in press*

Cicchetto, A.C., Jacobson, E.C., **Sunshine, H.**, Wilde, B.R., Krall, A.S., Jarrett, K.E., Sedgeman, L., Turner, M., Plath, K., Iruela-Arispe, M.L., et al. (2023). ZFP36-mediated mRNA decay regulates metabolism. Cell Rep. 42, 112411. 10.1016/j.celrep.2023.112411.

Afshar, Y., Ma, F., Quach, A., Jeong, A., **Sunshine, H.L**., Freitas, V., Jami-Alahmadi, Y., Helaers, R., Li, X., Pellegrini, M., et al. (2023). Transcriptional drifts associated with environmental changes in endothelial cells. eLife 12. 10.7554/eLife.81370.

McDonald, A.I., Shirali, A.S., Aragón, R., Ma, F., Hernandez, G., Vaughn, D.A., Mack, J.J., Lim, T.Y., **Sunshine, H**., Zhao, P., et al. (2018). Endothelial Regeneration of Large Vessels Is a Biphasic Process Driven by Local Cells with Distinct Proliferative Capacities. Cell Stem Cell 23, 210-225.e6. 10.1016/j.stem.2018.07.011.

Mack, J.J., Mosqueiro, T.S., Archer, B.J., Jones, W.M., **Sunshine, H.**, Faas, G.C., Briot, A., Aragón, R.L., Su, T., Romay, M.C., et al. (2017). NOTCH1 is a mechanosensor in adult arteries. Nat. Commun. 8, 1620. 10.1038/s41467-017-01741-8.

Sunshine, H., and Iruela-Arispe, M.L. (2017). Membrane lipids and cell signaling. Curr. Opin. Lipidol. *28*, 408–413. 10.1097/MOL.0000000000000443.

CHAPTER 1

INTRODUCTION

1.1 Endothelial plasticity and functional heterogeneity.

The vascular endothelium is the living pavement lining of the body's highways for oxygen and nutrient transport. Until the early 1970s, this innermost layer was thought to inertly act as a diffusion barrier for blood cells.[1] However, the endothelium is now considered an active organ, functioning as the body's frontline to sensing important circulating factors and acting as the first responder for regulating vascular permeability, coagulation, and blood pressure. Consequently, endothelial plasticity is necessary for pivoting the vasculature to adapt to unique tissue requirements.

Structural and functional heterogeneity in endothelial cells (ECs) is well documented throughout the vascular tree (Figure 1.1A). Arterial, venous, capillary and lymphatic endothelial cells are even more unique across tissues such as the discontinuous endothelium found in liver, with gaps to facilitate increased permeability, and the continuous endothelium of the blood brain barrier, which, in contrast, is rich in tight junctions.[2] Intrinsic epigenetics and extrinsic humoral factors, hemodynamics, and cell-cell interactions dictate these distinct phenotypes which contribute to the vast complexity of EC functional heterogeneity achieved in order to maintain tissue homeostasis and regeneration (Figure 1.1B-D).[3,4] Imbalances in any of these aspects can also negatively alter endothelial physiology and lower the threshold for disease pathogenesis. In fact, the severity of many a pathology hinges on the functionality of blood vessels.[5] Cardiovascular disease remains the leading cause of death in the United States.[6] Therefore, obtaining a better understanding of the signaling pathways involved in EC plasticity can lead to better therapeutic strategies for treating diseases with vascular pathophysiology.

In general, endothelial dysfunction is characterized by endothelial activation and the inability to regulate vascular tone.[7,8] Physiologically, ECs regulate vascular tone through the

production and release of vasoactive molecules such as nitric oxide. Through these mechanisms, ECs signal the tunica media to implement vasomotor demands. In addition, they can indirectly regulate circulation through basal or inducible permeability. Basal permeability can be accomplished through differences in junctional properties dictated by the microenvironment and cell-cell signaling. In arteries, for instance, hemodynamic shear stress has been shown to induce continuous intercellular Notch signaling, which, in addition to suppressing proliferation, promotes maintenance of adherens junctions.[9,10] With activation by agonists, such as reactive oxygen species and cytokines like tumor necrosis factor-α (TNFα) generated during an inflammatory response, endothelial cells upregulate the production of chemokines and adhesion molecules for leukocyte extravasation leading to junctional weakening and increased permeability.[11] This weakening of the endothelial barrier is another major driver of vascular disorders.[12]

Endothelial activation can also occur in response to tissue oxygen demands and metabolic output leading to endothelial remodeling for angiogenesis - the formation of new capillaries from pre-existing vessels. This process is important in adults for maintaining tissue homeostasis for wound or ischemic injury repair and is notoriously exploited in the context of cancer.[5,13] For example, solid tumors proliferate rapidly, creating local hypoxia and tissue damage.[90] This leads to the upregulation of factors responsible for driving angiogenesis. Mitogens, chiefly vascular endothelial growth factor (VEGF), are secreted from the hypoxic stroma and, in a dose-dependent manner, initiate complex pathways responsible for transitioning mitotically quiescent ECs from established vessels to an actively proliferative phenotype for vascular expansion.[14] Paramount in both physiological and pathological angiogenesis, vessel growth and regeneration in the endothelium requires collective cell behavior to maintain coordinated sprouting and contiguous luminal integrity; otherwise outgrowth and stability will be compromised, leading to vessel regression.[5]

1.2 Intercellular Notch signaling and angiogenesis.

The Notch signaling pathway plays an essential role in cell fate determination, angiogenesis, and vascular stability. Initial signaling occurs when one of four transmembrane receptors (Notch1-4) binds with one of five transmembrane ligands (Delta-like1,3,4; Jagged1,2) presented on adjacent cells. Thus, canonical Notch signal transduction is dependent on cell-cell contact. Upon binding its ligand on signal sending cell 'A,' the tension established allows two sequential proteolytic cleavage events of the Notch receptor in signal receiving cell 'B', releasing the Notch intracellular domain (NICD) (Figure 1.2). The NICD is then free to translocate to the nucleus and trigger the formation of an activation complex for the transcription of Notch target genes in cell 'B.' This spatial restriction of gene activation allows distinct programing in neighboring cells of an otherwise homogenous population.

Modulation of specific Notch receptor and ligand combinations can also lead to unique signaling consequences. Notch1 and Notch4 are the predominant Notch receptors expressed by vascular endothelium. Active Notch signaling is critical for establishing and maintaining arterial specification and homeostasis.[15-17] Notch1 is the most prevalent receptor found in human aortic endothelial cells (HAECs) and, as mentioned previously, promotes endothelial quiescence through cell cycle arrest.[18-20] Critical to its function in spatial restriction, Notch activation represses expression of Delta ligands in the signal receiving EC, potentiating a unidirectional relationship between signal sending and receiving cells through lateral inhibition based on relative ligand abundance.[21,22] This feature creates the opportunity for imparting directionality based on crosstalk with other signaling pathways that can regulate either receptor or ligand expression. Notably, VEGF activation raises endothelial Delta-like 4 (DLL4) levels and utilizes Notch asymmetric signaling to create a boundary between sprouting ligand-expressing cells (tip cells) and neighboring receptor-activated cells (stalk cells).[23-27] Tip and stalk specification, however, are transient and alternate depending on cumulative signaling thresholds.[27,28] Notch activation has been shown to also conversely increase Jagged1 (Jag1) expression.[91] However, despite

conserved transcriptional machinery, Notch1:Jag1 interactions support different signaling potential based on ligand binding preferences and through antagonizing endothelial Notch1:Dll4 interactions.[29-32] Jagged1 expression instead appears important for mural cell recruitment and vascular stabilization.[33] Genetic or pharmacological inactivation of Notch signaling during angiogenesis, through deletion of *Notch1* or *Dll4*, results in an overwhelming number of tip cells.[23-25,34,35] These excesses halt angiogenesis as tip cells alone are unable to form trunks for vascular elongation, resulting in an underdeveloped vascular system. Hence, the balance between VEGF and Notch signaling are indispensable for directing angiogenesis and the morphogenesis of a functional vascular tree.

Heterotypic cell interactions during vascular morphogenesis also utilize Notch signaling. Jagged1 (JAG1) is expressed by ECs, pericytes, and smooth muscle cells,[12] and is critical in orchestrating endothelial controlled recruitment of mural cells (pericytes and smooth muscle cells) and promoting the formation of arteries.[33,36] Jag1 is also essential in specifying smooth muscle cells and preventing them from adopting a default chondrocyte fate and Jag1 is critical for maintaining this fate in adults.[37-40] In the immature vascular plexus, tip cells are largely devoid of Jag1 expression presumably due to the selective pressures of VEGF activation, though the exact molecular mechanisms behind this process are unknown.[41]

1.3 Mitogenic posttranscriptional regulation through Zinc-finger protein 36.

Cells are endowed with multiple intrinsic mechanisms that regulate levels and compartmentalization of protein expression. One such process involves post-transcriptional regulation through RNA binding proteins (RBPs).[42,43] Despite a large diversity in RBPs, most contain common RNA-binding modules, including the RNA recognition motif, heterogeneous nuclear RNP K-homology domain, and zinc fingers (ZFs) among others, that recognize limited and often short motifs within messenger RNAs (mRNAs).[44] The organization and/or repetition of these individually weak modules creates tailorable and collectively stronger RNA binding

interfaces that, in cooperation with other molecular domains and linkers, define the specificity and diverse functionality of RBPs.[45] Moreover, this modular architecture allows additional means of regulating RBP, and subsequent mRNA fate, based on topology and respective protein interactome. Therefore, though all mRNA is eventually degraded, the rate of turnover can vary greatly depending on RBP responsiveness to intracellular and extracellular stimuli (i.e. post translation modifications). Concurrently, many early response genes, low or absent in quiescent cells and induced rapidly by a variety of stimuli, have mRNA motifs that predispose them for rapid decay. Adenylate-uridylate (AU)-rich elements (AREs) within the 3' untranslated regions (3'UTR) are commonly associated with these short-lived transcripts.[46] Through *in silico* analysis, functional 3'UTR-AREs were identified in approximately 8% of the total human transcriptome.[47] This analysis revealed previously identified cytokines and oncogenes only represented 10% of identified ARE-mRNA, suggesting a larger role for this regulatory element besides inflammation and tumor suppression. In summation, synergy between ARE-mRNA and ARE-RBPs (AUBPs) acts as an important general mechanism for transcriptional regulation downstream cellular activation.

A group of AUBPs frequently linked to promoting mRNA decay downstream extracellular stimuli belong to a small family of uncommon CCCH type, tandem zinc finger proteins. The founding member of this family was first cloned from fibroblast mRNA elevated transiently in response to tumor promoter 12-O-tetradecanoylphorbol-13-acetate (TPA).[48] Coined TPA-induced-sequence 11 (TIS11), this protein was additionally confirmed sensitive to insulin and serum in other cell types.[48-51] TIS11 also known as tristetraprolin (TTP), Nup475, G0S24, and by its gene name Zinc finger protein 36 homolog (ZFP36), is a promiscuous ARE-mRNA binding protein.[52] Henceforth in this dissertation, this protein will be referred to as ZFP36. Three additional mammalian paralogs were later identified ZFP36L1 (also known as TIS11b, cMG1, Berg36, BRF-1, and ERF-1), ZFP36L2 (also known as TIS11d, BRF-2, and ERF-2), and ZFP36L3, though the fourth member appears exclusively expressed in mouse placenta and not in human tissues.[53,54]

Once bound to ARE-mRNA, subsequent interactions with additional *trans*-acting machinery to promote mRNA deadenylation, the first step in all major modes of mammalian mRNA decay.[55-57] ZFP36's affinity to general ARE motifs has also been linked to autoregulatory mechanisms as it has been shown in some instances to interact with 3'UTR-AREs of its mRNA.[58-60] Human ZFP36 family members have >70% amino acid homolog between zinc finger domains, lending to the prediction for functional redundancy in mRNA targets.[61-62] However, this potential overlap and autoregulation is often mitigated depending on tissue distribution, sub-cellular localization, extracellular cues, and general expression of each member.[63-66] These differences in function are further confirmed in studies with knock-out (KO) mice. ZFP36 KO mice develop severe inflammatory syndrome primarily as a consequence of unchecked TNFα (ARE-mRNA target of ZFP36 in macrophages).[52] Whereas ZFP36L1 and ZFP36L2 KO both induce lethality from vascular abnormalities and deficiency in definitive hematopoiesis, respectively.[67-70] These strong developmental defects are in part due to Notch dysregulation as both ZFP36L1 and ZFP36L2 show dose dependent suppression of VEGF-A and Notch1 mRNA, both of which contain canonical 3'UTR-ARE motifs.[67,71-73] Many of these early studies utilize luciferase-based assays that overexpress ZFP36 family members and luciferase-based constructs to observe changes in signal intensities. These overexpression models, however, do not necessarily recapitulate endogenous interactions. For instance, overexpression of ZFP36 in the absence of stress has been observed to promote stress granule accumulation, causing non-specific ZFP36 mediated mRNA instability.[74] Consequently, sequence information alone is not sufficient to reliably predict AUBP binding; competing RBPs and spatiotemporal expressions vary depending on cellular environment. Additionally, despite their high specificity for AREs, the ZFP36 family members have been shown to regulate mRNA through non-ARE sequences or indirectly through networking with other RBPs.[74-78] Furthermore, a significant proportion of human genes (~25%) differ in ARE patterning compared to mouse and rat orthologs.[79] To combat these confounding issues, many researchers have turned to recently developed techniques that utilize *in vivo* UV-crosslinking. By

irradiating cells through UV-light exposure, irreversible covalent bonds are formed between proteins and RNA in their immediate vicinity.[80] Subsequent isolation and immunoprecipitation (together CLIP) combined with high-throughput sequencing can then be utilized to validate transcriptome-wide protein-RNA interactions with nucleotide resolution.[81,82] While published CLIP datasets for ZFP36 and ZFP36L1 exist, most were conducted in mouse immune cells (B cells, T cells, and macrophages) and biased toward founding member ZFP36. Comparing these with a single human ZFP36-CLIP dataset performed in human embryonic kidney cells (HEKs) there are several inconsistencies in identified targets.[83] Ergo, the contributions of ZFP36 family members in endothelial specific activation responses requires further validation.

Similar to many of its ARE-mRNA targets, ZFP36 family member expression levels are usually low or undetectable in most cell types under quiescent conditions, but robust induction can occur in response to stimuli.[64,84-88] Of note, previous experiments from our laboratory on EC regeneration revealed robust expression of ZFP36 in the proliferative zone of injured arteries.[13,89] These initial findings prompted our interest on the potential physiological function of ZFP36 in the vasculature and its role at critical times when VEGF is highly expressed during angiogenesis.

1.4 FIGURES

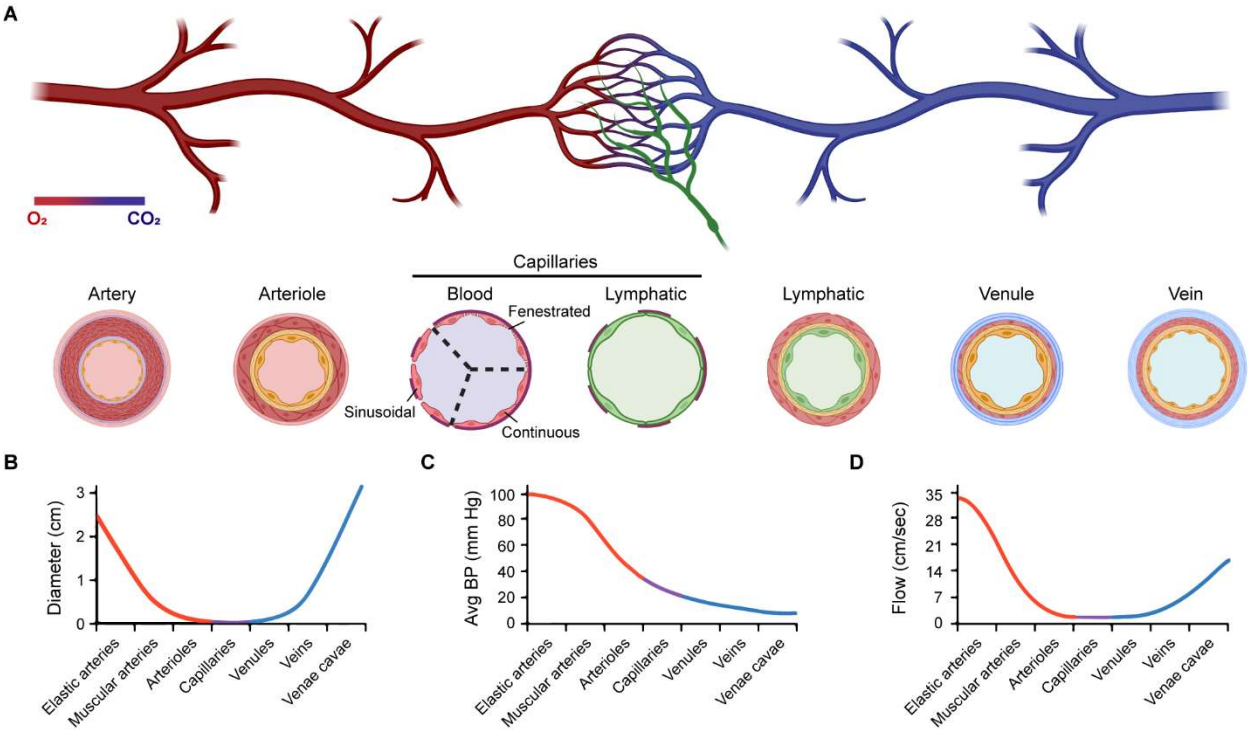

Figure 1.1 – Endothelial vessel diversity.

(A) General overview of systemic blood and lymphatic vessels and heterogeneity in endothelial microenvironment. Created with BioRender.com **(B-D)** Healthy adult human differences in **(B)** vessel diameter, **(C)** average blood pressure (Avg BP), and **(D)** blood flow velocity across various vascular beds.[4] Adapted from “Systemic Blood Vessels”, by BioRender.com (2023). Retrieved from https://app.biorender.com/biorender-templates.

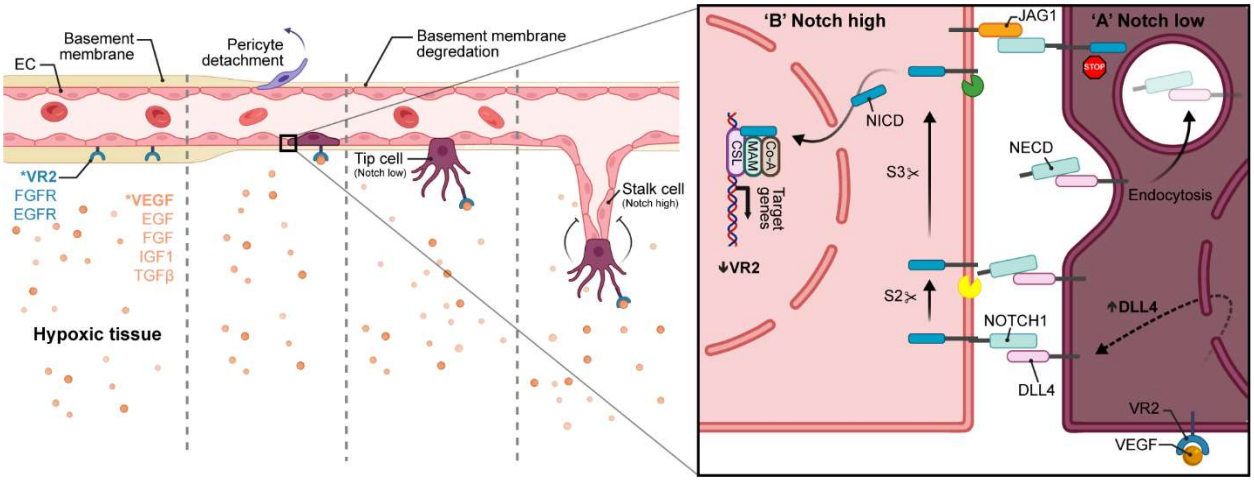

Figure 1.2 – Angiogenesis regulation through Notch signaling.

Schematic of the basic steps of sprouting angiogenesis. Parenchymal cells respond to hypoxic environment by secreting proangiogenic molecules (listed in orange). Key growth factor vascular endothelial growth factor (VEGF) binds to VEGF-A receptor 2 (VR2) on endothelial cells and triggers activation. These activated endothelial cells and other activate mural cells secrete factors that degrade vascular basement membrane and cause pericyte detachment, liberating activated endothelial cells which become invasive and protrude filopodia. Specification of tip and stalk cells is a dynamic process that culminates based on relative Notch1:DLL4 signaling, where comparatively 'Notch low' cells maintain lead position. This spouting process continues until nutrient and oxygen supply needs of newly vascularized tissue are met, silencing secretion of proangiogenic factors and reinforcing endothelial quiescence and vessel maturation. Adapted from "Tumor Vascularization" and "Notch Signaling Pathway", by BioRender.com (2023). Retrieved from https://app.biorender.com/biorender-templates.

1.5 REFERENCES

1. Félétou, M. (2011). The Endothelium: Part 1: Multiple Functions of the Endothelial Cells—Focus on Endothelium-Derived Vasoactive Mediators. Morgan & Claypool Life Sciences.

2. Aird, W.C. (2007). Phenotypic heterogeneity of the endothelium: I. Structure, function, and mechanisms. Circ. Res. 100, 158–173. 10.1161/01.RES.0000255691.76142.4a.

3. Deng, D.X.-F., Tsalenko, A., Vailaya, A., Ben-Dor, A., Kundu, R., Estay, I., Tabibiazar, R., Kincaid, R., Yakhini, Z., Bruhn, L., et al. (2006). Differences in vascular bed disease susceptibility reflect differences in gene expression response to atherogenic stimuli. Circ. Res. 98, 200–208. 10.1161/01.RES.0000200738.50997.f2.

4. Gopalan, C. (2022). Biology of Cardiovascular and Metabolic Disease. S.L.: Elsevier Academic Press.

5. Carmeliet, P. (2003). Angiogenesis in health and disease. Nat. Med. 9, 653–660. 10.1038/nm0603-653.

6. Heart Disease and Stroke Statistics - 2023 Update - Professional Heart Daily | American Heart Association https://professional.heart.org/en/science-news/heart-disease-and-stroke-statistics-2023-update.

7. Sun, H.-J., Wu, Z.-Y., Nie, X.-W., and Bian, J.-S. (2019). Role of endothelial dysfunction in cardiovascular diseases: the link between inflammation and hydrogen sulfide. Front. Pharmacol. 10, 1568. 10.3389/fphar.2019.01568.

8. Lerman, A., and Burnett, J.C. (1992). Intact and altered endothelium in regulation of vasomotion. Circulation 86, III12-19.

9. Polacheck, W.J., Kutys, M.L., Yang, J., Eyckmans, J., Wu, Y., Vasavada, H., Hirschi, K.K., and Chen, C.S. (2017). A non-canonical Notch complex regulates adherens junctions and vascular barrier function. Nature 552, 258–262. 10.1038/nature24998.

10. Mack, J.J., Mosqueiro, T.S., Archer, B.J., Jones, W.M., Sunshine, H., Faas, G.C., Briot, A., Aragón, R.L., Su, T., Romay, M.C., et al. (2017). NOTCH1 is a mechanosensor in adult arteries. Nat. Commun. 8, 1620. 10.1038/s41467-017-01741-8.

11. Lum, H., and Roebuck, K.A. (2001). Oxidant stress and endothelial cell dysfunction. Am J Physiol, Cell Physiol 280, C719-41. 10.1152/ajpcell.2001.280.4.C719.

12. Yuan, S.Y., and Rigor, R.R. (2010). Regulation of endothelial barrier function (Morgan & Claypool Life Sciences).

13. McDonald, A.I., Shirali, A.S., Aragón, R., Ma, F., Hernandez, G., Vaughn, D.A., Mack, J.J., Lim, T.Y., Sunshine, H., Zhao, P., et al. (2018). Endothelial Regeneration of Large Vessels Is a Biphasic Process Driven by Local Cells with Distinct Proliferative Capacities. Cell Stem Cell 23, 210-225.e6. 10.1016/j.stem.2018.07.011.

14. Senger, D.R., Galli, S.J., Dvorak, A.M., Perruzzi, C.A., Harvey, V.S., and Dvorak, H.F. (1983). Tumor cells secrete a vascular permeability factor that promotes accumulation of ascites fluid. Science 219, 983–985. 10.1126/science.6823562.

15. Villa, N., Walker, L., Lindsell, C.E., Gasson, J., Iruela-Arispe, M.L., and Weinmaster, G. (2001). Vascular expression of Notch pathway receptors and ligands is restricted to arterial vessels. Mech. Dev. 108, 161–164. 10.1016/S0925-4773(01)00469-5.

16. Lawson, N.D., Scheer, N., Pham, V.N., Kim, C.H., Chitnis, A.B., Campos-Ortega, J.A., and Weinstein, B.M. (2001). Notch signaling is required for arterial-venous differentiation during embryonic vascular development. Development 128, 3675–3683. 10.1242/dev.128.19.3675.

17. Quillien, A., Moore, J.C., Shin, M., Siekmann, A.F., Smith, T., Pan, L., Moens, C.B., Parsons, M.J., and Lawson, N.D. (2014). Distinct Notch signaling outputs pattern the developing arterial system. Development 141, 1544–1552. 10.1242/dev.099986.

18. Liu, Z.-J., Shirakawa, T., Li, Y., Soma, A., Oka, M., Dotto, G.P., Fairman, R.M., Velazquez, O.C., and Herlyn, M. (2003). Regulation of Notch1 and Dll4 by vascular endothelial growth factor in arterial endothelial cells: implications for modulating arteriogenesis and angiogenesis. Mol. Cell. Biol. 23, 14–25. 10.1128/MCB.23.1.14-25.2003.

19. Fang, J.S., Coon, B.G., Gillis, N., Chen, Z., Qiu, J., Chittenden, T.W., Burt, J.M., Schwartz, M.A., and Hirschi, K.K. (2017). Shear-induced Notch-Cx37-p27 axis arrests endothelial cell cycle to enable arterial specification. Nat. Commun. 8, 2149. 10.1038/s41467-017-01742-7.

20. Noseda, M., Chang, L., McLean, G., Grim, J.E., Clurman, B.E., Smith, L.L., and Karsan, A. (2004). Notch activation induces endothelial cell cycle arrest and participates in contact inhibition: role of p21Cip1 repression. Mol. Cell. Biol. 24, 8813–8822. 10.1128/MCB.24.20.8813-8822.2004.

21. Sjöqvist, M., and Andersson, E.R. (2019). Do as I say, Not(ch) as I do: Lateral control of cell fate. Dev. Biol. 447, 58–70. 10.1016/j.ydbio.2017.09.032.

22. Sprinzak, D., Lakhanpal, A., Lebon, L., Santat, L.A., Fontes, M.E., Anderson, G.A., Garcia-Ojalvo, J., and Elowitz, M.B. (2010). Cis-interactions between Notch and Delta generate mutually exclusive signalling states. Nature 465, 86–90. 10.1038/nature08959.

23. Lobov, I.B., Renard, R.A., Papadopoulos, N., Gale, N.W., Thurston, G., Yancopoulos, G.D., and Wiegand, S.J. (2007). Delta-like ligand 4 (Dll4) is induced by VEGF as a negative regulator of angiogenic sprouting. Proc Natl Acad Sci USA 104, 3219–3224. 10.1073/pnas.0611206104.

24. Leslie, J.D., Ariza-McNaughton, L., Bermange, A.L., McAdow, R., Johnson, S.L., and Lewis, J. (2007). Endothelial signalling by the Notch ligand Delta-like 4 restricts angiogenesis. Development 134, 839–844. 10.1242/dev.003244.

25. Hellström, M., Phng, L.-K., Hofmann, J.J., Wallgard, E., Coultas, L., Lindblom, P., Alva, J., Nilsson, A.-K., Karlsson, L., Gaiano, N., et al. (2007). Dll4 signalling through Notch1 regulates formation of tip cells during angiogenesis. Nature 445, 776–780. 10.1038/nature05571.

26. Siekmann, A.F., and Lawson, N.D. (2007). Notch signalling limits angiogenic cell behaviour in developing zebrafish arteries. Nature 445, 781–784. 10.1038/nature05577.

27. Jakobsson, L., Franco, C.A., Bentley, K., Collins, R.T., Ponsioen, B., Aspalter, I.M., Rosewell, I., Busse, M., Thurston, G., Medvinsky, A., et al. (2010). Endothelial cells dynamically compete for the tip cell position during angiogenic sprouting. Nat. Cell Biol. 12, 943–953. 10.1038/ncb2103.

28. Moya, I.M., Umans, L., Maas, E., Pereira, P.N.G., Beets, K., Francis, A., Sents, W., Robertson, E.J., Mummery, C.L., Huylebroeck, D., et al. (2012). Stalk cell phenotype depends on integration of Notch and Smad1/5 signaling cascades. Dev. Cell 22, 501–514. 10.1016/j.devcel.2012.01.007.

29. Sprinzak, D., and Blacklow, S.C. (2021). Biophysics of notch signaling. Annu. Rev. Biophys. 50, 157–189. 10.1146/annurev-biophys-101920-082204.

30. Nakano, Y., Nakao, S., Sueoka, M., Kasahara, D., Tanno, Y., Sumiyoshi, H., Itoh, T., Miyajima, A., Hozumi, K., and Inagaki, Y. (2022). Two distinct Notch signals, Delta-like 4/Notch1 and Jagged-1/Notch2, antagonistically regulate chemical hepatocarcinogenesis in mice. Commun. Biol. 5, 85. 10.1038/s42003-022-03013-8.

31. Benedito, R., Roca, C., Sörensen, I., Adams, S., Gossler, A., Fruttiger, M., and Adams, R.H. (2009). The notch ligands Dll4 and Jagged1 have opposing effects on angiogenesis. Cell 137, 1124–1135. 10.1016/j.cell.2009.03.025.

32. Antfolk, D., Sjöqvist, M., Cheng, F., Isoniemi, K., Duran, C.L., Rivero-Muller, A., Antila, C., Niemi, R., Landor, S., Bouten, C.V.C., et al. (2017). Selective regulation of Notch ligands during angiogenesis is mediated by vimentin. Proc Natl Acad Sci USA 114, E4574–E4581. 10.1073/pnas.1703057114.

33. Pedrosa, A.-R., Trindade, A., Fernandes, A.-C., Carvalho, C., Gigante, J., Tavares, A.T., Diéguez-Hurtado, R., Yagita, H., Adams, R.H., and Duarte, A. (2015). Endothelial Jagged1 antagonizes Dll4 regulation of endothelial branching and promotes vascular maturation downstream of Dll4/Notch1. Arterioscler. Thromb. Vasc. Biol. 35, 1134–1146. 10.1161/ATVBAHA.114.304741.

34. Suchting, S., Freitas, C., le Noble, F., Benedito, R., Bréant, C., Duarte, A., and Eichmann, A. (2007). The Notch ligand Delta-like 4 negatively regulates endothelial tip cell formation and vessel branching. Proc Natl Acad Sci USA 104, 3225–3230. 10.1073/pnas.0611177104.

35. Noguera-Troise, I., Daly, C., Papadopoulos, N.J., Coetzee, S., Boland, P., Gale, N.W., Lin, H.C., Yancopoulos, G.D., and Thurston, G. (2006). Blockade of Dll4 inhibits tumour growth by promoting non-productive angiogenesis. Nature 444, 1032–1037. 10.1038/nature05355.

36. High, F.A., Lu, M.M., Pear, W.S., Loomes, K.M., Kaestner, K.H., and Epstein, J.A. (2008). Endothelial expression of the Notch ligand Jagged1 is required for vascular smooth muscle development. Proc Natl Acad Sci USA 105, 1955–1959. 10.1073/pnas.0709663105.

37. Liu, H., Kennard, S., and Lilly, B. (2009). NOTCH3 expression is induced in mural cells through an autoregulatory loop that requires endothelial-expressed JAGGED1. Circ. Res. 104, 466–475. 10.1161/CIRCRESAHA.108.184846.

38. Lindsell, C.E., Shawber, C.J., Boulter, J., and Weinmaster, G. (1995). Jagged: a mammalian ligand that activates Notch1. Cell 80, 909–917. 10.1016/0092-8674(95)90294-5.

39. Briot, A., Jaroszewicz, A., Warren, C.M., Lu, J., Touma, M., Rudat, C., Hofmann, J.J., Airik, R., Weinmaster, G., Lyons, K., et al. (2014). Repression of Sox9 by Jag1 is continuously required to suppress the default chondrogenic fate of vascular smooth muscle cells. Dev. Cell 31, 707–721. 10.1016/j.devcel.2014.11.023.

40. Breikaa, R.M., Denman, K., Ueyama, Y., McCallinhart, P.E., Khan, A.Q., Agarwal, G., Trask, A.J., Garg, V., and Lilly, B. (2022). Loss of Jagged1 in mature endothelial cells causes vascular dysfunction with alterations in smooth muscle phenotypes. Vascul. Pharmacol. 145, 107087. 10.1016/j.vph.2022.107087.

41. Hofmann, J.J., and Luisa Iruela-Arispe, M. (2007). Notch expression patterns in the retina: An eye on receptor-ligand distribution during angiogenesis. Gene Expr. Patterns 7, 461–470. 10.1016/j.modgep.2006.11.002.

42. Garneau, N.L., Wilusz, J., and Wilusz, C.J. (2007). The highways and byways of mRNA decay. Nat. Rev. Mol. Cell Biol. 8, 113–126. 10.1038/nrm2104.

43. Garneau, N.L., Wilusz, J., and Wilusz, C.J. (2007). The highways and byways of mRNA decay. Nat. Rev. Mol. Cell Biol. 8, 113–126. 10.1038/nrm2104.

44. Burd, C. G., & Dreyfuss, G. (1994). Conserved Structures and Diversity of Functions of RNA-Binding Proteins. Science, 265(5172), 615–621. 10.1126/science.8036511

45. Lunde, B.M., Moore, C., and Varani, G. (2007). RNA-binding proteins: modular design for efficient function. Nat. Rev. Mol. Cell Biol. 8, 479–490. 10.1038/nrm2178.

46. Barreau, C., Paillard, L., and Osborne, H.B. (2005). AU-rich elements and associated factors: are there unifying principles? Nucleic Acids Res. 33, 7138–7150. 10.1093/nar/gki1012.

47. Bakheet, T., Frevel, M., Williams, B.R., Greer, W., and Khabar, K.S. (2001). ARED: human AU-rich element-containing mRNA database reveals an unexpectedly diverse functional repertoire of encoded proteins. Nucleic Acids Res. 29, 246–254. 10.1093/nar/29.1.246.

48. Lim, R.W., Varnum, B.C., and Herschman, H.R. (1987). Cloning of tetradecanoyl phorbol ester-induced “primary response” sequences and their expression in density-arrested Swiss 3T3 cells and a TPA non-proliferative variant. Oncogene 1, 263–270.

49. DuBois, R.N., McLane, M.W., Ryder, K., Lau, L.F., and Nathans, D. (1990). A growth factor-inducible nuclear protein with a novel cysteine/histidine repetitive sequence. J. Biol. Chem. 265, 19185–19191. 10.1016/S0021-9258(17)30642-7.

50. Lai, W.S., Stumpo, D.J., and Blackshear, P.J. (1990). Rapid insulin-stimulated accumulation of an mRNA encoding a proline-rich protein. J. Biol. Chem. 265, 16556–16563. 10.1016/S0021-9258(17)46259-4.

51. Ma, Q., and Herschman, H.R. (1991). A corrected sequence for the predicted protein from the mitogen-inducible TIS11 primary response gene. Oncogene 6, 1277–1278.

52. Taylor, G.A., Carballo, E., Lee, D.M., Lai, W.S., Thompson, M.J., Patel, D.D., Schenkman, D.I., Gilkeson, G.S., Broxmeyer, H.E., Haynes, B.F., et al. (1996). A Pathogenetic Role for TNFα in the Syndrome of Cachexia, Arthritis, and Autoimmunity Resulting from Tristetraprolin (TTP) Deficiency. Immunity 4, 445–454. 10.1016/S1074-7613(00)80411-2.

53. Brooks, S.A., and Blackshear, P.J. (2013). Tristetraprolin (TTP): interactions with mRNA and proteins, and current thoughts on mechanisms of action. Biochim. Biophys. Acta 1829, 666–679. 10.1016/j.bbagrm.2013.02.003.

54. Blackshear, P.J., Phillips, R.S., Ghosh, S., Ramos, S.B.V., Richfield, E.K., and Lai, W.S. (2005). Zfp36l3, a rodent X chromosome gene encoding a placenta-specific member of the Tristetraprolin family of CCCH tandem zinc finger proteins. Biol. Reprod. 73, 297–307. 10.1095/biolreprod.105.040527.

55. Lykke-Andersen, J., and Wagner, E. (2005). Recruitment and activation of mRNA decay enzymes by two ARE-mediated decay activation domains in the proteins TTP and BRF-1. Genes Dev. 19, 351–361. 10.1101/gad.1282305.

56. Fabian, M.R., Frank, F., Rouya, C., Siddiqui, N., Lai, W.S., Karetnikov, A., Blackshear, P.J., Nagar, B., and Sonenberg, N. (2013). Structural basis for the recruitment of the human CCR4-NOT deadenylase complex by tristetraprolin. Nat. Struct. Mol. Biol. 20, 735–739. 10.1038/nsmb.2572.

57. Chen, C.-Y.A., and Shyu, A.-B. (2011). Mechanisms of deadenylation-dependent decay. Wiley Interdiscip. Rev. RNA 2, 167–183. 10.1002/wrna.40.

58. Brooks, S.A., Connolly, J.E., and Rigby, W.F.C. (2004). The role of mRNA turnover in the regulation of tristetraprolin expression: evidence for an extracellular signal-regulated kinase-specific, AU-rich element-dependent, autoregulatory pathway. J. Immunol. 172, 7263–7271. 10.4049/jimmunol.172.12.7263.

59. Tang, T., Scambler, T.E., Smallie, T., Cunliffe, H.E., Ross, E.A., Rosner, D.R., O'Neil, J.D., and Clark, A.R. (2017). Macrophage responses to lipopolysaccharide are modulated by a feedback loop involving prostaglandin E2, dual specificity phosphatase 1 and tristetraprolin. Sci. Rep. 7, 4350. 10.1038/s41598-017-04100-1.

60. Tchen, C.R., Brook, M., Saklatvala, J., and Clark, A.R. (2004). The stability of tristetraprolin mRNA is regulated by mitogen-activated protein kinase p38 and by tristetraprolin itself. J. Biol. Chem. 279, 32393–32400. 10.1074/jbc.M402059200.

61. Varnum, B.C., Ma, Q.F., Chi, T.H., Fletcher, B., and Herschman, H.R. (1991). The TIS11 primary response gene is a member of a gene family that encodes proteins with a highly conserved sequence containing an unusual Cys-His repeat. Mol. Cell. Biol. 11, 1754–1758.

62. Deveau, L.M., and Massi, F. (2016). Three Residues Make an Evolutionary Switch for Folding and RNA-Destabilizing Activity in the TTP Family of Proteins. ACS Chem. Biol. 11, 435–443. 10.1021/acschembio.5b00639.

63. Clement, S.L., Scheckel, C., Stoecklin, G., and Lykke-Andersen, J. (2011). Phosphorylation of tristetraprolin by MK2 impairs AU-rich element mRNA decay by preventing deadenylase recruitment. Mol. Cell. Biol. 31, 256–266. 10.1128/MCB.00717-10.

64. Sanduja, S., Blanco, F.F., and Dixon, D.A. (2011). The roles of TTP and BRF proteins in regulated mRNA decay. Wiley Interdiscip. Rev. RNA 2, 42–57. 10.1002/wrna.28.

65. Prenzler, F., Fragasso, A., Schmitt, A., and Munz, B. (2016). Functional analysis of ZFP36 proteins in keratinocytes. Eur. J. Cell Biol. 95, 277–284. 10.1016/j.ejcb.2016.04.007.

66. Carrick, D.M., and Blackshear, P.J. (2007). Comparative expression of tristetraprolin (TTP) family member transcripts in normal human tissues and cancer cell lines. Arch. Biochem. Biophys. 462, 278–285. 10.1016/j.abb.2007.04.011.

67. Bell, S.E., Sanchez, M.J., Spasic-Boskovic, O., Santalucia, T., Gambardella, L., Burton, G.J., Murphy, J.J., Norton, J.D., Clark, A.R., and Turner, M. (2006). The RNA binding protein Zfp36l1 is required for normal vascularisation and post-transcriptionally regulates VEGF expression. Dev. Dyn. 235, 3144–3155. 10.1002/dvdy.20949.

68. Stumpo, D.J., Byrd, N.A., Phillips, R.S., Ghosh, S., Maronpot, R.R., Castranio, T., Meyers, E.N., Mishina, Y., and Blackshear, P.J. (2004). Chorioallantoic fusion defects and embryonic lethality resulting from disruption of Zfp36L1, a gene encoding a CCCH tandem zinc finger protein of the Tristetraprolin family. Mol. Cell. Biol. 24, 6445–6455. 10.1128/MCB.24.14.6445-6455.2004.

69. Ramos, S.B.V., Stumpo, D.J., Kennington, E.A., Phillips, R.S., Bock, C.B., Ribeiro-Neto, F., and Blackshear, P.J. (2004). The CCCH tandem zinc-finger protein Zfp36l2 is crucial for female fertility and early embryonic development. Development 131, 4883–4893. 10.1242/dev.01336.

70. Stumpo, D.J., Broxmeyer, H.E., Ward, T., Cooper, S., Hangoc, G., Chung, Y.J., Shelley, W.C., Richfield, E.K., Ray, M.K., Yoder, M.C., et al. (2009). Targeted disruption of Zfp36l2, encoding a CCCH tandem zinc finger RNA-binding protein, results in defective hematopoiesis. Blood 114, 2401–2410. 10.1182/blood-2009-04-214619.

71. Hu, Y.-X., Zhu, R.-F., Qin, Y.-W., Zhao, X.-X., and Jing, Q. (2020). Zfp36l1b protects angiogenesis through Notch1b/Dll4 and Vegfa regulation in zebrafish. Atherosclerosis 309, 56–64. 10.1016/j.atherosclerosis.2020.07.021.

72. Albano, F., Tucci, V., Blackshear, P.J., Reale, C., Roberto, L., Russo, F., Marotta, P., Porreca, I., Colella, M., Mallardo, M., et al. (2021). ZFP36L2 role in thyroid functionality. Int. J. Mol. Sci. 22. 10.3390/ijms22179379.

73. Hodson, D.J., Janas, M.L., Galloway, A., Bell, S.E., Andrews, S., Li, C.M., Pannell, R., Siebel, C.W., MacDonald, H.R., De Keersmaecker, K., et al. (2010). Deletion of the RNA-binding proteins ZFP36L1 and ZFP36L2 leads to perturbed thymic development and T lymphoblastic leukemia. Nat. Immunol. 11, 717–724. 10.1038/ni.1901.

74. Stoecklin, G., Tenenbaum, S.A., Mayo, T., Chittur, S.V., George, A.D., Baroni, T.E., Blackshear, P.J., and Anderson, P. (2008). Genome-wide analysis identifies interleukin-10 mRNA as target of tristetraprolin. J. Biol. Chem. 283, 11689–11699. 10.1074/jbc.M709657200.

75. Emmons, J., Townley-Tilson, W.H.D., Deleault, K.M., Skinner, S.J., Gross, R.H., Whitfield, M.L., and Brooks, S.A. (2008). Identification of TTP mRNA targets in human dendritic cells reveals TTP as a critical regulator of dendritic cell maturation. RNA 14, 888–902. 10.1261/rna.748408.

76. Linker, K., Pautz, A., Fechir, M., Hubrich, T., Greeve, J., and Kleinert, H. (2005). Involvement of KSRP in the post-transcriptional regulation of human iNOS expression-complex interplay of KSRP with TTP and HuR. Nucleic Acids Res. 33, 4813–4827. 10.1093/nar/gki797.

77. Fechir, M., Linker, K., Pautz, A., Hubrich, T., Förstermann, U., Rodriguez-Pascual, F., and Kleinert, H. (2005). Tristetraprolin regulates the expression of the human inducible nitric-oxide synthase gene. Mol. Pharmacol. 67, 2148–2161. 10.1124/mol.104.008763.

78. Kedar, V.P., Zucconi, B.E., Wilson, G.M., and Blackshear, P.J. (2012). Direct binding of specific AUF1 isoforms to tandem zinc finger domains of tristetraprolin (TTP) family proteins. J. Biol. Chem. 287, 5459–5471. 10.1074/jbc.M111.312652.

79. Halees, A.S., El-Badrawi, R., and Khabar, K.S.A. (2008). ARED Organism: expansion of ARED reveals AU-rich element cluster variations between human and mouse. Nucleic Acids Res. 36, D137-40. 10.1093/nar/gkm959.

80. Ule, J., Jensen, K.B., Ruggiu, M., Mele, A., Ule, A., and Darnell, R.B. (2003). CLIP identifies Nova-regulated RNA networks in the brain. Science 302, 1212–1215. 10.1126/science.1090095.

81. König, J., Zarnack, K., Luscombe, N.M., and Ule, J. (2012). Protein-RNA interactions: new genomic technologies and perspectives. Nat. Rev. Genet. 13, 77–83. 10.1038/nrg3141.

82. Hafner, M., Katsantoni, M., Köster, T., Marks, J., Mukherjee, J., Staiger, D., Ule, J., and Zavolan, M. (2021). CLIP and complementary methods. Nat. Rev. Methods Primers 1, 20. 10.1038/s43586-021-00018-1.

83. Li, J.-H., Liu, S., Zhou, H., Qu, L.-H., and Yang, J.-H. (2014). starBase v2.0: decoding miRNA-ceRNA, miRNA-ncRNA and protein-RNA interaction networks from large-scale CLIP-Seq data. Nucleic Acids Res. 42, D92-7. 10.1093/nar/gkt1248.

84. Newton, R., Shah, S., Altonsy, M.O., and Gerber, A.N. (2017). Glucocorticoid and cytokine crosstalk: Feedback, feedforward, and co-regulatory interactions determine repression or resistance. J. Biol. Chem. 292, 7163–7172. 10.1074/jbc.R117.777318.

85. Cicchetto, A.C., Jacobson, E.C., Sunshine, H., Wilde, B.R., Krall, A.S., Jarrett, K.E., Sedgeman, L., Turner, M., Plath, K., Iruela-Arispe, M.L., et al. (2023). ZFP36-mediated mRNA decay regulates metabolism. Cell Rep. 42, 112411. 10.1016/j.celrep.2023.112411.

86. Brook, M., Tchen, C.R., Santalucia, T., McIlrath, J., Arthur, J.S.C., Saklatvala, J., and Clark, A.R. (2006). Posttranslational regulation of tristetraprolin subcellular localization and protein stability by p38 mitogen-activated protein kinase and extracellular signal-regulated kinase pathways. Mol. Cell. Biol. 26, 2408–2418. 10.1128/MCB.26.6.2408-2418.2006.

87. Amit, I., Citri, A., Shay, T., Lu, Y., Katz, M., Zhang, F., Tarcic, G., Siwak, D., Lahad, J., Jacob-Hirsch, J., et al. (2007). A module of negative feedback regulators defines growth factor signaling. Nat. Genet. 39, 503–512. 10.1038/ng1987.

88. Marderosian, M., Sharma, A., Funk, A.P., Vartanian, R., Masri, J., Jo, O.D., and Gera, J.F. (2006). Tristetraprolin regulates Cyclin D1 and c-Myc mRNA stability in response to rapamycin in an Akt-dependent manner via p38 MAPK signaling. Oncogene 25, 6277–6290. 10.1038/sj.onc.1209645.

89. Shirali, A.S., Romay, M.C., McDonald, A.I., Su, T., Steel, M.E., and Iruela-Arispe, M.L. (2018). A multi-step transcriptional cascade underlies vascular regeneration *in vivo*. Sci. Rep. 8, 5430. 10.1038/s41598-018-23653-3.

90. Chung, A.S., Lee, J., and Ferrara, N. (2010). Targeting the tumour vasculature: insights from physiological angiogenesis. Nat. Rev. Cancer 10, 505–514. 10.1038/nrc2868.

91. Manderfield, L.J., High, F.A., Engleka, K.A., Liu, F., Li, L., Rentschler, S., and Epstein, J.A. (2012). Notch activation of Jagged1 contributes to the assembly of the arterial wall. Circulation 125, 314–323. 10.1161/CIRCULATIONAHA.111.047159.

CHAPTER 2

2.1 – INTRODUCTION

This chapter presents *in vitro* findings from a manuscript currently in press (Sunshine et al., 2023 Cell Reports). The aim of the study is to examine the functional role for ZFP36 in endothelial biology. All experiments have therefore been completed and are awaiting final review. Previous experiments from our laboratory on EC regeneration revealed robust expression of ZFP36 in the proliferative zone of injured arteries.[1,2] These initial findings prompted interest on the potential physiological function of ZFP36 in the vasculature and its role at critical times when VEGF is highly expressed during angiogenesis. Included in this section is the first half of the manuscript that identifies specific finding *in vitro* of specific upregulation of ZFP36 in a VEGF dependent manner and specific regulation of Notch ligand Jagged1.

2.2 – RESULTS

2.2.1 - VEGF exposure upregulates the RNA-decay protein ZFP36.

Given the high induction of ZFP36 during regeneration of arteries[2] and in the context of its upregulation by multiple growth factors,[3] we asked whether ZFP36 could be induced by VEGF. Bulk RNA sequencing on HUVECs stimulated with VEGF for one hour revealed that ZFP36 was within the top 20 induced transcripts (Figures 2.1A, 2.1B). Time-course experiments confirmed the RNAseq findings at the protein level (Figure 2.1C) and further revealed that protein induction was short lived, peaking at 1 h and retaining high levels for an additional 1.5 hours. Importantly other members of the ZFP36 family, namely ZFP36L1 and ZFP36L2,[4] were also expressed by ECs but were not induced by VEGF (Figure 2.1C). The response to VEGF was transcriptional, as shown by a clear peak of ZFP36 mRNA at 30min that preceded protein induction (Figure 2.1D). Moreover, the transient nature of this induction and the presence of additional molecular weight forms recognized by the antibody implies additional post-transcriptional regulation and post-translational modifications, such as autoregulation of mRNA and/or control of protein stability

through phosphorylation.[5,6] The rapid VEGF sensitivity was reproduced in multiple HUVEC biological replicates and was noted to extend to human aortic and human dermal microvascular ECs (HAECs and HDMECs respectively) (Figure S2.1A-D). Interestingly, while ZFP36 induction patterns were similar across different vascular beds, relative levels of the ZFP36L1 and ZFP36L2 exhibited variability; both are highly expressed by HAECs, in contrast to higher levels of ZFP36L2 by HUVECs and ZFP36L1 by HDMECs. Induction of ZFP36 by VEGF was also confirmed by immunocytochemistry on endothelial monolayers, showing presence of ZFP36 both in nucleus and cytoplasm (Figure 2.1E, 2.1F). The dynamics of VEGF response and known function as an mRNA decay factor suggested a conserved role for ZFP36 in transient post-transcriptional regulation downstream VEGF signaling.

Next, to determine whether ZFP36 induction used canonical VEGF signaling, pretreatment with a selective small molecule VEGFR 2 (VR2) inhibitor (ZM323881)[7] was utilized to block receptor activation (Figure 2.1G, 2.1H). In the presence of VEGFR2 inhibition, ZFP36 induction was drastically reduced at both protein and transcript levels (Figure 2.1H, 2.1I). Interestingly, only a short pulse of VEGF (5min) was sufficient to trigger potent upregulation of ZFP36 by 1h (Figure 2.1J). Finally, we confirmed that VEGF-mediated induction of ZFP36 requires transcription by co-treatment with Actinomycin D (ActD) (Figure 2.1K). Together these results indicate a functional role for ZFP36 mediated mRNA-decay in ECs downstream VEGF signaling.

2.2.2 - ZFP36 binds to the 3'UTR of Jag1.

To investigate the potential function of ZFP36 in the endothelium using enhanced UV crosslinking and immunoprecipitation (eCLIP-seq) to unbiasedly identify putative ZFP36 target mRNAs at the transcriptome-wide level.[3] This approach preserves RNA-protein complexes by promoting covalent interactions, thus facilitating immunoprecipitation of ZFP36 and its associated transcripts. Subsequent sequencing of libraries generated from the pull-down templates allows for the identification of binding sites with high precision.[8] Recognizing the potential overlapping

role of ZFP36L1 and ZFP36L2 in transcript binding, libraries were generated using immortalized embryonic fibroblasts from mice with concurrent flox alleles in *Zfp36, Zfp36l1* and *Zfp36l2* loci (Figure 2.2A). RNA libraries were generated from serum stimulated parental or Cre-recombinase infected cells (Figure 2.2B). The approach was replicated twice with high reproducibility, successfully validating many of the previously identified targets.[3,9-11] Importantly, the archetypal feature as an RNA binding protein that preferentially targets AREs was fully reproduced, as indicated by a nearly log-fold enrichment of the UAUUUAUU motif relative to competing binding sites.[3] Amongst previously unreported ZFP36 targets with direct relation to endothelial biological context was Jagged1. Using Integrative Genomics Viewer software, we found that ZFP36 bound to the 3'UTR from wild-type cells but the peaks were completely absent from triple knock-out cells (TKO) in independent replicates (Figure 2.2C). The complete absence of peaks in the controls (TKO) further confirmed that the signal corresponded to ZFP36 binding to the *Jag1* 3'UTR, and not from off-target affinities of the ZFP36 antibody. Importantly, the major peak showed several ARE motifs in the 3'UTR of Jag1, consistent with its known affinity for this sequence, and indicative of robust binding in this region (Figure 2.2C, boxed sequence and asterisk; Figure S2.2A, full ms-JAG1 3'UTR sequence). The CLIP results were further confirmed using CLIP-qPCR and comparing with previously identified ZFP36-binding target *Ptgs2* (Figure S2.2B).

Based on sequence and AU-rich element (ARE) motif similarities between mouse and human Jag1, we suspected conserved ZFP36 *JAG1*-binding affinity across species and cell types (Figure S2.2C). To test the effect of ZFP36 on human endothelial cells, we generated CRISPR control and KO cells. Since levels of ZFP36 are difficult to detect without VEGF stimulation, cells were exposed to VEGF for 1h to verify that HUVEC knockout for *ZFP36 (ZFP36* KO) failed to be induced (Figure S2.3A). We also observed that the increased baseline levels of JAG1 in ZFP36 KO cells were stable even after 1h of VEGF exposure (Figure S2.3A, S2.3B). These increases at first glance did not appear to phenotypically change the cells, as ZFP36 KO did not significantly affect key behaviors of migration or proliferation and the cells appeared otherwise normal in

cultured monolayers (Figure S2.3C-F). Consistent with changes in protein abundance, we also found that *JAG1* transcripts were elevated by approximately 50% in the absence of *ZFP36* (Figure 2.2D). Increases in JAG1 in the absence of ZFP36 were further validated through immunocytochemistry (Figure 2.2E, 2.2F). The corresponding relationship between ZFP36 induction by VEGF and JAG1 levels was also tested through a time-course of VEGF stimulation in control and KO cells. Consistent with the notion that ZFP36 regulates JAG1 levels, endothelial cells exposed to VEGF, which upregulates ZFP36, showed a sustained reduction in JAG1 protein (1-6h). However, the same was not observed in endothelial cells where ZFP36 was inactivated (Figure 2.2G, 2.2H).

To further scrutinize specificity of ZFP36 in human-derived ECs, we first compared the 3'UTRs of mouse and human Jag1 sequences and generated reporter constructs. A control construct with the full mJag1-3'UTR (FL) and a second construct where the region corresponding to the major CLIP peak was deleted (Δ) (Figure 2.3A, 2.3B). Wild-type endothelial cells infected with the resulting lentiviruses clearly confirmed the relevance of this binding-region of the Jag1 mRNA for regulation by endogenous ZFP36. The ARE-deleted construct exhibited higher mean nuclear GFP (reporter) than the full-length construct (Figure 2.3C, 2.3D). With additional VEGF stimulation, we also observed decreased fluorescent signal in both mFL and mΔ transfected cells. There are several possible interpretations of our findings. We expected that VEGF would naturally increase mRNA-decay activity with its induction and therefore as predicted we saw a decrease in mFL transfected cells. The mΔ construct, while it no longer had the peak binding sequence, still retained other ARE motifs that could potentially bind to Zfp36 albeit with reduced affinity. This idea was supported by the fact that the VEGF-mediated reductions found in mFL cells were still significantly lower than mΔ transfected cells. Alternatively, ZFP family members ZFP36L1 and ZFP36L2 could also have potential redundancy in transcript binding. Though we did not perform transcript binding analysis with other family members L1 and L2, because they did not exhibit sensitivity to VEGF (Figure 2.1C), we predicted that in this specific context they may not contribute

to Jag1 transcript stability. Moreover, while visually pleasing, the relatively stable half-life (~26h) of GFP might not be ideal to assess decay dynamics of a relatively rapid post-transcriptional mechanism. Thus, similar experiments were also performed with luciferase reporters using the human 3'UTR sequence (Figure 2.3E-G). An additional benefit of using a dual luciferase assay is the differential read-out (more quantitative) in relation to a co-transfected independent control vector allows us to also normalize for transfection efficiency. In control cells, deletion of the homologous human peak binding region (hΔ) increased level of luciferase by 2-fold, an effect that was achieved at baseline in ZFP36 null cells with the full-length construct (hFL) (Figure 2.3F). When transfections were done in the presence or absence of VEGF (to modulate ZFP36 levels) differences were clearly exacerbated, as per the trending difference in full length JAG1-3'UTR (FL) in control cells (Figure 2.3G). These effects were no longer observed when either the binding region was removed (Δ transfected cells) or in the context of *ZFP36* KO cells.

2.2.3 - ZFP36 affects Notch signaling and sprouting angiogenesis by altering Jag1 expression.

Notch signaling is initiated by binding to transmembrane ligands that interact with Notch receptors in *trans.* For this, the expression of the receptor (Notch) should be in one cell and expression of the ligand (Dll4, Jag1 and others) in an adjacent cell. Conversely, when receptor and ligand are both located on the same cell, paring of receptor-ligand at the cell surface in *cis* which leads to suppression of the pathway.[12] To test the effects of ZFP36 deletion and resulting elevated levels of Jagged1 on Notch signaling, we examined nuclear presence of Notch intracellular domain (NICD) in *ZFP36* KO and control cells. These experiments were conducted in confluent cultures, as per integrity of continuous VE-Cadherin, to ensure trans activation of the Notch pathway. Control and *ZFP36* KO cultures were either exposed to vehicle or VEGF for 1 h, a time consistent with induction of ZFP36. We found that VEGF-treated cells had lower levels of NICD in the nucleus, reflecting lower Notch signaling. Importantly, in the case of *ZFP36* KO cells, both control

and VEGF-treated cells showed a noticeable reduction in nuclear NICD (Figure 2.4A, 2.4B). The findings indicate that excess Jag1 due to the absence of ZFP36 regulation is sufficient to tilt the delicate balance of *cis*- versus *trans*- ligand-receptor interactions and alter the levels of Notch signaling, as per abundance of nuclear NOTCH 1. When presenting control and *ZFP36* KO HUVECs with exogenous ligand for 24 h, this decrease in Notch signaling was no longer significantly reduced and the cells appeared to signal at levels equivalent to control. This suggests that heterotypic interactions could mitigate the effects of potential *cis*-inhibition (Figure S2.4A-D). Further functional implications of the above findings were pursued using sprouting bead assays *in vitro* with control and *ZFP36* KO HUVECs (Figure 2.4C-G). Interestingly, we found that absence of ZFP36 yielded a significant increase in the number and in the length of the sprouts that was not driven by differences in cell number (Figure 2.4G).

2.3 – DISCUSSION

In this *in vitro* work, we established that VEGF signaling induces ZFP36 in a transcriptionally-dependent manner resulting in a burst of protein expression that subsides relatively quickly. In turn, we identified *Jag1* transcript as a target of ZFP36 and validated a role for this RNA binding protein in post-transcriptional stability of Jagged1 *in vitro* and *in vivo*. We showed that endothelial cells lacking ZFP36 exhibit constitutive higher levels of Jagged protein, reduced Notch1 signaling, and increased sprouting angiogenesis. From these observations, we present a critical functional role for ZFP36 as a post-transcriptional regulator of endothelial Notch signaling downstream VEGF.

The ZPF36 family, which also includes ZFP36L1 and ZFP36L2, are RNA binding proteins involved in sequestration and / or decay of ARE-containing mRNAs.[13,14] Through recognition and selective mRNA binding, they are able to regulate metabolic pathways, inflammation, and immunity.[3,4,14-17] Furthermore a role ZFP36 in facilitating quick adaptive switches, particularly during inflammatory settings, has been highlighted in several pathological conditions, partially due

to its rapid and robust induction by several cytokines.[3,6,8-11,18-20] Interestingly, the findings presented here indicate that ZFP36 can also modulate developmental processes, such as angiogenesis, downstream VEGF signaling. Importantly, we showed that induction of ZFP36 by VEGF is temporally restricted and presumably associated with the recycling of VEGFR2. Although we did not experimentally demonstrate the mechanisms responsible for ZFP36 reduction, it has been recognized its activity, localization, and stability are regulated by phosphorylation.[6] Intriguingly some of the kinases involved in ZFP36 post-translational modifications are also downstream of VEGF, indicating a feedback loop of robust production and degradation. We suspect these specific pulses of induction impose oscillatory cycles of regulation that refine and optimize the angiogenic process.

2.4 AUTHOR CONTRIBUTIONS

Conceptualization, HLS and MLIA; Methodology, HLS, ACC; Validation, HLS and ACC; Formal Analysis, HLS, ACC, KEKU; Investigation HLS and ACC; Resources, ACC, KEKU, HRC; Data Curation, KEKU; Writing – Original Draft, HLS and MLIA; Writing – Review & Editing HLS, ACC, HRC, TAV, and MLIA; Funding Acquisition, HLS and MLIA; Supervision, HRC, TAV, and MLIA.

2.5 – METHODS

2.5.1 Resource availability

Materials used in this study are commercially available. RNA-seq data generated for this study were deposited at GEO and will be publicly available upon publication. This study also analyzes existing, publicly available data. Accession numbers and detailed material information can be found in the key resources table below.

2.5.2 Experimental models

Endothelial cells (HUVECs, HAECs, and HDMECs) were cultured with 10% fetal bovine serum (FBS) (Omega Scientific #FB-11) in either MCDB-131 (VEC Technologies; MCDB131-WOFBS)

or EBM-2 Basal Medium (Lonza; CC-3156) supplemented with 1% penicillin/streptomycin and EGM-2 supplements (Lonza; CC-4176) sans kit FBS. HEK293T and MEF cell lines were cultured in DMEM containing 1 mM pyruvate and 4 mM glutamine supplemented with 10% FBS and 1% penicillin/streptomycin in a humidified incubator at 37°C with 5% CO_2 and atmospheric oxygen. MEF isolation, immortalization and adenoviral treatments were performed as previously described.[3]

2.5.3 Method details

Cell culture treatments:

VEGF and serum stimulation

Stock recombinant Human $VEGFA_{165}$ (VEGF) (Peprotech) was prepared in sterile molecular grade water in single-use aliquots. After washing cells once with serum-free media, cells were serum starved overnight followed by direct application of VEGF at a final concentration of 100 ng/mL for indicated times. In the case of 10% FBS treatments (MEF experiments), FBS was re-introduced as in standard culture conditions (10% final concentration) post-overnight serum starvation.

VEGF burst experiment

Cultured HUVECs were washed once in serum-free media and serum-starved overnight before adding VEGF directly to culture media as described above. At indicated times cells were washed twice with serum-free media to remove VEGF. Leaving on the second wash, all cultures were harvested for protein after total time of 1 h to examine ZFP36 induction.

Inhibitor treatments

ZM323881 hydrochloride (ZM323) (Tocris) and Actinomycin D (ActD) (Invitrogen) stock solutions were prepared according to manufacturer's instructions. After overnight serum starvation

described above, ZM323 or ActD was added directly to culture media 1 h prior to VEGF time course experiments at a final concentration of 1 μM and 10 μg/mL respectively.

Lentivirus production and infection

Lentivirus particles were produced in 293T cells by co-transfecting with a construct of interest and second-generation packaging plasmids psPAX2 and pMD2.G (Addgene; gift from Didier Trono). At 24 and 48 hours, lentivirus-rich medium was collected and pooled. After centrifuging 1250 rpm for 5 min, supernatant was filtered (0.22 μm) and aliquot for single use and frozen at -80°C for long term storage. For transduction on HUVECs, aliquots were applied directly to cells overnight in the presence of 8 μg/mL polybrene. Infected cells were cultured in regular growth medium for 48 h prior to beginning puromycin (1 mg/mL) antibiotic selection where applicable.

Migration Assay

Cells were seeded in 96-well image lock plates (Essen Bioscience) to confluence. After waiting for adherence (4-6h) scratches were made in each well using Incucyte Woundmaker tool according to manufacturer instructions. Cells were washed twice with culture media to remove cell debris. Automated time course imaging was performed using Incucyte S3 (Sartorius) in humidified incubator at 37°C with 5% CO_2 set to capture each well every hour until wound closure. Analysis was performed using ImageJ software plugin for wound healing analysis.[21]

Proliferation Assay

Control or *ZFP36* KO HUVECs infected with lentivirus CMV-GFP were seeded in 96-well plates at 5,000 cells per well. Automated image capture was performed using Incucyte S3 (Sartorius) in humidified incubator at 37°C with 5% CO_2 and set to capture both phase and GFP images every hour until confluence was reached. Media was changed every other day as necessary. Confluence analysis was performed using ImageJ. Briefly, GFP images were binarized to calculate Area Fraction of endothelial coverage in the field of view over time.

JAG1-UTR construct experiments and staining

Lentivirus constructs were manufactured through VectorBuilder custom lentivirus gene expression packaging service. HUVECs were infected according to manufacturer's instructions using MOI 4 with 8 µg/mL final concentration polybrene. HUVEC infection and puromycin selection were otherwise performed as described above. After VEGF stimulation, Cells were fixed with 4% (wt/vol) paraformaldehyde diluted in 1xPBS (PFA) for 10 min at room temp. After three 5 min washes in 1xPBS cells were directly stained for 30 min with Alx647 conjugated-VE-CAD clone Hec1 antibody (graciously provided by Dr. William Muller - Northwestern University, Chicago) and DAPI. After three additional 5 min washes in 1xPBS cells were directly imaged.

Luciferase reporter assay

Plasmid constructs were manufactured through VectorBuilder custom design vector services. Control or *ZFP36* KO HUVECs were trypsinized and transfected in suspension using Lipofectamine 3000 (Thermo Fisher) according to manufacturer's instructions and seeded to opaque-white 96-well clear-bottom culture plates. For each L3000 reaction, a *Renilla* Luciferase reporter was co-transfected 10:1 (Firefly to *Renilla*) for normalization of transfection efficiency. After 24h, plates were media changed and cells were allowed to recover post-transfection. Luciferase activity was measured the following day using DualGlo Luciferase Assay System (Promega) according to the manufacturer's instructions. For VEGF stimulation, serum starvation was performed overnight after the 24h media change and VEGF was added the following day at indicated times before measurement.

Jag1-Fc coated culture plates

Recombinant human Jagged 1 Fc Chimera (R&D systems) was reconstituted according to manufacturer's instructions (200 µg/mL in sterile 1xPBS) and stored frozen at -80°C in single use aliquots. This stock or control human IgG, Fc fragment (Sigma-Aldrich) was diluted to final concentration of 10 µg/mL and incubated rocking overnight at 4°C in respective wells of 12-well

culture plate. Wells were washed once with sterile 1xPBS, and cells were seeded in wells to confluence. After 24 h, cell lysates were harvested for immunoblotting or quantitative RT-PCR.

Bulk RNA-seq analysis

Total RNA was extracted and purified using RNeasy mini kit (Qiagen) according to manufacturer's instructions. RNA libraries were prepared using the Illumina TruSeq Total RNA library prep kit according to manufacturer's instructions. Following barcoding, 18 samples per lane were sequenced on a HiSeq3000 using 50 bp single-end protocol. Reads were QC'd using FastQC in batch mode and mapped to the mouse genome (mm10) using STAR aligner version 2.3.1. The count data were normalized using DESeq2′s median of ratios method.[22] Differential expression analysis was performed using DEseq2 with statistically significant genes called using adjusted p-value cutoffs of less than 0.1.[23]

Cell lysis and immunoblotting

Cells were lysed in modified RIPA buffer (50 mM Tris pH8, 150 mM NaCl, 0.5% w/v Na-Desoxycholate, 1% w/v Triton-X100, 0.1% w/v SDS, 200 µM Na_3VO_4, 1x protease inhibitor cocktail) after washing once with cold 1xPBS. Lysates were then denatured with Laemmli buffer for 10 min at 95°C. Denatured protein lysates were separated by SDS-PAGE gradient (4–20%) gel (Bio-Rad) and transferred using 20 min semi-dry transfer using Trans-blot Turbo (Bio-Rad) onto nitrocellulose membranes and incubated overnight at 4°C with primary antibodies (see Key Resource Table). HRP-conjugated secondary antibodies (1:10,000) were applied in species dependent manner at room temperature for 1 h. Immuno-complexes were detected by enhanced chemiluminescence with SuperSignal™ West Pico PLUS or Femto Maximum Sensitivity Substrate (Thermo Fisher) using ChemiDoc Imaging system (Bio-Rad). Quantification of bands by densitometry analysis was performed using ImageLab Software (Bio-Rad).

Quantitative RT-PCR

Total RNA from cell culture was extracted and purified using RNeasy mini kit (Qiagen) according to manufacturer's instructions. Complementary DNA synthesis was performed with Superscript III reverse transcription First-Strand synthesis kit (Invitrogen). qPCR was performed for each sample in duplicate and gene expression was normalized with the housekeeping gene (HPRT) and relative expression calculated using the ΔΔCt method. Primer sets were synthesized by Integrated DNA Technologies, Inc (Primer sequences listed in key resource table).

Immunocytochemistry

Staining and imaging

Cells cultured on glass bottom 6 or 12-well plates (Cell Vis) were fixed with 2% PFA for 15 min followed by permeabilization with blocking buffer (3% v/v normal donkey serum, 0.3% v/v Triton-X100, and 0.05% v/v Tween-20 diluted in 1xPBS) for 1 h at room temperature. Primary antibodies (listed in key resource table) were incubated overnight at 4°C diluted in blocking buffer. After washing 3x5 min with 1xPBS, fluorescent-tagged secondary antibodies were applied and incubated for 1 h at room temperature. After washing another 3x5min with 1xPBS, imaging was performed using A1R HD25 confocal microscope (Nikon) using x20 objective. Z-stack scan feature was used to capture cell volume. For figure images, Denoise.AI (Nikon) was employed to remove Poisson shot noise.

Image Analysis

Cell mean fluorescence intensity (MFI) measurements were quantified on non-denoised images using Imaris software (Imaris 9.9.0, Bitplane) 'Cells' feature. Where applicable, VECAD was used for cell borders and DAPI for nuclear area. MFI was calculated per cell or as an average of cells within field of view. In the case of Notch1, MFI was calculated as a fraction of nuclear/cytosolic as a proxy for pathway activation.

eCLIP-seq processing and analysis

This paper analyzes existing, publicly available data.[3] Accession numbers for the datasets are listed in the key resources table. Reads were processed and aligned as previously described. Briefly, reads were aligned to the mouse mm10 genome. Then using a combination of umi_tools[24], cutadapt[25], and STAR[26] sequences were aligned and de-duplicated. Peaks were called with pureclip[27], using an input control for each CLIP library. To identify ZFP36-specific peaks, peaks were identified in both the *Zfp36/l1/l2* wildtype (WT) and triple knockout (TKO) MEF conditions for each library; peaks identified in TKO.1 libraries were excluded from all downstream analyses.

ARE site alignment

Adenosine-uridine rich element (ARE) motifs in mouse *Jag1* and human *JAG1* 3'UTR were identified using publicly available database ARE site2 using all available default motifs.[28] Bed files were extracted and aligned to genomes (mm10 and hg38 respectively) using Integrative Genomics Viewer. Overlapping sequences were collapsed for final presentation and aligned to available eCLIP binding peaks.

CLIP-qPCR

CLIP-qPCR validation of sequencing was performed as previously described.[3] Briefly, *Zfp36/l1/l2* wildtype (WT) or triple knockout (TKO.1) MEFs were serum deprived overnight, stimulated for 40 min with 10% FBS, UV-irradiated, snap frozen, and stored at -80°C as described for eCLIP-seq experiments.[3] At the time of lysis, DNase digestion was performed for 5 min at 37°C. Importantly, RNase inhibitor was added to the lysates and no RNase digestion step was performed to ensure recovery of full-length transcripts in complex with ZFP36. Protein quantification using a BCA assay was performed to ensure equal amounts of protein from WT or TKO.1 MEF conditions were used for subsequent immunoprecipitation (IP). For each IP, 100 µl Protein A Dynabeads pre-conjugated with 25 µg anti-ZFP36 antibody (Millipore ABE285) was incubated rocking for 1 h at 4°C. On-bead Proteinase K (NEB) digestion was performed to release RNA, which was then purified with acid-

phenol:chloroform, pH 4.5 (with IAA, 125:24:1) and concentrated to 20 µl final volume (Zymo). Isolated RNA was used for cDNA synthesis (Bio-Rad; iScript), then diluted 5-fold in nuclease-free water in preparation for qPCR using QuantStudio5 (Applied Biosystems). Relative ZFP36 binding enrichment to target mRNAs over background was calculated according to previously described methods deriving ΔΔCt with *Rplpo* as the reference gene for IP samples.[29] *Tuba1b* was used as a negative control, *Ptgs2* served as a positive control. Data are presented as ZFP36 target binding enrichment fold change relative to TKO.1 cells; signal from TKO.1 conditions is independent of ZFP36. (Primer sequences listed in Supplementary Table S1).

Microcarrier bead angiogenesis assay

Microcarrier bead cell coating

The microbead angiogenesis assay was performed as previously described.[30] Briefly, trypsinized HUVECs were coated on dextran-coated microcarrier beads at a ratio of approximately 400:1. Coated beads were rested overnight in culture media in humidified incubator at 37°C with 5% CO_2 and atmospheric oxygen. The next day beads were washed and resuspended at 500 beads/mL in PBS solution containing 10 mg/mL fibrinogen & 15 U/mL aprotinin. This mixture was then carefully mixed inside 24-well glass bottom well containing a droplet of 10 U/mL thrombin to form and embed the HUVEC coated beads in fibrin gel. After polymerization, sprouting was allowed to occur for 24 h.

Staining and imaging

After 24 h, wells were fixed with 4% PFA followed by permeabilization with blocking buffer (3% v/v normal donkey serum, 0.3% v/v Triton-X100, and 0.05% v/v Tween-20 diluted in 1xPBS) for 1 h at room temperature. Phalloidin and Hoechst diluted in blocking buffer were incubated overnight at 4°C. Imaging was performed using a CSU-W1 confocal microscope (Nikon) with x20 objective. Z-stack scan feature was used to capture entire bead and sprouting volume. For figure images, Denoise.AI (Nikon) was employed to remove Poisson shot noise.

Image analysis

Non-denoised z-stack images were imported to ImageJ for analysis. From maximum intensity projections, bead area was manually masked for exclusion and individual channels were threshold (Li algorithm) to obtain overall measured phalloidin area and nuclei counts. To assess outgrowth distance, Euclidean distance maps (binary with 10 iterations) were generated from each bead mask. The binary phalloidin area was used to generate a selection area. This area was then restored on distance maps to generate a histogram of positive pixels over radial distance. Histogram data was compiled, and pixel distance converted to microns.

Quantification and statistical analysis

Statistical parameters were calculated using Prism 8 (Graphpad) and are specified in figure legends. Unless otherwise stated, we calculated p-values for time course datasets using non-parametric Kruskal-Wallis with post-hoc Dunn's multiple comparison test. For single comparisons we used Mann-Whitney tests. All significant results, defined as having a p-value < 0.05, are specified for each figure.

Table 2.1 – Key resource table

REAGENT or RESOURCE	SOURCE	IDENTIFIER
Antibodies		
Rabbit polyclonal anti-BRF1/2	Cell Signaling Tech	Cat#2119; RRID: AB_10695874
Goat polyclonal anti-CDH5	R&D Systems	Cat#AF938; RRID: AB_355726
Rabbit polyclonal anti-gamma-Tubulin	Abcam	Cat#11321; RRID: AB_297926
Mouse monoclonal anti-GAPDH	Millipore Sigma	Cat#MAB374; RRID: AB_2107445
Rabbit monoclonal anti-JAG1	Cell Signaling Tech	Cat#2620; RRID: AB_10693295
Mouse monoclonal anti-JAG1 (E-12)	Santa Cruz	Cat#Sc-390177; RRID: AB_2892141
Rabbit monoclonal anti-NICD (Val1744)	Cell Signaling Tech	Cat#4147; RRID: AB_2153348
Rabbit monoclonal anti-Notch1	Cell Signaling Tech	Cat#3608; RRID: AB_2153354

Rabbit monoclonal anti-phospho-VR2 (Tyr1175)	Cell Signaling Tech	Cat#2478; RRID: AB_31377
Rabbit monoclonal anti-VR2	Cell Signaling Tech	Cat#2479; RRID: AB_2212507
Rabbit monoclonal anti-ZFP36	Cell Signaling Tech	Cat#71632; RRID: AB_2799806
Rabbit polyclonal anti-ZFP36	Millipore Sigma	Cat#ABE285; RRID: AB_11205589
Bacterial and virus strains		
Ad-Cre-GFP	Vector Biolabs	Cat#1700
Ad-GFP	Vector Biolabs	Cat#1060
lentiCRISPR v2	Sanjana et al.[31]	Cat#52961; RRID:Addgene_52961
Biological samples		
Human umbilical vein endothelial cells	Lonza	Cat# C2517A; Lot# 18TL072772, 18TL072771, 18TL061650, 21TL169354, 21TL195719, 20TL293905, 0000632996, 0000296747
Human umbilical vein endothelial cells, pooled	Lonza	Cat#C2519A; Lot#0000460587
Human aortic endothelial cells	University of California, Los Angeles	N/A
Human Dermal Microvascular Endothelial Cells	PromoCell	Cat#C-12212
Chemicals, peptides, and recombinant proteins		
ZM323881 hydrochloride	Tocris	Cat#2475/1
Actinomycin D	Invitrogen	Cat#A7592
$VEGFA_{165}$	Peprotech	Cat#100-20
Recombinant human Jagged 1 Fc Chimera	R&D systems	Cat#1277
Human IgG, Fc fragment	Sigma-Aldrich	Cat#AG714
eBioscience™ 1xRBC lysis buffer	Invitrogen	Cat#00-4333-57
Lipofectamine™ 2000	Thermo Fisher	Cat#11668019
Restore™ Western Blot Stripping Buffer	Thermo Fisher	Cat#21059
Dynabeads™ Protein A	Thermo Fisher	Cat#10001D
ProLong Gold Antifade Mountant	Thermo Fisher	Cat#P36930
Puromycin	Invitrogen	Cat#ANTPR1
Polybrene	Millipore Sigma	Cat#TR-1003-G
cOmplete™ EDTA-free Protease Inhibitor Cocktail	Sigma-Aldrich	Cat#11873580001
Recombinant Human Jagged 1 Fc Chimera Protein, CF	R&D Systems	Cat#1277-JG-050
Cytodex 3 microcarriers	Cytiva	Cat#17048501
Fibronogen	Sigma-Aldrich	Cat#F-8630

Aprotinin	Sigma-Aldrich	Cat#A-1153
Thrombin	Sigma-Aldrich	Cat#T-3399
2.5% Trypsin, 10x	Corning	Cat#MT25054CI
Paraformaldehyde (PFA) 4%, in PBS	Thermo Fisher	Cat#AAJ61899AP
Triton-X100	Thermo Fisher	Cat#BP151500
Tween-20	Sigma-Aldrich	Cat#P9416
Normal Donkey Serum	Jackson ImmunoResearch	Cat#017-000-121
Proteinase K	New England Biolabs	Cat# P8107S
Phalloidin-AF488	Thermo Fisher	Cat#A12379
Hoechst 33342	Enzo	Cat#ENZ-52401
Critical commercial assays		
RNeasy Plus Micro Kit	Qiagen	Cat#74034
RNeasy Mini Kit	Qiagen	Cat#74104
TruSeq Total RNA library prep kit	Illumina	Cat#20020594
Trans-Blot® Turbo™ RTA Midi Nitrocellulose Transfer Kit	Bio-Rad	Cat#1704271
Thermo Scientific Pierce Detergent Compatible Bradford Assay	Fisher Scientific	Cat#PI23246
Pierce™ BCA Protein Assay Kit	Thermo Fisher	Cat#23227
4–20% Mini-PROTEAN® TGX™ Precast Protein Gels	Bio-Rad	Cat#4561095, 4561094
4–20% Criterion™ TGX Stain-Free™ Protein Gel	Bio-Rad	Cat#5678093
Superscript™ III First-Strand Synthesis System	Invitrogen	Cat#18080051
SsoAdvanced Universal SYBR® Green Supermix	Bio-Rad	Cat#1725274
Dual-Glo® Luciferase Assay System	Promega	Cat#E2940
Lipofectamine 3000 Transfection Reagent	Thermo Fisher	Cat#L3000015
Protein A Dynabeads	Thermo Fisher	Cat#10001D
RNA Clean & Concentrator	Zymo Research	Cat#R1017
iScript™ cDNA Synthesis Kit	Bio-Rad	Cat#170-8891
Deposited data		
HUVEC RNAseq	This paper	GSE235462
eCLIP-seq	Cicchetto et al.[3]	PRJNA943291
Experimental models: Cell lines		
Lenti-X 293T	Takara	Cat#632180
Oligonucleotides		
qPCR primers (Table S1)	See Table S1	N/A
gRNA ZFP36 Forward: CACCGTGCCCGTGCCATCCGACCA	This paper	N/A
gRNA ZFP36 Reverse: AAACTGGTCGGATGGCACGGGCAC	This paper	N/A
Recombinant DNA		

pLV[Exp]-Puro-EF1A>NLS-EGFP :{mJag1_3'UTR_565bp}	This Paper - Vector Builder custom order	Cat#VB220720-1510tzf
pLV[Exp]-Puro-EF1A>NLS-EGFP :{mJag1_3'UTR_517bp(del 48bp)}	This Paper - Vector Builder custom order	Cat#VB220720-1515agk
pRP[Exp]-Hygro-CAG-Luciferase&{hJAG1_3UTR_1814bp}	This Paper – Vector Builder custom order	Cat#VB230730-1401fzh
pRP[Exp]-Hygro-CAG-Luciferase&{hJAG1_3UTR'(del 331bp-429bp)}	This Paper – Vector Builder custom order	Cat#VB230807-1714sjb
psPAX2	Addgene	Cat# 12260 RRID: Addgene_12260
pMD2.G	Addgene	Cat# 12259 RRID: Addgene_12259
pCMV-GFP	Matsuda et al.[33]	Cat#11153 RRID: Addgene_11153
Software and algorithms		
FIJI	Schindelin et al.[34]	RRID:SCR_002285
Imaris (v9.9.0)	Bitplane	RRID:SCR_007370
NIS Elements	Nikon	RRID:SCR_014329
Image Lab Software	BioRad	RRID:SCR_014210
CFX Manager (v3.1)	BioRad	RRID:SCR_017251
STAR (v2.7.3)	Dobin et al.[26]	RRID:SCR_004463
BioRender	BioRender	RRID:SCR_018361
Adobe Illustrator	Adobe	RRID:SCR_010279
Prism 9	Graphpad	RRID:SCR_002798
UMI-tools	GitHub	RRID:SCR_017048
PureCLIP	GitHub	https://github.com/skrakau/PureCLIP
DESeq2	GitHub	RRID:SCR_015687
FastQC	GitHub	RRID:SCR_014583
AREsite2	Gruber et al.[28]	http://nibiru.tbi.univie.ac.at/AREsite2/welcome
BioTek Gen5	Agilent	RRID:SCR_017317
QuantStudio 5	Applied Biosystems	RRID:SCR_020240
Wound_healing_size_tool	Suarez-Arnedo et al.[35]	https://github.com/AlejandraArnedo/Wound-healing-size-tool/wiki
Other		
HiSeq3000	Illumina	Cat#SY-401-3001
IncuCyte S3 Live Cell Analysis System	Sartorius	Cat#4647 RRID:SCR_023147
Glass bottom well-plates	Cell Vis	Cat# P06-1.5H-N, P12-1.5H-N, P24-1.5H-N
BioTek Synergy H1 Microplate Reader	Agilent	Cat#SH1M2-SN RRID:SCR_019748
Incucyte® Wound Maker 96-Tool	Sartorius	Cat# 4563

Supplemental Table S1 – qPCR primers

Gene	Forward (5' to 3')	Reverse (5' to 3')	Species	Source
ZFP36	GACTGAGCTATGTC GGACCTT	GAGTTCCGTCTTGTA TTTGGGG	Human	This paper
ZFP36L1	GATGACCACCACCC TCGT	TGGGAGCACTATAGT TGAGCATC	Human	This paper
ZFP36L2	CTGCTGCTGACTGC GGTA	ATCCAGACCCACAAC TTTGC	Human	This paper
JAG1	GACTCATCAGCCGT GTCTCA	TGGGGAACACTCAC ACTCAA	Human	This paper
HPRT	GCCCTGGCGTCGTG ATTAGT	AGCAAGACGTTCAGT CCTGTC	Human	Mack et al[32]
Jag1	CGTAGAGTACACTG CCTGCC	CAAGTATCTCCCCAG TCCCG	Mouse	This paper
Tuba1b	GAGACCCGGTGTCT GCTTC	GAGATGCACTCACG CATGATA	Mouse	Cicchetto et al[3]
Ptgs2	TGAGTACCGCAAAC GCTTCT	CAGCCATTTCCTTCT CTCCTGT	Mouse	Cicchetto et al[3]
Rplpo	CACTGGTCTAGGAC CCGAGAAG	GGTGCCTCTGGAGA TTTTCG	Mouse	Cicchetto et al[3]

2.6 - FIGURES

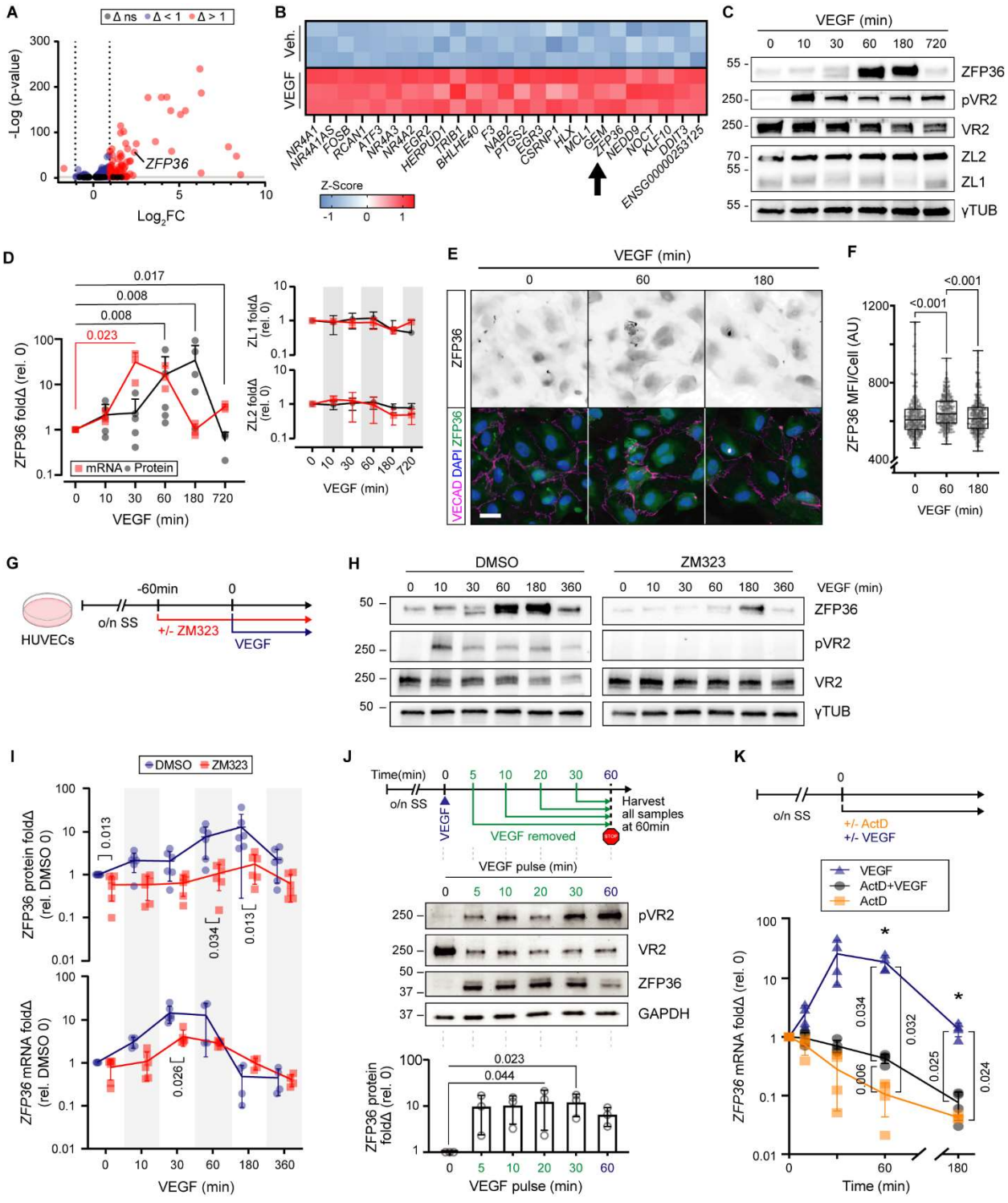

Figure 2.1 - VEGF triggers a robust induction of ZFP36 in endothelial cells.

(A) Volcano plot of RNAseq differential expression Log_2fold change (Δ) of HUVECs +/- VEGF for 1h. Non-significant (ns) cutoff set to -Log(p)>2. **(B)** Z-score heatmap of top 25 differentially

expressed genes after exposure to vehicle (Ctrl) or $VEGF_{165}$ (100 ng/mL) for 1 h (n = 3 biological replicates). **(C)** Representative immunoblots of ZFP36, phospho-VEGFR2 (pVR2), VEGFR2 (VR2), ZFP36L1 (ZL1), ZFP36L2 (ZL2), and γTubulin (γTUB) from HUVEC lysates after VEGF stimulation for the indicated times. **(D)** Immunoblot quantification of fold change (Δ) relative to control (n = 5 biological; except t =720, n = 3 biological replicates) and qPCR transcripts of ZFP36, ZFP36L1, and ZFP36L2 (n = 3 biological replicates). Data for ZFP36 are individual replicates with line representing mean. Data for ZFP36L1 and ZFP36L2 are represented with mean ± SD. Statistical analysis with Mann-Whitney test. **(E)** Representative immunofluorescence of ZFP36, VE-Cadherin (VECAD) and DAPI on HUVECs treated with or without VEGF at indicated times (scale bar = 25 μm). **(F)** Quantification of ZFP36 mean fluorescent intensity (MFI) per cell (n = 300 cells). Data are presented as individual replicates with overlaid box extending from the 25th to 75th percentiles with whiskers showing min and max values. Statistics: Kruskal-Wallis with post-hoc Dunn's multiple comparison test. **(G)** Experimental design. Confluent HUVEC monolayers were exposed to VEGFR2 inhibitor ZM323881 (ZM323) or vehicle for 1 h following overnight serum starvation (SS), followed by $VEGF_{165}$ stimulation. **(H)** Representative immunoblots of ZFP36, phospho-VEGFR2 (pVR2), VEGFR2 (VR2), and γTubulin (γTUB) from HUVECs treated in VEGF time course with or without ZM323. **(I)** Quantification of immunoblot (n=5 biological replicates) and qPCR transcripts (n=4-6, combination of technical replicates with minimum of 3 biological replicates) for ZFP36 after VEGF time course in the presence or absence of ZM323. Data presented are individual replicates with connecting line representing mean ± SD. Statistics: multiple Mann Whitney tests with Holm-Šídák method to adjust for multiple comparisons. **(J)** Experimental design of pulse-chase VEGF treatment with associated representative WB and quantification. WB quantification is presented with individual replicates and mean ± SD relative to control (n=3 biological replicates). Statistics: Freidman's test with post-hoc Dunn's multiple comparison test. **(K)** Experimental design of Actinomycin D (ActD) treatment and qPCR quantification of mRNA normalized to *HPRT* (n = 4 biological replicates) mean fold change ± SD relative to control. Kruskal-Wallis with post-hoc Dunn's multiple comparison test.
Abbreviations: human umbilical vascular endothelial cells (HUVECs), overnight serum starvation (o/n SS).

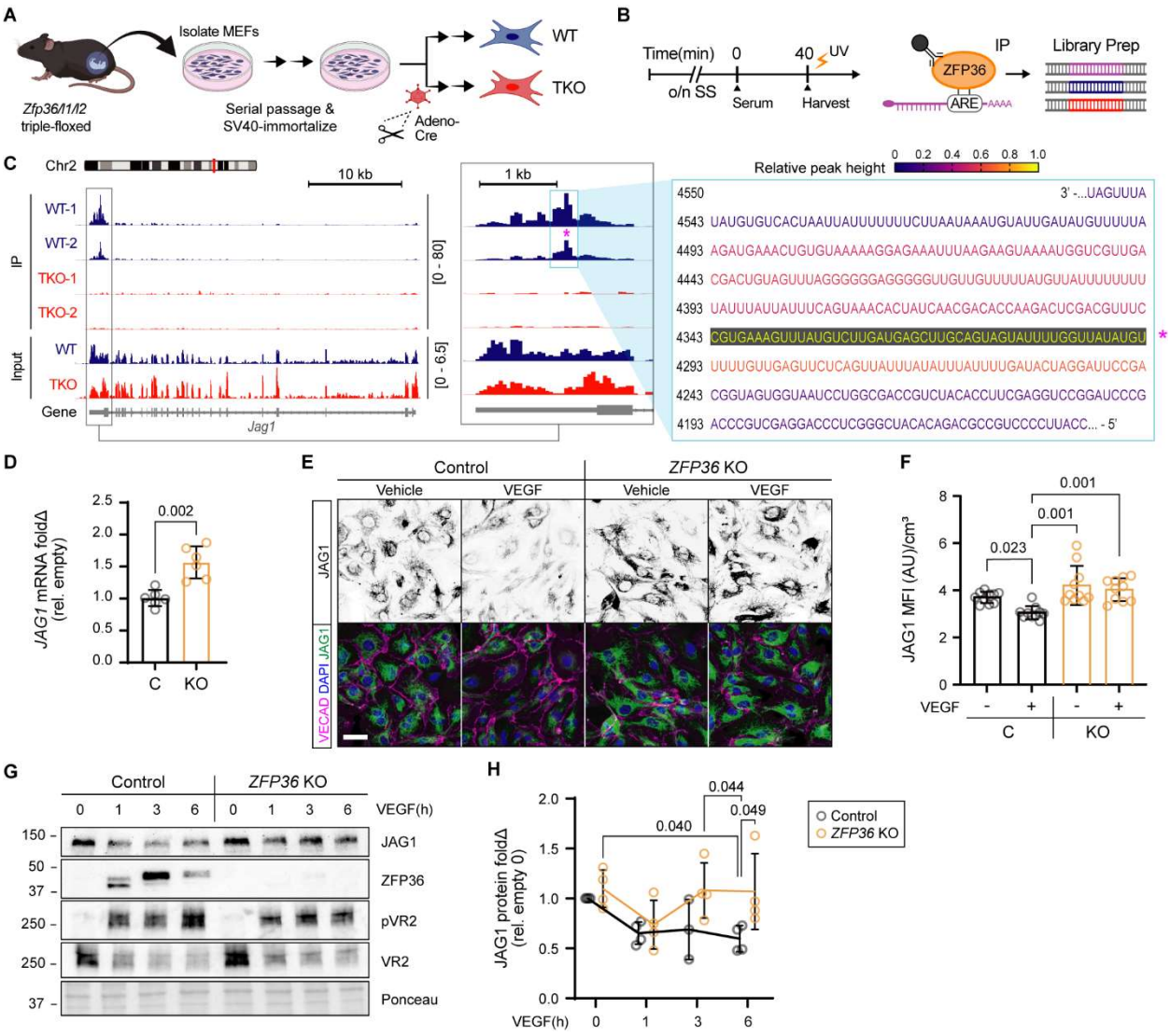

Figure 2.2 - Jagged1 is a direct target for ZFP36 binding.

(A) Schematic for generation of Zfp36/l1/l2 triple-floxed MEF cells and adenoviral-based approach for *in vitro* Cre-recombinase delivery (adeno-Cre), or GFP control (adeno-GFP), to derive *Zfp36/l1/l2* triple-foxed wild type (WT) and triple-floxed knockout (TKO) cells from an isogenic cell population. **(B)** Schematic of experimental design for eCLIP. **(C)** Integrative Genomics Viewer generated from eCLIP-seq data showing the ZFP36 binding site on Jag1 mRNA within 3'UTR. Track height scale denoted in brackets. Relative peak height from clip data was used to color code corresponding mRNA nucleotides associated with highest binding peak (*). **(D)** Quantification of *JAG1* mRNA mean fold change (Δ) ± SD by qPCR from CRISPR control and *ZFP36* KO HUVECs normalized to *HPRT* (n = 3 biological replicates, 2 technical replicates each). Statistics: Kruskal-Wallis with post-hoc Dunn's multiple comparison test. **(E)** Representative immunofluorescence of JAG1, VECAD, and DAPI in CRISPR control and ZFP36 KO HUVECs

treated with or without VEGF for 1 h (scale bar = 50 μm). **(F)** Quantification of Jag1 MFI ± SD normalized to cell volume per field of view (n = 10 fields). Statistics: Kruskal-Wallis with post-hoc Dunn's multiple comparison test. **(G)** Representative immunoblots of JAG1, ZFP36, pVR2 and VR2, protein expression from CRISPR control and *ZFP36* KO HUVECs stimulated with VEGF at indicated times. Included corresponding Ponceau stain is used as loading control reference. **(H)** Quantification of WB results fold change (Δ) relative to empty control and normalized to total protein (n = 3 biological replicates with an additional technical replicate in all but Control 3h). Data presented are individual replicates with connecting line representing mean ± SD. Statistical analysis using mixed-effects analysis with post-hoc Tukey's multiple comparison test.
Abbreviations: Mouse embryonic fibroblasts (MEFs), CRISPR control (C), ZFP36 KO (KO)

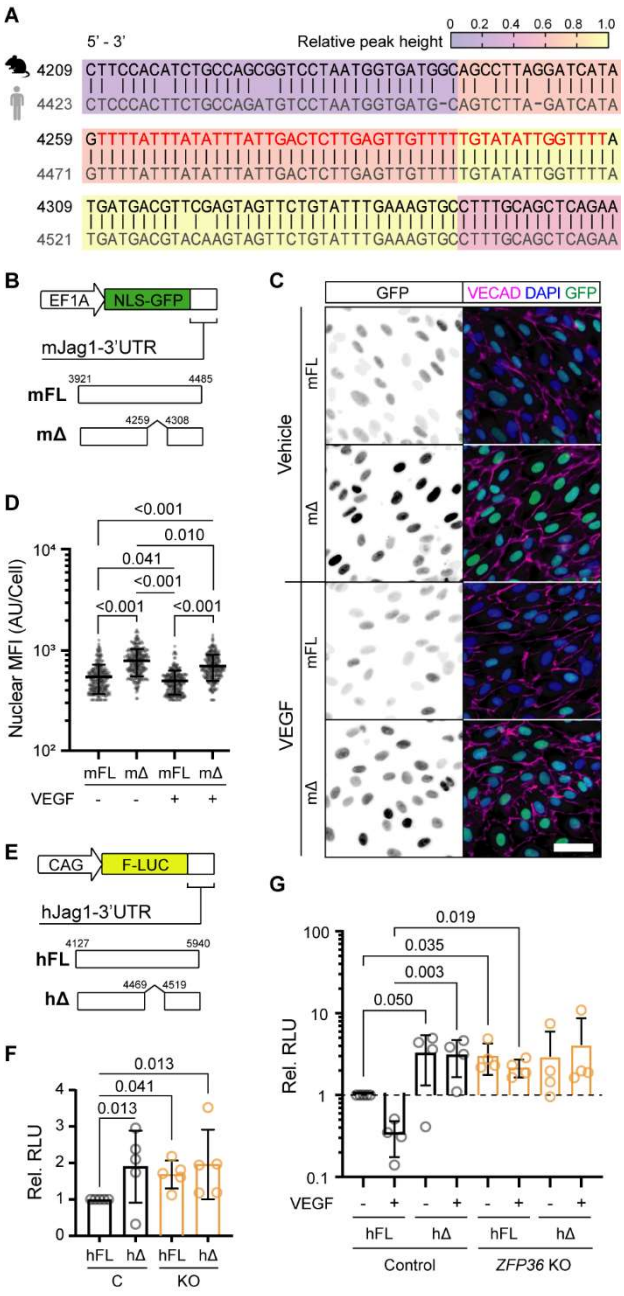

Figure 2.3 - Zfp36 regulates reporter expression levels depending on Jag1 3'UTR domains. **(A)** BLASTN sequence alignment (5' to 3') of mouse *Jag1* (NM_013882.5) and human *JAG1* (NM_000214.3) mRNA associated with peak ZFP36 binding domain identified in eCLIPseq experiments (red lettering). **(B)** Jag1 lentivirus reporter with NLS-eGFP m*Jag1* 3'UTR with and without peak binding sequence (4260-4307). **(C)** Representative immunofluorescence of VECAD and DAPI on Jag1-eGFP-UTR infected HUVECs stimulated with and without VEGF for 1 h (scale bar = 50 µm). **(D)** Quantification of GFP nuclear mean fluorescent intensity (MFI) per cell ± SD (n > 300 cells). Statistics: Kruskal-Wallis with post-hoc Dunn's multiple comparison test. **(E)**

Luciferase constructs fused to human *JAG1* 3'UTR with and without putative peak binding sequence (4470-4518). **(F)** Mean luciferase activity ± SD in CRISPR control and *ZFP36* KO HUVECs co-transfected with *JAG1* 3'UTR either full-length (FL) or without peak binding sequence (Δ) and *Renilla* luciferase. Data are normalized to *Renilla* luciferase and presented relative to control HUVECs transfected with FL (n=3 biological replicates with an additional technical replicate). Statistics: Kruskal-Wallis with post-hoc uncorrected Dunn's test. **(G)** Same as (F) but +/- VEGF treatment for 1h. Statistics: Kruskal-Wallis with post-hoc uncorrected Dunn's test.

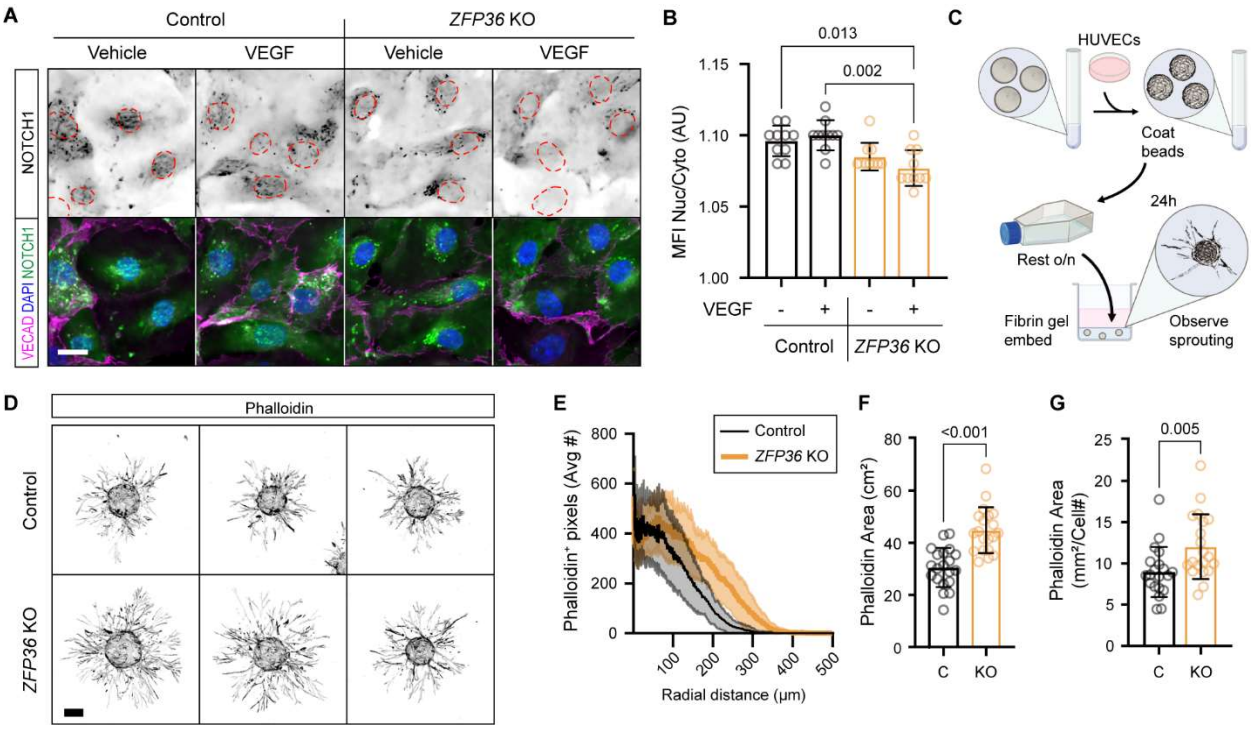

Figure 2.4 - Zfp36KO cells display increased sprouting angiogenesis.

(A) Representative immunofluorescence of NOTCH1, VECAD and DAPI in CRISPR-control and ZFP36 KO HUVECs +/- VEGF for 1 h (scale bar = 25 μm). Dashed outlines indicate individual nuclei. **(B)** Ratio of nuclear to cytosolic NOTCH1 MFI ± SD per field of view (n = 10 fields). Statistics: Kruskal-Wallis with post-hoc Dunn's multiple comparison test. **(C)** Schematic microcarrier bead angiogenesis assay. **(D)** Representative images of angiogenesis assay phalloidin staining results from CRISPR empty and ZFP36 KO HUVECs post 24 h (scale bar = 100 μm). **(E-G)** CRISPR-control and ZFP36 KO HUVEC microcarrier bead assay quantification of phalloidin distance relative to bead border **(E)**, overall phalloidin area (sans bead area) **(F)**, and overall phalloidin area normalized to cell number **(G)**. Data bars and error lines indicate mean ± SD (n = 20 technical replicates). Statistics: Mann-Whitney test.

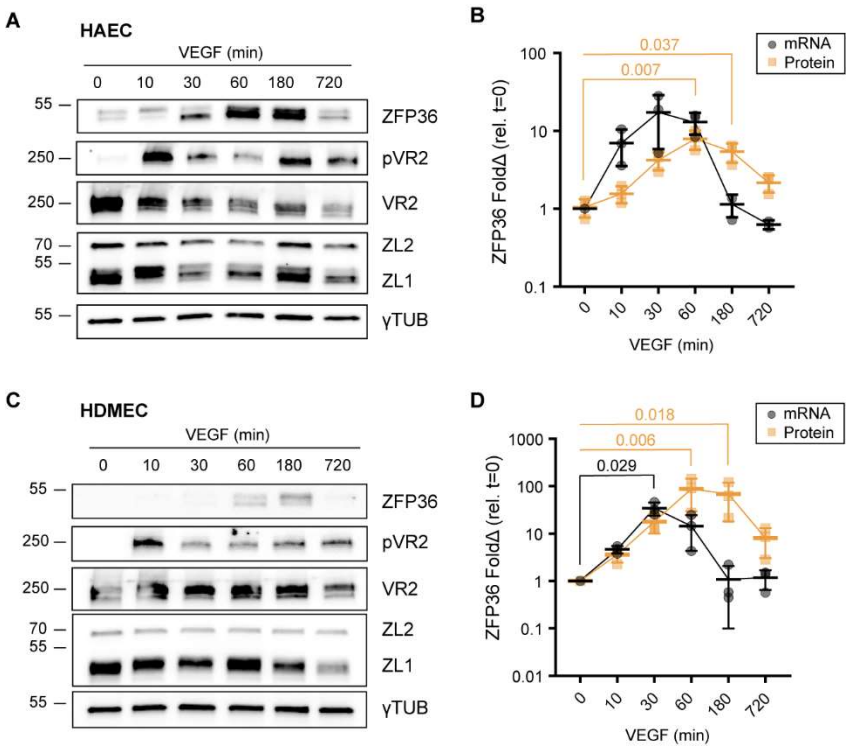

Supplemental Figure 2.1 - VEGF triggered induction of ZFP36 is conserved in multiple EC types.

(A) HAEC representative immunoblots of ZFP36, pVR2, VR2, ZFP36L1, ZFP36L2 and γTUB from VEGF stimulation time course experiment. Cultures were first incubated in serum-free medium overnight and stimulated with VEGF for the indicated times. **(B)** HAEC immunoblot quantification of fold change (Δ) of ZFP36 protein relative to control normalized to γTUB (n = 3 technical replicates) and qPCR of *ZFP36* transcripts of normalized to *HPRT* (n=3 technical replicates). Data for ZFP36 are individual replicates with line representing mean ± SD. Statistical analysis using Kruskal-Wallis with post-hoc Dunn's multiple comparison test. **(C)** HDMEC representative immunoblots of ZFP36, pVR2, VR2, ZFP36L1, ZFP36L2 and γTUB from VEGF stimulation time course experiment. Cultures were first incubated in serum-free medium overnight and stimulated with VEGF for the indicated times. **(D)** HDMEC immunoblot quantification of fold change (Δ) of ZFP36 protein relative to control normalized to γTUB (n = 3 technical replicates) and qPCR of *ZFP36* transcripts normalized to *HPRT* (n=3 technical replicates). Data for ZFP36 are individual replicates with line representing mean ± SD. Statistical analysis using Kruskal-Wallis with post-hoc Dunn's multiple comparison test. Abbreviations: Human aortic endothelial cell (HAEC), human dermal microvascular endothelial cell (HDMEC)

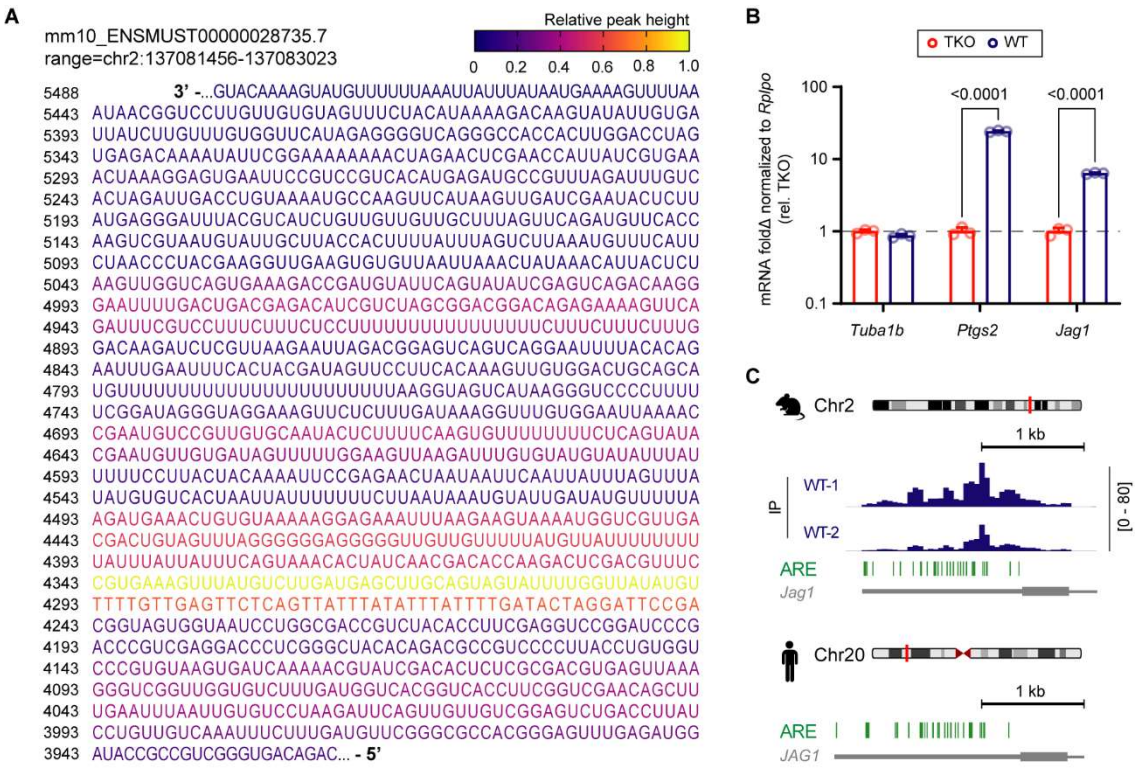

Supplemental Figure 2.2 - Jag1 mRNA features facilitate ZFP36 mRNA binding.

(A) Full mouse JAG1 3'UTR mRNA nucleotide sequence color coded based on relative eCLIP peak height. **(B)** Quantification of *Tuba1b*, *Ptgs2*, and *Jag1* mRNA fold change normalized to *Rplpo* from CLIP-qPCR experiment post 40 min serum stimulation of WT relative to TKO *Zfp36/l1/l2* triple-floxed MEF clones (n = 3 technical replicates). Statistical analysis was performed using two-way ANOVA with Sidak's multiple comparison test. **(C)** Integrative Genomics Viewer generated from AREsite2[28] identified adenosine-uridine rich element (ARE) motifs in mouse (mm10) and human (hg38) JAG1 3'UTR. Respective chromosome positions are marked with red lines. Mouse 3'UTR alignment also includes binding peaks from WT-IP eCLIP-seq experiment with respective track height scale denoted in brackets.

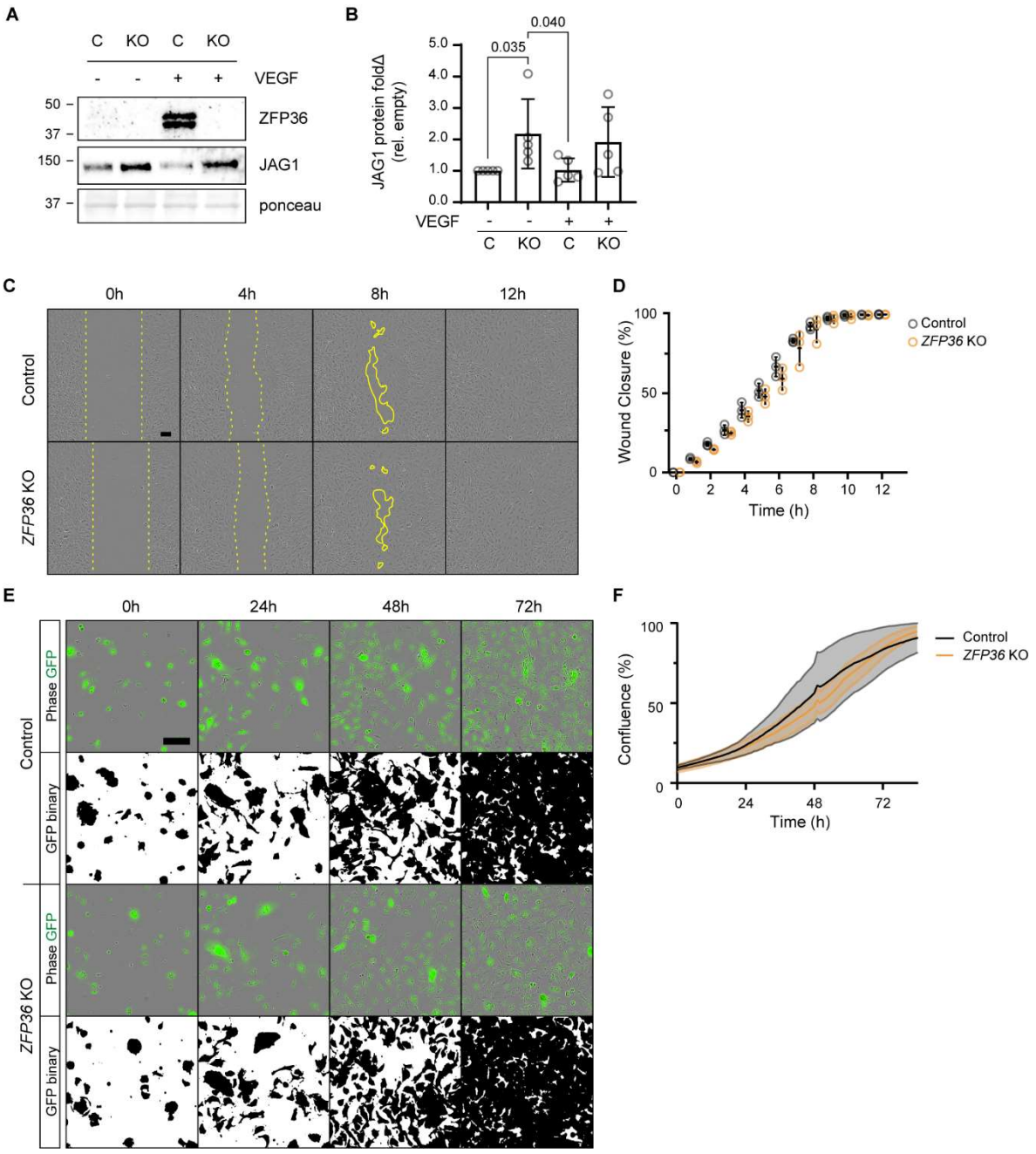

Supplemental Figure 2.3 - *In vitro* migration and proliferation are unaffected by *ZFP36* KO. **(A)** Representative immunoblots of ZFP36 and JAG1 protein expression from CRISPR control and *ZFP36* KO HUVECs stimulated with and without VEGF for 1 h. Ponceau is used as loading control reference. **(B)** Quantification of WB results fold change (Δ) in relative to empty control normalized to total protein (mean ± SD, n = 5 biological replicates). Statistical analysis using Kruskal-Wallis with post-hoc Dunn's multiple comparison test. **(C)** Representative phase images from scratch assay using CRISPR control and *ZFP36* KO HUVECs at indicated times. Empty culture area indicated with yellow outlines (scale bar = 100 µm). **(D)** Quantification of scratch

assay wound closure (%) area fraction (mean ± SD) measured at 1h increments (n = 3 biological replicates, each averaged from at least 4 technical replicates). **(E)** Representative overlay phase and fluorescence images from proliferation assay using CRISPR control and *ZFP36* KO HUVECs infected with CMV-GFP lentivirus. Binary GFP images were used for confluence quantification (scale bar = 100 μm). **(F)** Quantification of mean confluence overtime (%) calculated from GFP binary area fraction (mean line ± SD) measured at 1h increments (n = 2 biological replicates, 4 technical replicates each).

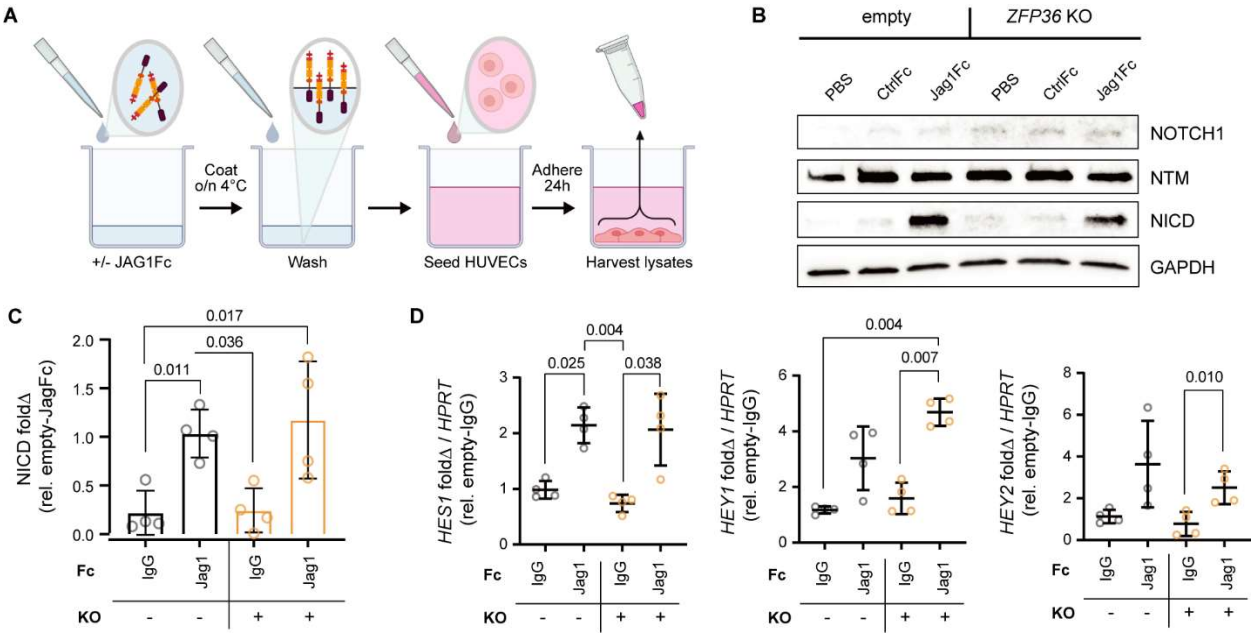

Supplemental Figure 2.4 - Trans-endothelial Notch activation is preserved in *ZFP36* KO cells when presented exogenous ligand.

(A) Schematic diagramming experimental design of JAG1Fc-coated plate assay. After coating human recombinant JAG1Fc overnight on tissue culture plate, HUVECs are seeded on top to confluence and allowed to adhere for 24 h before harvesting for Notch signaling analysis. **(B)** Representative immunoblots of full-length NOTCH1, NOTCH1 transmembrane fragment (NTM), cleaved NOTCH1 (NICD), and GAPDH from CRISPR empty or *zfp36*KO HUVECs post-24 h culture on JAG1-Fc coated plates. **(C)** Quantification of fold change (Δ) of ZFP36 protein relative to control normalized to housekeeping protein GAPDH or γTUB (n = 4 biological replicates). Statistical analysis using Kruskal-Wallis with post-hoc uncorrected Dunn's test. **(D)** Quantification of downstream NOTCH1 target genes *HES1, HEY1,* and *HEY2* mRNA mean fold change ± SD by qPCR from HUVEC JAG1-Fc experiments relative to CRISPR empty IgG cultured cells. Cq-values normalized to *HPRT* (n = 4 biological replicates). Statistical analysis performed using Kruskal-Wallis with post-hoc Dunn's multiple comparison test.

2.7 REFERENCES

1. McDonald, A.I., Shirali, A.S., Aragón, R., Ma, F., Hernandez, G., Vaughn, D.A., Mack, J.J., Lim, T.Y., Sunshine, H., Zhao, P., et al. (2018). Endothelial Regeneration of Large Vessels Is a Biphasic Process Driven by Local Cells with Distinct Proliferative Capacities. Cell Stem Cell 23, 210-225.e6. 10.1016/j.stem.2018.07.011.

2. Shirali, A.S., Romay, M.C., McDonald, A.I., Su, T., Steel, M.E., and Iruela-Arispe, M.L. (2018). A multi-step transcriptional cascade underlies vascular regeneration *in vivo*. Sci. Rep. 8, 5430. 10.1038/s41598-018-23653-3.

3. Cicchetto, A.C., Jacobson, E.C., Sunshine, H., Wilde, B.R., Krall, A.S., Jarrett, K.E., Sedgeman, L., Turner, M., Plath, K., Iruela-Arispe, M.L., et al. (2023). ZFP36-mediated mRNA decay regulates metabolism. Cell Rep. 42, 112411. 10.1016/j.celrep.2023.112411.

4. Makita, S., Takatori, H., and Nakajima, H. (2021). Post-Transcriptional Regulation of Immune Responses and Inflammatory Diseases by RNA-Binding ZFP36 Family Proteins. Front. Immunol. 12, 711633. 10.3389/fimmu.2021.711633.

5. Brooks, S.A., Connolly, J.E., and Rigby, W.F.C. (2004). The role of mRNA turnover in the regulation of tristetraprolin expression: evidence for an extracellular signal-regulated kinase-specific, AU-rich element-dependent, autoregulatory pathway. J. Immunol. 172, 7263–7271. 10.4049/jimmunol.172.12.7263.

6. Rezcallah, M.C., Al-Mazi, T., and Ammit, A.J. (2021). Cataloguing the phosphorylation sites of tristetraprolin (TTP): Functional implications for inflammatory diseases. Cell. Signal. 78, 109868. 10.1016/j.cellsig.2020.109868.

7. Whittles, C.E., Pocock, T.M., Wedge, S.R., Kendrew, J., Hennequin, L.F., Harper, S.J., and Bates, D.O. (2002). ZM323881, a novel inhibitor of vascular endothelial growth factor-receptor-2 tyrosine kinase activity. Microcirculation 9, 513–522. 10.1038/sj.mn.7800164.

8. Van Nostrand, E.L., Pratt, G.A., Shishkin, A.A., Gelboin-Burkhart, C., Fang, M.Y., Sundararaman, B., Blue, S.M., Nguyen, T.B., Surka, C., Elkins, K., et al. (2016). Robust transcriptome-wide discovery of RNA-binding protein binding sites with enhanced CLIP (eCLIP). Nat. Methods 13, 508–514. 10.1038/nmeth.3810.

9. Mukherjee, N., Jacobs, N.C., Hafner, M., Kennington, E.A., Nusbaum, J.D., Tuschl, T., Blackshear, P.J., and Ohler, U. (2014). Global target mRNA specification and regulation by the RNA-binding protein ZFP36. Genome Biol. 15, R12. 10.1186/gb-2014-15-1-r12.

10. Moore, M.J., Blachere, N.E., Fak, J.J., Park, C.Y., Sawicka, K., Parveen, S., Zucker-Scharff, I., Moltedo, B., Rudensky, A.Y., and Darnell, R.B. (2018). ZFP36 RNA-binding proteins restrain T cell activation and anti-viral immunity. eLife 7. 10.7554/eLife.33057.

11. Sedlyarov, V., Fallmann, J., Ebner, F., Huemer, J., Sneezum, L., Ivin, M., Kreiner, K., Tanzer, A., Vogl, C., Hofacker, I., et al. (2016). Tristetraprolin binding site atlas in the macrophage transcriptome reveals a switch for inflammation resolution. Mol. Syst. Biol. 12, 868. 10.15252/msb.20156628.

12. del Álamo, D., Rouault, H., and Schweisguth, F. (2011). Mechanism and significance of cis-inhibition in Notch signalling. Curr. Biol. 21, R40-7. 10.1016/j.cub.2010.10.034.

13. Taylor, G.A., Carballo, E., Lee, D.M., Lai, W.S., Thompson, M.J., Patel, D.D., Schenkman, D.I., Gilkeson, G.S., Broxmeyer, H.E., Haynes, B.F., et al. (1996). A Pathogenetic Role for TNFα in the Syndrome of Cachexia, Arthritis, and Autoimmunity Resulting from Tristetraprolin (TTP) Deficiency. Immunity 4, 445–454. 10.1016/S1074-7613(00)80411-2.

14. Lai, W.S., Kennington, E.A., and Blackshear, P.J. (2002). Interactions of CCCH zinc finger proteins with mRNA: non-binding tristetraprolin mutants exert an inhibitory effect on degradation of AU-rich element-containing mRNAs. J. Biol. Chem. 277, 9606–9613. 10.1074/jbc.M110395200.

15. Lykke-Andersen, J., and Wagner, E. (2005). Recruitment and activation of mRNA decay enzymes by two ARE-mediated decay activation domains in the proteins TTP and BRF-1. Genes Dev. 19, 351–361. 10.1101/gad.1282305.

16. Fabian, M.R., Frank, F., Rouya, C., Siddiqui, N., Lai, W.S., Karetnikov, A., Blackshear, P.J., Nagar, B., and Sonenberg, N. (2013). Structural basis for the recruitment of the human CCR4-NOT deadenylase complex by tristetraprolin. Nat. Struct. Mol. Biol. 20, 735–739. 10.1038/nsmb.2572.

17. Newton, R., Shah, S., Altonsy, M.O., and Gerber, A.N. (2017). Glucocorticoid and cytokine crosstalk: Feedback, feedforward, and co-regulatory interactions determine repression or resistance. J. Biol. Chem. 292, 7163–7172. 10.1074/jbc.R117.777318.

18. Rappl, P., Brüne, B., and Schmid, T. (2021). Role of tristetraprolin in the resolution of inflammation. Biology (Basel) 10. 10.3390/biology10010066.

19. Al-Souhibani, N., Al-Ahmadi, W., Hesketh, J.E., Blackshear, P.J., and Khabar, K.S.A. (2010). The RNA-binding zinc-finger protein tristetraprolin regulates AU-rich mRNAs involved in breast cancer-related processes. Oncogene 29, 4205–4215. 10.1038/onc.2010.168.

20. Tiedje, C., Diaz-Muñoz, M.D., Trulley, P., Ahlfors, H., Laaß, K., Blackshear, P.J., Turner, M., and Gaestel, M. (2016). The RNA-binding protein TTP is a global post-transcriptional regulator of feedback control in inflammation. Nucleic Acids Res. 44, 7418–7440. 10.1093/nar/gkw474.

21. Suarez-Arnedo, A., Torres Figueroa, F., Clavijo, C., Arbeláez, P., Cruz, J.C., and Muñoz-Camargo, C. (2020). An image J plugin for the high throughput image analysis of *in vitro* scratch wound healing assays. PLoS ONE 15, e0232565. 10.1371/journal.pone.0232565.

22. Anders, S., and Huber, W. (2010). Differential expression analysis for sequence count data. Genome Biol. 11, R106. 10.1186/gb-2010-11-10-r106.

23. Love, M.I., Huber, W., and Anders, S. (2014). Moderated estimation of fold change and dispersion for RNA-seq data with DESeq2. Genome Biol. 15, 550. 10.1186/s13059-014-0550-8.

24. Smith, T., Heger, A., and Sudbery, I. (2017). UMI-tools: modeling sequencing errors in Unique Molecular Identifiers to improve quantification accuracy. Genome Res. 27, 491–499. 10.1101/gr.209601.116.

25. Martin, M. (2011). Cutadapt removes adapter sequences from high-throughput sequencing reads. EMBnet j. 17, 10. 10.14806/ej.17.1.200.

26. Dobin, A., Davis, C.A., Schlesinger, F., Drenkow, J., Zaleski, C., Jha, S., Batut, P., Chaisson, M., and Gingeras, T.R. (2013). STAR: ultrafast universal RNA-seq aligner. Bioinformatics 29, 15–21. 10.1093/bioinformatics/bts635.

27. Krakau, S., Richard, H., and Marsico, A. (2017). PureCLIP: capturing target-specific protein-RNA interaction footprints from single-nucleotide CLIP-seq data. Genome Biol. 18, 240. 10.1186/s13059-017-1364-2.

28. Gruber, A.R., Fallmann, J., Kratochvill, F., Kovarik, P., and Hofacker, I.L. (2011). AREsite: a database for the comprehensive investigation of AU-rich elements. Nucleic Acids Res. 39, D66-9. 10.1093/nar/gkq990.

29. Martindale, J.L., Gorospe, M., and Idda, M.L. (2020). Ribonucleoprotein immunoprecipitation (RIP) analysis. Bio Protoc 10, e3488. 10.21769/BioProtoc.3488.

30. Kempers, L., van der Bijl, I., van Stalborch, A.-M.D., Ponsioen, B., and Margadant, C. (2021). Fast *in vitro* protocol for the visualization and quantitative high-throughput analysis of sprouting angiogenesis by confocal microscopy. STAR Protocols 2, 100690. 10.1016/j.xpro.2021.100690.

31. Sanjana, N.E., Shalem, O., and Zhang, F. (2014). Improved vectors and genome-wide libraries for CRISPR screening. Nat. Methods 11, 783–784. 10.1038/nmeth.3047.

32. Mack, J.J., Mosqueiro, T.S., Archer, B.J., Jones, W.M., Sunshine, H., Faas, G.C., Briot, A., Aragón, R.L., Su, T., Romay, M.C., et al. (2017). NOTCH1 is a mechanosensor in adult arteries. Nat. Commun. 8, 1620. 10.1038/s41467-017-01741-8.

33. Matsuda, T., and Cepko, C.L. (2004). Electroporation and RNA interference in the rodent retina *in vivo* and *in vitro*. Proc Natl Acad Sci USA 101, 16–22. 10.1073/pnas.2235688100.

34. Schindelin, J., Arganda-Carreras, I., Frise, E., Kaynig, V., Longair, M., Pietzsch, T., Preibisch, S., Rueden, C., Saalfeld, S., Schmid, B., et al. (2012). Fiji: an open-source platform for biological-image analysis. Nat. Methods 9, 676–682. 10.1038/nmeth.2019.

35. Suarez-Arnedo, A., Torres Figueroa, F., Clavijo, C., Arbeláez, P., Cruz, J.C., and Muñoz-Camargo, C. (2020). An image J plugin for the high throughput image analysis of *in vitro* scratch wound healing assays. PLoS ONE 15, e0232565. 10.1371/journal.pone.0232565.

CHAPTER 3

3.1 INTRODUCTION

This chapter presents *in vivo* findings from a manuscript accepted in Cell Reports (Sunshine et al. 2023, in press). The aim of the study is to examine the functional role for ZFP36 in endothelial biology. All experiments have therefore been completed and are awaiting final review. We established previously *in vitro* in both mouse and human primary cells that ZFP36 mediates JAG1 expression. We further provide evidence that 3'UTR binding identified in mouse embryonic fibroblast CLIP data is conserved in human cells using fluorescence and luminescence decay assays showing that when peak binding domains are deleted signal intensity is retained compared to full length UTR. Furthermore, we show *in vitro* that the increase in JAG1 caused by *ZFP36* KO in HUVECs resulted in reduced Notch signaling and increased the density of tip cells in microbead angiogenesis. Based on these findings we were interested in confirming increased EC JAG1 in endothelial specific *Zfp36* KO animals and whether this increase consequently changes sprouting dynamics *in vivo*.

3.2 RESULTS

3.2.1 Inactivation of ZFP36 in ECs alters the distribution and levels of Jag1.

Animal models with global deletion in *Zfp36* develop inflammatory phenotypes. In fact, many identified mRNA binding targets are involved in regulating inflammatory transcripts, particularly TNFα in macrophages.[1] To clarify the role of ZFP36 in the endothelium and under physiological conditions, we generated tamoxifen-inducible EC-specific KO mice. Induction of endothelial *Zfp36* deletion with tamoxifen shortly post-birth did not result in drastic alterations in the phenotype of the mice, nor revealed any inflammatory phenotypes despite high induction efficiency (data not shown). To test the consequence of *Zfp36* deletion to Jag1 levels, we first isolated liver ECs from Cre-negative and Cre-positive *Zfp36*$^{f/f}$ that were exposed to tamoxifen shortly post-birth (Figure 3.1A). The efficiency of the isolation and relative endothelial purity of the cultures was assessed

by evaluation of tdTomato (Tom) reporter by fluorescence microscopy and flow cytometry (Figure 3.1B, 3.1C). Using these cells, we evaluated levels of Jag1 by flow cytometry and Western blots (Figure 3.1D, 3.1E). In both cases, absence of Zfp36 yielded a significant increase in both cell surface and total Jag1 protein. We also verified levels of Jag1 protein *in vivo*. As aortic ECs from adult mice normally express *Jag1*, we predicted that this expression would be elevated in the absence of endothelial *Zfp36*. Accordingly, immunocytochemistry of adult animals that were pulsed with tamoxifen for three consecutive days post-birth, then evaluated at P120, showed that reporter positive cells (Tom, arrowheads) had higher levels of JAG1 than adjacent cells that were not deleted for *Zfp36* (as per lack of Tom, arrows) (Figure 3.1F-H). Similar experiments were also performed in triple (*Zfp36*, *Zfp36l1* and *Zfp36l2*) – endothelial specific deleted animals (Z36T), which yielded the same outcome (Figure 3.1G, 3.1I). Specifically, reporter-positive ECs (Tom-positive, arrowheads) showed a higher level of JAG1 than adjacent reporter-negative ECs (Tom-negative; arrows). These results were slightly more robust than single *Zfp36* deletion in adults (Figure 3.1G, 3.1I), suggesting a potential overlapping effect by ZFP36L1 and ZFP36L2 family members.

3.2.2 ZFP36 affects sprouting angiogenesis *in vivo* by altering Jag1 expression.

The mouse retina is a classical site in which to visualize vascular morphogenesis in a planar manner. By P6, the angiogenic front can be noted at the edge with progressive differentiation towards the center of the retina.[2] First, we sought to determine whether Zfp36 was expressed in the retinal endothelium at the relevant timepoints. For this, we took advantage of available scRNAseq datasets published by two independent groups.[3,4] Critically, these results indicated that transcripts for Zfp36 (and Jag1) were present in developing retina ECs (Figure 3.2A-D). This information was imperative, as none of the commercially available antibodies tested were able to faithfully recognize mouse Zfp36 by immunocytochemistry (using null mice as controls) in our hands. Distribution of Zfp36 and Jag1 expressing cells in the UMAP in relation to the

subpopulations of endothelial cells in the retina (Figure 3.2B, 3.2C, red dots for Zfp36 and green dots for Jag1) revealed absence of overlap between the transcripts (yellow dots), supporting the concept that Zfp36 decreases levels of Jag1 transcripts. Importantly, examining specific cluster expression levels clearly demonstrated that Zfp36 is higher in tip cells, the region of greatest exposure to VEGF and where Jag1 is canonically low (Figure 3.2D). As anticipated, Dll4 is also highest in the tip cell population, while Jagged is highest in the stalk cell population. In contrast, the Notch1 receptor levels are very low and generally distributed evenly across all clusters. This would suggest that relative abundance of ligands Dll4 and/or Jag1 drives positive signaling or cis inhibition.

Next, we evaluated distribution and levels of Jag1 in the retinal vasculature of $Zfp36^{f/f}$ Cdh5-Cre negative and Cre positive mice. As anticipated, endothelial deletion of Zfp36 yields higher levels of overall Jag1 within CD31 positive vasculature (Figure 3.3A-C). The overall measured increase Jag1 was equivalent at the angiogenic front and in the inner primary plexus (Figure 3.3D). We acknowledge, however, that our current methods do not account for the potential contribution of Jag1 expression from other cell types. The inner plexus, for instance, includes pericytes and smooth muscle cells which also express Jag1. When we performed IHC analysis on a known Zfp36 target and tip cell marker uPAR,[5] we observed significant upregulation primarily at the angiogenic front (Figure S3.1A, S3.1B). The angiogenic front is unique in that it is generally only composed of sprouting tip endothelial cells, which express high levels of Zfp36 based on single cell analysis. Therefore, we expect that the cells responsible for protein increases in this area are endothelial. Higher levels of uPAR and Jag1 were even more pronounced when all three ZFP36 family members were inactivated in the endothelium (Figure S3.1C, S3.1D, 3.3E, 3.3F). Jag1 expression was increased by nearly three-fold in both the angiogenic front and in the inner plexus (Figure 3.3E, 3.3F). Combined, these findings validate that Jag1 is indeed an important target of *Zfp36 in vivo* and further highlight that expression of Zfp36 in the tip cells prevents expression of Jag1 at the angiogenic front.

We then explored whether the balance of tip to stalk cell identity was compromised when *Zfp36* was deleted from the endothelium. Using mice with endothelial-specific deletion of *Zfp36* and Cre-negative controls, we found that outgrowth was impaired and the number of $ESM1^{+}ERG^{+}$ cells (tip cells) was increased in $Zfp36^{ECKO}$ retinas in comparison to littermate controls (Figure 3.4A-D). Once again, these effects were more pronounced in triple KO animals when all three Zfp36 family members were deleted in the endothelium (Figure S3.1E-H). Although in this model, attributing the delayed outgrowth solely to changes in tip and stalk cell dynamics is potentially confounded by the additional reduction in proliferation at the angiogenic front (Figure S3.1I, S3.1J). These changes in proliferation are not observed in the single Zfp36 endothelial null mice (Figure S3.1K, S3.1L).

Overall, our findings *in vivo* were consistent with a role for ZFP36 in the regulation of Notch signaling by altering JAG1 levels and distribution. Then again, ZFP36 controls multiple other genes, including uPAR, which could likely participate in promoting the invading angiogenic front. Thus, additional experimentation was needed to inquire about to what level was the effect of Zfp36 specifically on Jagged1, associated with the biological outcomes observed. Along these lines, we considered a potential rescue experiment whereby genetic reduction in Jag1, in the context of Zfp36 deficiency, might return baseline levels of Jag1 and normalize biological read outs. These experiments could help us confirm or deny direct causation. To achieve this, we first examined how removal of one Jag1 allele affected protein levels and vascular growth. Endothelial-specific heterozygous mice for Jag1 showed a reduction in Jag1 protein by about 20% in comparison to control (Figure 3.4E-H) and delayed angiogenic outgrowth (Figure 3.4I, 3.4J). Crosses between Cdh5-Cre $Zfp36^{f/f}$ animals and $Jag1^{f/f}$ eventually allowed us to obtain triple transgenic mice with either one or two copies of *Jag1* in the same litter. Lower levels of Jag1 protein were detected in Jag1 $^{f/+}$ / $Zfp36^{f/f}$ / Cre+ mice in arteries, veins, capillaries and in the angiogenic front. In this context inactivation of Zfp36 resulted in an elevation in Jag1 protein, albeit not sufficiently high to return to baseline (wild-type) levels (Figure 3.4K-O). Despite this the additional Jag1 protein was

sufficient to rescue the biological phenotype of Zfp36^{ECKO}. Specifically, both the increase in tip cells and the reduction in angiogenic outgrowth were returned to base line levels by Jag1 haploinsufficiency (Figure 3.4P-S). Combined these experiments corroborated that regulation of Jag1 by Zfp36 is biologically relevant. Moreover, as a supplemental merit, both compared experimental groups in Jag1 haploinsufficiency experiments were Cre-positive and exposed to tamoxifen, providing an important control for concurrent presence of Cre and tamoxifen.[6]

3.3 DISCUSSION

In mice, we show that endothelial-specific deletion of ZFP36 mirrored the effects found *in vitro* with increased levels of JAG1 and increased number of ESM1-expressing tip cells in the immature vascular plexus that delays maturation and growth. This phenotype was mitigated by genetic reduction of Jag1 dosage through heterozygous expression. Based on these data we predict ZFP36 participates in a biologically conserved VEGF sensitive feedforward mechanism to direct Notch signaling through rapid post-transcriptional destabilization of *Jag1*-mRNA.

The identification of this regulatory mechanism for *Jag1* is far-reaching given the impact of the Notch signaling pathway in multiple biological and pathological settings. Within the context of a growing vascular plexus, these results fill a knowledge gap and explain the heterogenous distribution of JAG1 in the developing vascular plexus (abundant in mature arteries but absent from the sprouting front).[7] JAG1 is predominantly, though nonexclusively, expressed in adult arterial endothelium.[8] In mature vessels, JAG1 mediates trans-Notch activation, but mostly through heterotypic interactions with smooth muscle cells.[9-11] Maturation of the vascular plexus requires acquisition of mural cells (pericytes and smooth muscle cells). It is in this context that high *Jag1* expression is important. Endothelial JAG1 trans-activates Notch1 and 3 in smooth muscle cells, promoting mural cell investment and arterial fate.

Specific ligand enrichment is not unique to the mature vascular plexus, DLL4 is the predominant ligand for Notch in capillaries and in sprouting tip cells. In this manner, while JAG1

marks mature arterioles, DLL4 is a well-accepted marker for tip cells along with ESM1.[12] At the angiogenic front, the expansion of a vascular plexus relies on the careful specification of tip and stalk cells. Tip cells at the edge of the plexus expand the network, while the adjacent stalk cells communicate to the rest of the network through the organization of tubular structures. VEGF and Notch coordinate this process, whereby VEGF drives *Dll4* expression in tip cells that bind to adjacent Notch-expressing stalk cells, establishing their differential fates.[13-15] Additionally, Dll4 is maintained through a Notch-dependent positive feedback loop.[16] This relationship provides a feedforward mechanism by which Notch signaling can be propagated between adjacent ECs with very limited amount of ligand. In fact, this inter-endothelial continuous DLL4/Notch signaling is critical for endothelial quiescence and vascular stability.[17-20] Thus, DLL4 is distributed throughout the plexus regulating multiple aspects necessary for establishing and maintaining vascular networks. In addition to intrinsic Notch autoregulatory mechanisms, interactions with transcription factors, such as ERG, have been noted to reinforce *Dll4* activation and repress *Jag1*.[21] This mechanism, however, presents a paradox in that ERG expression is relatively uniform across the vascular plexus despite varying ligand expression. Therefore, the confined endothelial distribution of JAG1 has been acknowledged, but not mechanistically understood.[22] Critically, *Dll4* transcripts have very few weak ARE-motifs only noted to interact with ZFP36L1[23] which we found not to be induced by VEGF. Thus, our results depict a targeted auxiliary model for *Jag1* suppression by ZFP36 that spatially matches its known expression and interaction profiles, hence satisfying a potential mechanism for ligand segregation.

The combinatorial contribution of Notch ligands in the endothelium remains poorly understood. Notably, EC-specific inactivation of each ligand yields distinct phenotypes, highlighting nonredundant ligand contributions to vascular morphogenesis. Deletion of *Dll4* leads to excess of sprouts and absence of a differentiated vascular network, a phenotype that is replicated by inactivation of *Notch1* in ECs.[24-26] In contrast, EC-specific deletion of *Jag1* yields a considerably reduced vascular plexus with a paucity of tip cells.[27] These findings support the

necessary interplay between ligands and a model where JAG1 functions antagonistically to canonical *trans*-EC DLL4 ligand binding, titrating signaling potential. In this context, we propose that ZFP36 acts as a rheostat for this balance by imposing pulses of transient Jag1 suppression that provide feedforward regulation and adequate vascular morphogenesis.

3.4 – AUTHOR CONTRIBUTIONS

Conceptualization, HLS and MLIA; Methodology, HLS, DP, and VS; Validation, HLS; Formal Analysis, HLS, FM, CS, and VS; Investigation HLS; Resources FM, VS, MT and TAV; Writing – Original Draft, HLS and MLIA; Writing – Review & Editing HLS, ACC, HRC, TAV, and MLIA; Funding Acquisition, HLS and MLIA; Supervision, HRC, TAV, and MLIA.

3.5 – METHODS

3.5.1 Resource availability

Materials used in this study are commercially available. This study analyzes existing, publicly available data. Accession numbers and detailed material information can be found in the key resources table below.

3.5.2 Experimental models

All animal procedures were approved and performed in accordance with Northwestern University Institutional Animal Care and Use Committee. All mouse strains were maintained on a C57BL/6J background, both female and male mice were used for retina analysis. For inducible endothelial deletion of *Zfp36*, Tg(*Cdh5*-Cre/ERT2)1Rha mice[28] were crossed with *Zfp36*$^{f/f}$ mice or with *Zfp36*$^{f/f}$*l1*$^{f/f}$*l2*$^{f/f}$ mice.[29,30] These lines were then further crossed with R26RTd Cre reporter line (Gt(ROSA)26Sor $^{tm14(CAG\ tdTomato)Hze}$).[31] For developmental post-natal comparisons, internal littermate controls were achieved by crossing Cre(-) with Cre(+) parents. For *Jag1* dosage experiments, mice Cdh5-Cre(+) and *Zfp36*$^{f/f}$ were further crossed with *Jag1*$^{f/f}$ mice[32] and backcrossed in order to obtain Cdh5-Cre(+) litters containing *Zfp36*$^{f/f}$*Jag1*^{wt} and *Zfp36*$^{f/f}$*Jag1*$^{f/+}$ for

comparison. Three consecutive days of tamoxifen administration was given by oral gavage (5uL at 20mg/mL) starting on day of birth.

2.5.3 Method details

Liver endothelial isolation and flow cytometry

Aged tamoxifen-treated Cre(-) *Zfp36*$^{f/f}$ and Cre(+) *Zfp36*$^{f/f}$ Tom reporter mice were sacrificed and perfused through the left ventricle with 10mL DMEM. Liver lobes were collected and washed once with HBSS and returned to fresh DMEM. Tissue was roughly minced with surgical scissors. Liver pieces were then digested using liver dissociation kit (Miltenyi) according to manufacturer's instructions. Cell pellets were resuspended in 1 mL RBC lysis buffer and incubated for 4 min at RT with frequent vortexing. This reaction was quenched using 12 mL HBSS + 10% FBS. Cells were pelleted at 300xg for 10 min. If the pellet was still red, RBC lysis was repeated however all subsequent incubations were only 1 min without vortexing. When the pellet was clean, it was resuspended in DMEM and cells counted with trypan blue. Cells were then plated at a concentration of $1.5x10^6$ cells/well of 6-well plate. Cells were then placed in humidified incubator at 37°C with 5% CO_2 for 1 h in MCDB-131+10% FBS to for adherent endothelial enrichment. After washing away non-adherent cells, adherent cells were trypsinized and collected, pelleted, and stained in FACS buffer (0.5% bovine serum albumin, 1 mM EDTA and 0.05% sodium azide in PBS) with indicated antibodies for 30 min on ice. When secondaries were necessary, cells were washed twice with FACs buffer before incubating with secondary for 30 min on ice. For direct flow analysis, cells were washed and then fixed with 1% PFA before analysis using Cytek® Northern Lights™ flow cytometer. Data were analyzed with FlowJo (BD Biosciences).

Aorta en face preparation

Mice were intraperitoneally injected with 100 µL methalcholine (10 mg/mL in 1xPBS) before sacrifice. 2% (wt/vol) PFA was perfused through the left ventricle of the heart; the aorta's length was then measured before removal. Under a dissecting microscope, small branching vessels and

adventitia were removed before the vessel was cut open longitudinally. Fileted tissue pieces were then pinned down in a 35 mm silicon-coated dish before proceeding with additional 2% (wt/vol) PFA fixation for 20 min at room temperature.

Aorta en face immunohistochemistry

Pinned aortae in silicon-coated dishes were washed 3x5 min with Hank's balanced salt solution (HBSS) before incubating in blocking/permeabilization buffer (0.3% TritonX-100, 0.05% Tween-20, 3% Normal Donkey Serum in HBSS) for 1 h at room temperature. Aortae were incubated in primary antibody overnight at 4°C, washed 3x5 min with 1xHBSS, and then incubated in secondary antibody for 1 h at room temperature. To mount, aortae were stretched and pinned to its *in-situ* length on a silicon-coated dish. A glass coverslip was then placed under the pinned aorta, ProLong Gold mounting reagent was used to cover the tissue, and then a second glass coverslip was placed over the tissue to seal. After curing overnight at room temperature, the glass-tissue-glass sandwich was transferred onto a glass microscope slide and imaged.

Retina immunohistochemistry

At P6, post-enucleation, whole eyes were fixed directly in 4% PFA for 15min, followed by retinal dissection in 2% PFA and total fixation time of 1 h in 2% PFA. The retinas were washed 3x5 min in 1xPBS before blocking for 1 h at room temperature. Primary antibodies were incubated overnight at 4 °C in blocking buffer. The following day retinas were washed 3x5 min in 1xPBS before secondary antibodies applied for 1 h at room temperature. Retinas were again washed 3x5 min in 1xPBS and flat-mounted on slides in ProLong Gold Antifade Mountant (Fisher Scientific #P36930).

IHC confocal imaging

Imaging was performed using A1R HD25 confocal microscope (Nikon). Z-stack and tile scan features were used to image the entire retinal surface and superficial plexus. Tiles were stitched

into a single large image (NIS-Elements, Nikon). For figure images, Denoise.AI (Nikon) was employed to remove Poisson shot noise. Images were acquired using ×20 objective.

Image Quantification and Analysis

Aorta single field Z-stacks (non-denoised) were analyzed in ImageJ for JAG1 mean fluorescent intensity for each field of view. Manual selections were made in some instances in Cre(+) animals to only include Tom(+) cells. For outgrowth calculations, Denoise.ai (Nikon) processed retina images were analyzed with ImageJ (FIJI). Imported images were threshold to create binary images for total area and CD31 area. A median of 0.5 pixels was applied to remove noise. Convex hulls were generated from CD31 area and used to calculate percent outgrowth from total area. Percent outgrowth was then normalized relative to littermate controls. Using CD31 (BD) binary images created as described above, selection masks were generated to measure vasculature specific mean fluorescent intensity (MFI) of uPAR (R&D Systems) or JAG1 (Sigma) on corresponding un-denoised images. For vascular plexus subdivision, previously generated CD31 convex hulls were rescaled centered to 70%. This new scaled selection was used to divide CD31 binary into inner plexus and angiogenic front specific surfaces. Mean fluorescent intensity measurements were normalized by subtracting mean background fluorescent intensity and made relative to littermate controls. Counting ESM1+ and pHH3+ ECs was performed manually using Imaris spots feature. Positive counts were made for ERG that co-localized with the respective marker. Counts outside CD31+ area were excluded.

scRNA-seq processing and analysis

The expression matrices for the scRNA-seq samples were downloaded from GEO accession: GSE175895. All six samples were merged, and only the WT samples were used to make the plots. The R package Seurat[33] (v4.1.1) was used to cluster the cells in the merged matrix. Cells with less than 100 genes or 500 transcripts or more than 10,000 transcripts or 15% of mitochondrial expression were first filtered out as low-quality cells. The NormalizeData function

was used to normalize the expression level for each cell with default parameters. The FindVariableFeatures function was used to select variable genes with default parameters. The ScaleData function was used to scale and center the counts in the dataset. Principal component analysis (PCA) was performed on the variable genes. The RunHarmony function from the Harmony package was applied to remove potential batch effect among samples processed in different batches. Uniform Manifold Approximation and Projection (UMAP) dimensional reduction was performed using the RunUMAP function. The clusters were obtained using the FindNeighbors and FindClusters functions with the resolution set to 0.5. The cluster marker genes were found using the FindAllMarkers function. Pecam1 and Cdh5 expressions were used to identify the endothelial cluster. Sub-clustering on ECs was performed with the same quality controls and Seurat steps described above. Heatmaps, violin plots and gene expression plots were generated by DoHeatmap, VlnPlot and featurePlot functions, respectively.

Quantification and statistical analysis

Statistical parameters were calculated using Prism 8 (GraphPad) and are specified in figure legends. Unless otherwise stated, we calculated p-values for time course datasets using non-parametric Kruskal-Wallis with post-hoc Dunn's multiple comparison test. For single comparisons we used Mann-Whitney tests. All significant results, defined as having a p-value < 0.05, are specified for each figure.

Table 3.1 – Key resource table

REAGENT or RESOURCE	SOURCE	IDENTIFIER
Antibodies		
Rat monoclonal anti- CD11b, PerCP-Cy™5.5 conjugated	Biolegend	Cat#101228; RRID: AB_893232
Rat monoclonal anti-CD31	BD Biosciences	Cat#557355; RRID: AB_396660
Rat monoclonal anti-CD31, FITC conjugated, Clone MEC 13.3	BD Biosciences	Cat#553372; RRID: AB_394818
Hamster monoclonal anti-CD31 (clone 2H8)	Bogen et al.[34]	N/A

Rat monoclonal anti-CD45, Brilliant Violet 421TM conjugated	Biolegend	Cat#109831; RRID: AB_10900256
Rabbit monoclonal anti-CDH5	Cell Signaling Tech	Cat#2500; RRID: AB_10839118
Rabbit monoclonal anti-ERG	Abcam	Cat#Ab115555; RRID: AB_10898854
Rabbit monoclonal anti-ERG- Alexa Fluor® 647	Abcam	Cat#Ab196149
Rabbit monoclonal anti-ERG- Alexa Fluor® 488	Abcam	Cat#Ab196374
Goat polyclonal anti-ESM1	R&D Systems	Cat#AF1999; RRID: AB_2101810
Rabbit polyclonal anti-phospho-Histone H3 (Ser10)	Cell Signaling Tech	Cat#9701; RRID: AB_331535
Rabbit monoclonal anti-JAG1	Cell Signaling Tech	Cat#2620; RRID: AB_10693295
Goat polyclonal anti-JAG1	Sigma-Aldrich	Cat#J4127; RRID: AB_260348
Goat polyclonal anti-uPAR	R&D Systems	Cat#AF534; RRID: AB_2165351
Rabbit monoclonal anti-VR2	Cell Signaling Tech	Cat#2479; RRID: AB_2212507
Rabbit monoclonal anti-ZFP36	Cell Signaling Tech	Cat#71632; RRID: AB_2799806
Rabbit polyclonal anti-ZFP36	Millipore Sigma	Cat#ABE285; RRID: AB_11205589
Chemicals, peptides, and recombinant proteins		
eBioscienceTM 1xRBC lysis buffer	Invitrogen	Cat#00-4333-57
Methalcholine chloride, 100.4%	MP Biomedicals	Cat#0219023105
Restore™ Western Blot Stripping Buffer	Thermo Fisher	Cat#21059
ProLong Gold Antifade Mountant	Thermo Fisher	Cat#P36930
cOmplete™ EDTA-free Protease Inhibitor Cocktail	Sigma-Aldrich	Cat#11873580001
2.5% Trypsin, 10x	Corning	Cat#MT25054CI
Paraformaldehyde (PFA) 4%, in PBS	Thermo Fisher	Cat#AAJ61899AP
Triton-X100	Thermo Fisher	Cat#BP151500
Tween-20	Sigma-Aldrich	Cat#P9416
Normal Donkey Serum	Jackson ImmunoResearch	Cat#017-000-121
Critical commercial assays		
Trans-Blot® Turbo™ RTA Midi Nitrocellulose Transfer Kit	Bio-Rad	Cat#1704271
Thermo Scientific Pierce Detergent Compatible Bradford Assay	Fisher Scientific	Cat#PI23246
4–20% Mini-PROTEAN® TGX™ Precast Protein Gels	Bio-Rad	Cat#4561095, 4561094
4–20% Criterion™ TGX Stain-Free™ Protein Gel	Bio-Rad	Cat#5678093
Liver dissociation kit, mouse	Miltenyi	Cat#130-105-807

Deposited data		
Retinal single-cell mRNA profiles of WT P6 mice (GSM5350878)	Zarkada et al.[3]	GSE175895
Experimental models: Organisms/strains		
Mouse: Tg(Cdh5-cre/ERT2)1Rha	Sörensen et al.[35]	N/A
Mouse: Zfp36f/f	Qiu et al.[30]	N/A
Mouse: Gt(ROSA)26Sor tm14(CAG tdTomato)Hze	Jackson Laboratory	RRID: IMSR_JAX:007914
Mouse: Jag1f/f	Mancini et al.[36]	N/A
Mouse: Zfp36f/fZl1f/fZl2f/f	This paper	N/A
Software and algorithms		
FIJI	Schindelin et al.[37]	RRID:SCR_002285
Imaris (v9.9.0)	Bitplane	RRID:SCR_007370
Seurat (v4.1.1)	Hao et al.[38]	RRID:SCR_016341
NIS Elements	Nikon	RRID:SCR_014329
Image Lab Software	BioRad	RRID:SCR_014210
STAR (v2.7.3)	Dobin et al.[39]	RRID:SCR_004463
FlowJo	BD Biosciences	RRID:SCR_008520
BioRender	BioRender	RRID:SCR_018361
Adobe Illustrator	Adobe	RRID:SCR_010279
Prism 9	Graphpad	RRID:SCR_002798
BioTek Gen5	Agilent	RRID:SCR_017317

3.6 – FIGURES

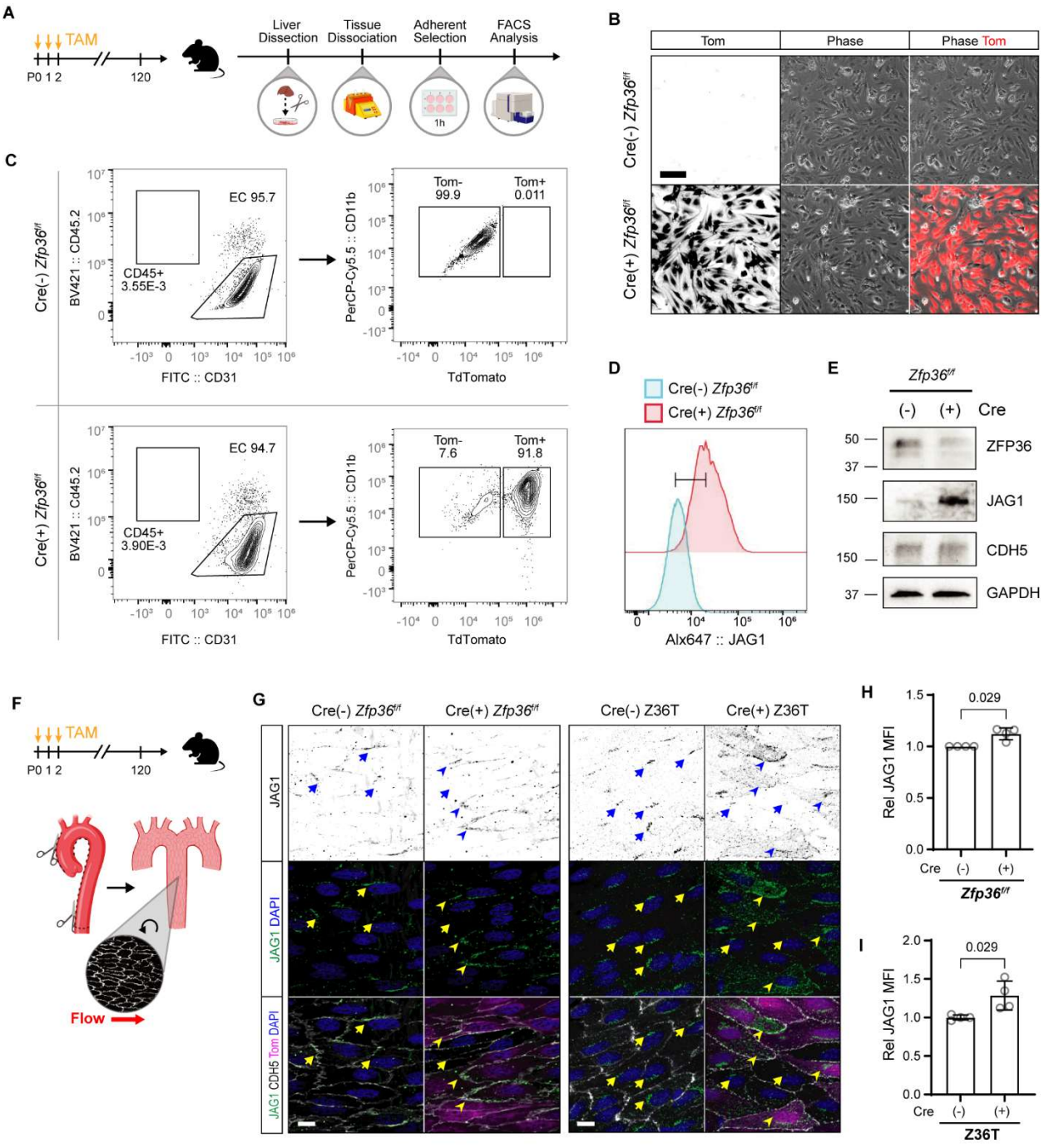

Figure 3.1 - Deletion of zfp36 in the endothelium increases Jag1 expression *in vivo*.

(A) Experimental design for isolation of endothelial cells from tamoxifen-fed inducible *Cdh5*-Cre *Zfp36*$^{f/f}$ TdTomato (Tom) reporter mice. **(B)** Representative Tom fluorescence and phase images from selected liver ECs in culture (scale bar = 100 μm). **(C)** Flow cytometry gating strategy and analysis of liver ECs. **(D)** Flow cytometry analysis of surface Jag1 expression from Cre(-),Tom(-)

ECs and Cre(+),Tom(+) ECs gated from experiment shown in panel C. Y-axis represents normalized (relative to mode) cell numbers. **(E)** Immunoblot of Zfp36, Jag1, VECAD, and GAPDH from EC lysates. **(F)** Schematic of aortic dissection for en face immunohistochemistry. **(G)** Representative immunohistochemistry of JAG1, VECAD, and DAPI from TAM fed *Cdh5*-Cre *zfp36*$^{f/f}$ TdTomato mice and from *Cdh5*-Cre triple zfp36$^{f/f}$*l1*$^{f/f}$*l2*$^{f/f}$ (Z36T) TdTomato mice, as indicated (scale bars = 10 μm). Tom signal indicates recombination of the reporter in respective cells. Several areas of positive fluorescent signal are marked on Tom(-) (arrows) and Tom(+) (arrowheads) cells. **(H)** Quantification of Jag1 mean fluorescent intensity (MFI) ± SD from TAM fed *Cdh5*-Cre *zfp36*$^{f/f}$ TdTomato mice averaged from a minimum of 2 fields of view per animal (n = 4). For Cre(+) animals only Tom(+) cell area were measured. Statistics: Mann Whitney test. **(I)** Quantification of JAG1 MFI ± SD from TAM fed *Cdh5*-Cre triple zfp36$^{f/f}$*l1*$^{f/f}$*l2*$^{f/f}$ (Z36T) TdTomato mice averaged from a minimum of 2 fields of view per animal (n=4). For Cre(+) animals only Tom(+) cell area were measured. Statistics: Mann Whitney test.

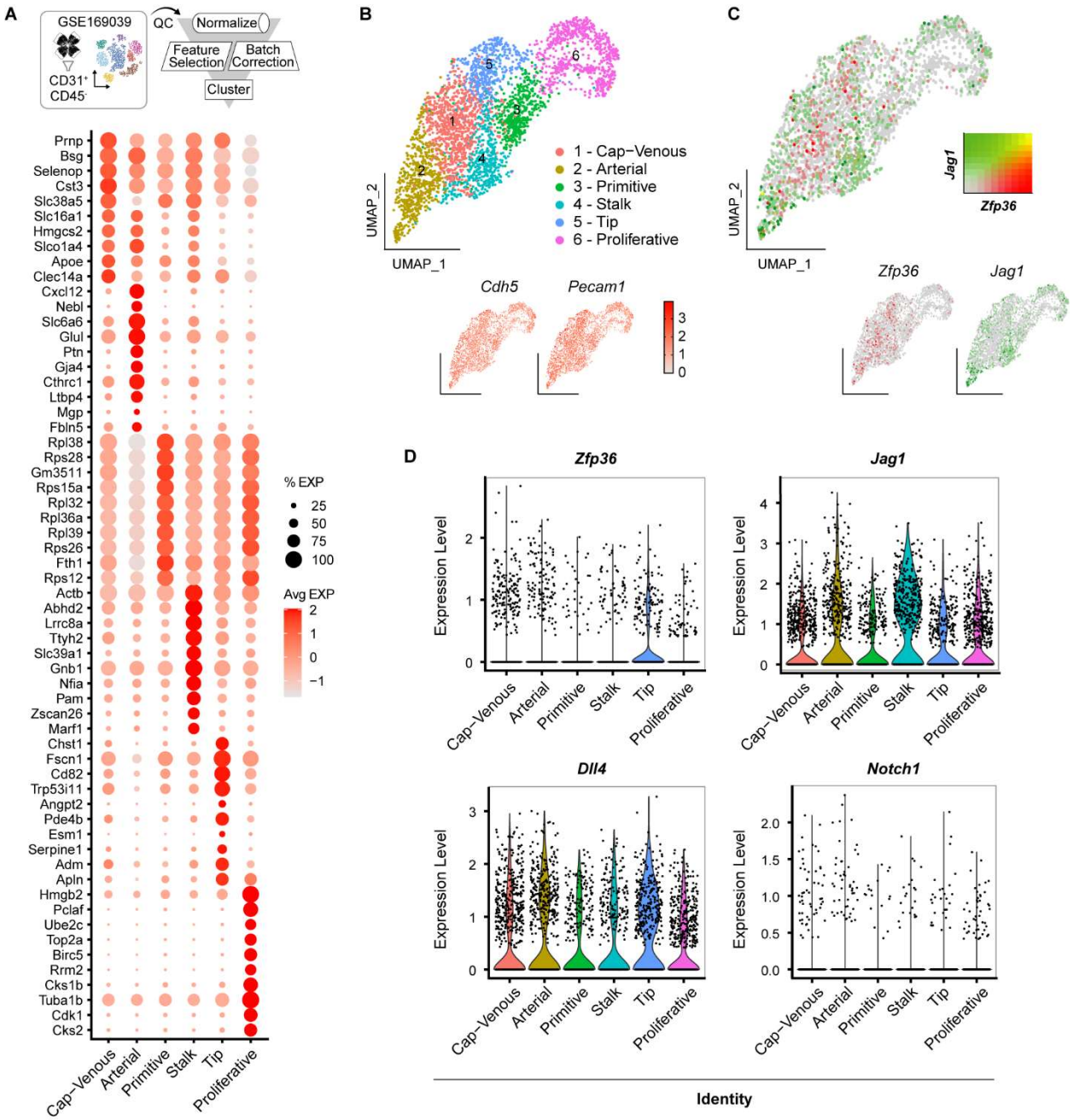

Figure 3.2 – scRNAseq of retinal ECs showed enrichment of *Zfp36* in tip cell population.

(A) Schematic of data processing from publicly available scRNAseq from CD31 enriched p6 and p10 WT retina (GSE169039) with corresponding dot plot for identification of endothelial clusters. **(B)** UMAP cluster analysis of EC identity and endothelial markers *Cdh5* and *Pecam1*. **(J)** Relative individual *Zfp36* (red) and *Jag1* (green) expression in endothelial clusters with corresponding feature blended UMAP. **(C)** Violin plots showing *Zfp36*, *Jag1*, *Dll4*, and *Notch1* transcripts in respective cell clusters.

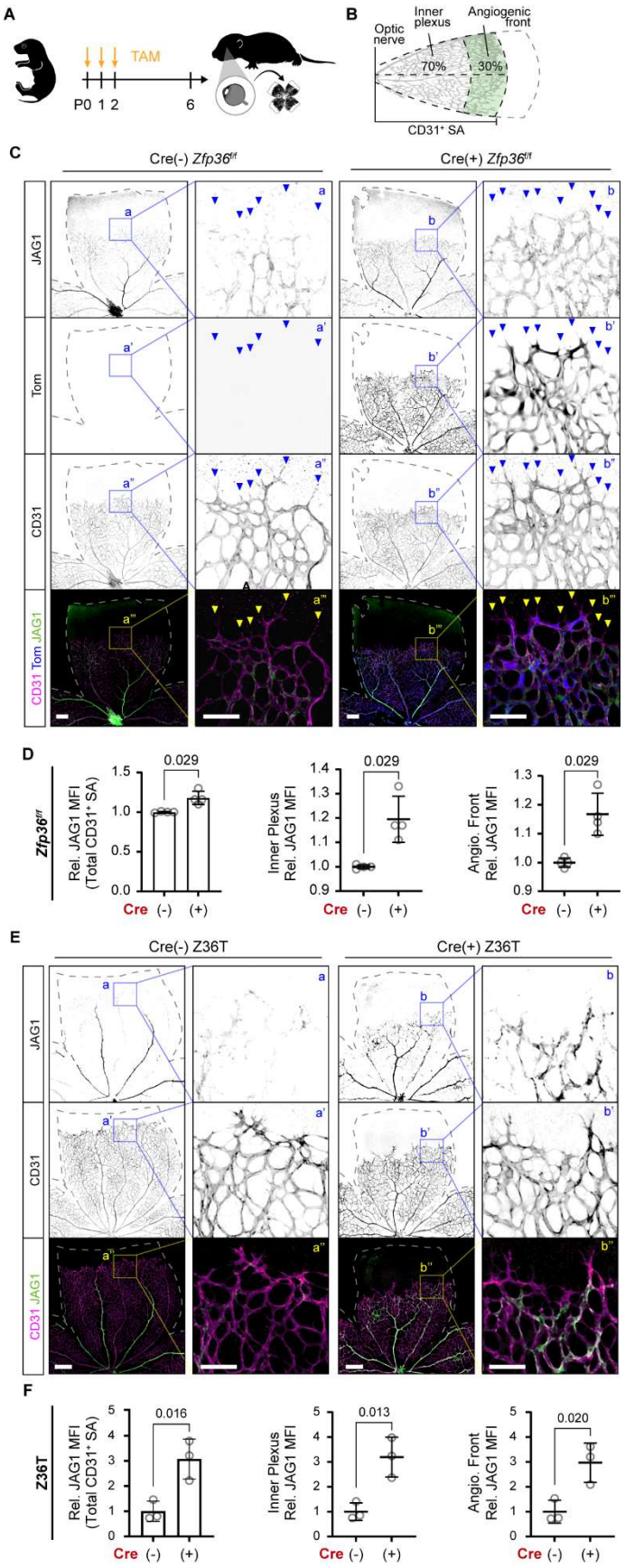
A
TAM
P0 1 2
6
B
Optic nerve
Inner plexus
Angiogenic front
70%
30%
CD31+ SA
C
Cre(-) Zfp36f/f
Cre(+) Zfp36f/f
JAG1
Tom
CD31
CD31 Tom JAG1
D
Zfp36f/f
Rel. JAG1 MFI (Total CD31+ SA)
Inner Plexus Rel. JAG1 MFI
Angio. Front Rel. JAG1 MFI
0.029
Cre (-) (+)
E
Cre(-) Z36T
Cre(+) Z36T
CD31 JAG1
F
Z36T
0.016
0.013
0.020

Figure 3.3 - Deletion of Zfp36 in the endothelium increases Jag1 expression in the developing retina vascular plexus.

(A) Schematic of TAM feeding and post-natal retina harvest. **(B)** Schematic for quantification of JAG1 mean fluorescence intensity using $CD31^+$ surface area (SA) mask. This area was further subdivided to inner plexus and angiogenic front regions based $CD31^+$ SA convex hull area percentages as indicated. **(C)** Representative JAG1, tdTom, and CD31 immunohistochemistry of TAM fed inducible *Cdh5*-Cre *Zfp36*$^{f/f}$ tdTom reporter mice. Dashed lines outline retina area and arrows indicate angiogenic sprouts (low magnification scale bar = 200 μm; zoom scale bar = 100 μm). **(D)** Quantification of JAG1 MFI ± SD within total CD31+ SA, inner plexus, and angiogenic front of TAM fed inducible *Cdh5*-Cre *Zfp36*$^{f/f}$ mice relative to respective littermate cre(-) controls (n = 4 replicates each; comparisons from 3 independent litters). Statistics: Mann-Whitney test. **(E)** Representative Jag1 and CD31 immunohistochemistry of TAM fed inducible triple CDH5-Cre *Zfp36*$^{f/f}$*I1*$^{f/f}$*I2*$^{f/f}$ (Z36T) mice. Dashed lines outline retina area (low magnification scale bar = 300 μm; zoom scale bar = 100 μm). **(F)** Quantification of Jag1 MFI ± SD within CD31+ area inner plexus, and angiogenic front from experimental and control littermates (n = 3 animals each). Statistics: unpaired two-tailed t-test.

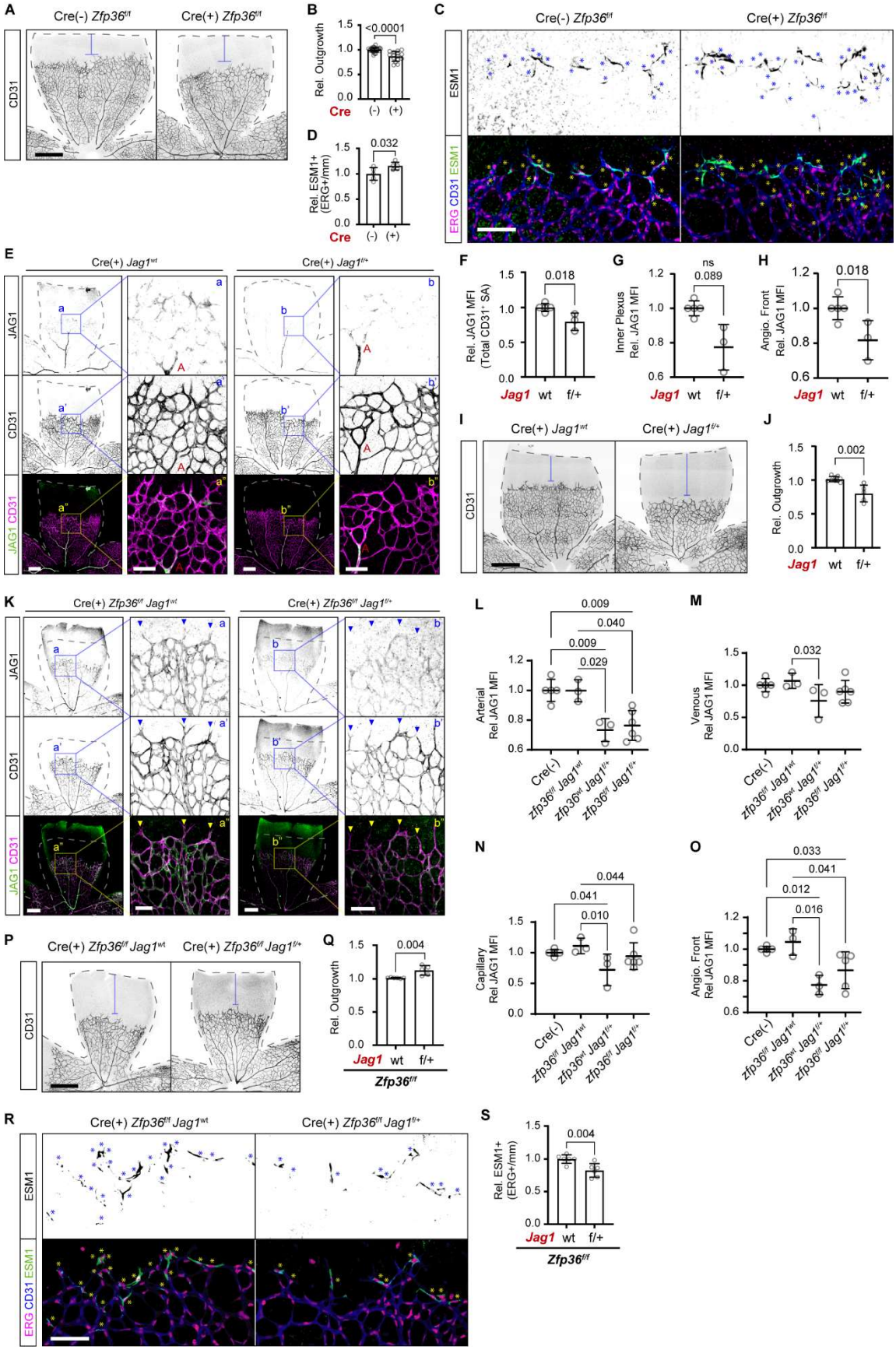
A
Cre(-) Zfp36f/f
Cre(+) Zfp36f/f
CD31
B
Rel. Outgrowth
<0.0001
Cre
(-) (+)
D
Rel. ESM1+ (ERG+/mm)
0.032
C
ESM1
ERG CD31 ESM1
E
Cre(+) Jag1wt
Cre(+) Jag1f/+
JAG1
CD31
JAG1 CD31
F
Rel. JAG1 MFI (Total CD31+ SA)
0.018
Jag1 wt f/+
G
Inner Plexus Rel. JAG1 MFI
ns
0.089
H
Angio. Front Rel. JAG1 MFI
0.018
I
J
Rel. Outgrowth
0.002
K
Cre(+) Zfp36f/f Jag1wt
Cre(+) Zfp36f/f Jag1f/+
L
Arterial Rel JAG1 MFI
0.009
0.040
0.009
0.029
Cre(-)
zfp36f/f Jag1wt
zfp36wt Jag1f/+
zfp36f/f Jag1f/+
M
Venous Rel JAG1 MFI
0.032
N
Capillary Rel JAG1 MFI
0.044
0.041
0.010
O
Angio. Front Rel JAG1 MFI
0.033
0.041
0.012
0.016
P
Q
Rel. Outgrowth
0.004
Jag1 wt f/+
Zfp36f/f
R
S
Rel. ESM1+ (ERG+/mm)
0.004

Figure 3.4 - Increased tip cells and delayed retinal angiogenesis from endothelial Zfp36KO are rescued by Jag1 haploinsufficiency.

(A) Representative CD31 immunohistochemistry of TAM fed inducible *Cdh5*-Cre *Zfp36*$^{f/f}$ mice. Dashed lines outline retina area and blue bracket indicates angiogenic outgrowth based on remaining retina area (scale bar = 500 μm). **(B)** Quantification of outgrowth (CD31+ area/total area) averaged per animal of TAM fed inducible *Cdh5*-Cre *Zfp36*$^{f/f}$ mice retina relative to average littermate control (mean ± SD; n = 22 Cre(-) *Zfp36*$^{f/f}$ & 15 Cre(+) *Zfp36*$^{f/f}$, derived from >3 independent litters). Statistics: Mann-Whitney test. **(C)** Representative CD31, ESM1, and ERG immunohistochemistry of TAM fed inducible *Cdh5*-Cre *Zfp36*$^{f/f}$ mice. Asterisks indicate ESM1+ ERG (scale bar = 100 μm). **(D)** Quantification of ESM1+ ERG normalized to width of angiogenic front (mm) of TAM fed inducible *Cdh5*-Cre *Zfp36*$^{f/f}$ mice relative to average littermate control (mean ± SD; n = 5 replicates each derived from 3 independent litters). Statistics: Mann-Whitney test. **(E)** Representative JAG1 and CD31 immunohistochemistry of TAM fed inducible CDH5-Cre(+) *Jag1*^{wt} and *Jag1*$^{f/+}$ mice. Dashed lines outline retina area with artery (A) labeled (low magnification scale bar = 300 μm; zoom scale bar = 100 μm). **(F-H)** Quantification of JAG1 MFI ± SD within total CD31+ SA **(F)**, inner plexus **(G)**, and angiogenic front **(H)** in TAM fed inducible CDH5-Cre(+) *Jag1*^{wt} and *Jag1*$^{f/+}$ mice (mean ± SD, n = 5 and 3 respectively). Statistics: Mann-Whitney test. **(I)** Representative CD31 immunohistochemistry of TAM fed inducible CDH5-Cre(+) *Jag1*^{wt} and *Jag1*$^{f/+}$ mice. Dashed lines outline retina area and blue bracket indicates angiogenic outgrowth based on remaining retina area (scale bar = 300 μm). **(J)** Quantification of outgrowth (CD31+ area/total area) per retina of TAM fed inducible CDH5-Cre(+) *Jag1*^{wt} and *Jag1*$^{f/+}$ mice (mean ± SD, n = 5 and 3 respectively). Statistics: Mann-Whitney test. **(K)** Representative JAG1 and CD31 IHC of TAM fed inducible CDH5-Cre(+) *Zfp36*$^{f/f}$ mice with either *Jag1*^{wt} or *Jag1*$^{f/+}$ alleles. Dashed lines outline retina area (low magnification scale bar = 300 μm; zoom scale bar = 100 μm). **(L-O)** Quantification of JAG1 MFI ± SD within CD31+ SA subdivided by arterial **(L)**, Venous **(M)** or capillary **(N)** specific regions from inner plexus in addition to angiogenic front **(O)** in TAM fed inducible CDH5-Cre(+) *Zfp36*$^{f/f}$*Jag1*^{wt}, *Zfp36*^{wt}*Jag1*$^{f/+}$, *Zfp36*$^{f/f}$*Jag1*$^{f/+}$ mice relative to littermate Cre(-) controls (n = 3, 3, 5, and 5 animals respectively; derived from 4 independent litters). Statistics: Mann-Whitney test and Kruskal-Wallis with post-hoc uncorrected Dunn's test. **(P)** Representative CD31 immunohistochemistry of TAM fed inducible *Cdh5*-Cre(+) *Zfp36*$^{f/f}$ mice with either *Jag1*^{wt} or *Jag1*$^{f/+}$ alleles. Dashed lines outline retina area and blue bracket indicates angiogenic outgrowth based on remaining retina area (scale bar = 500 μm). **(Q)** Quantification of outgrowth (CD31+ area/total area) averaged per animal of TAM fed inducible *Cdh5*-Cre *Zfp36*$^{f/f}$ mice either *Jag1*^{wt} or *Jag1*$^{f/+}$ retina relative to average littermate control (mean ± SD; n = 6 *Jag1*^{wt}

& 5 *Jag1*$^{f/+}$; derived from 4 independent litters). Statistics: Mann-Whitney test. **(R)** Representative CD31, ESM1, and ERG immunohistochemistry of TAM fed inducible *Cdh5*-Cre(+) *Zfp36*$^{f/f}$ mice with either *Jag1*^{wt} or *Jag1*$^{f/+}$ alleles. Asterisks indicate ESM1+ ERG (scale bar = 100 µm). **(S)** Quantification of ESM1+ ERG of TAM fed inducible *Cdh5*-Cre *Zfp36*$^{f/f}$ mice retina with either *Jag1*^{wt} or *Jag1*$^{f/+}$ alleles normalized to width of angiogenic front (mm) relative to average littermate control (mean ± SD; n = 7 replicates each, derived from 4 independent litters). Statistics: Mann-Whitney test.

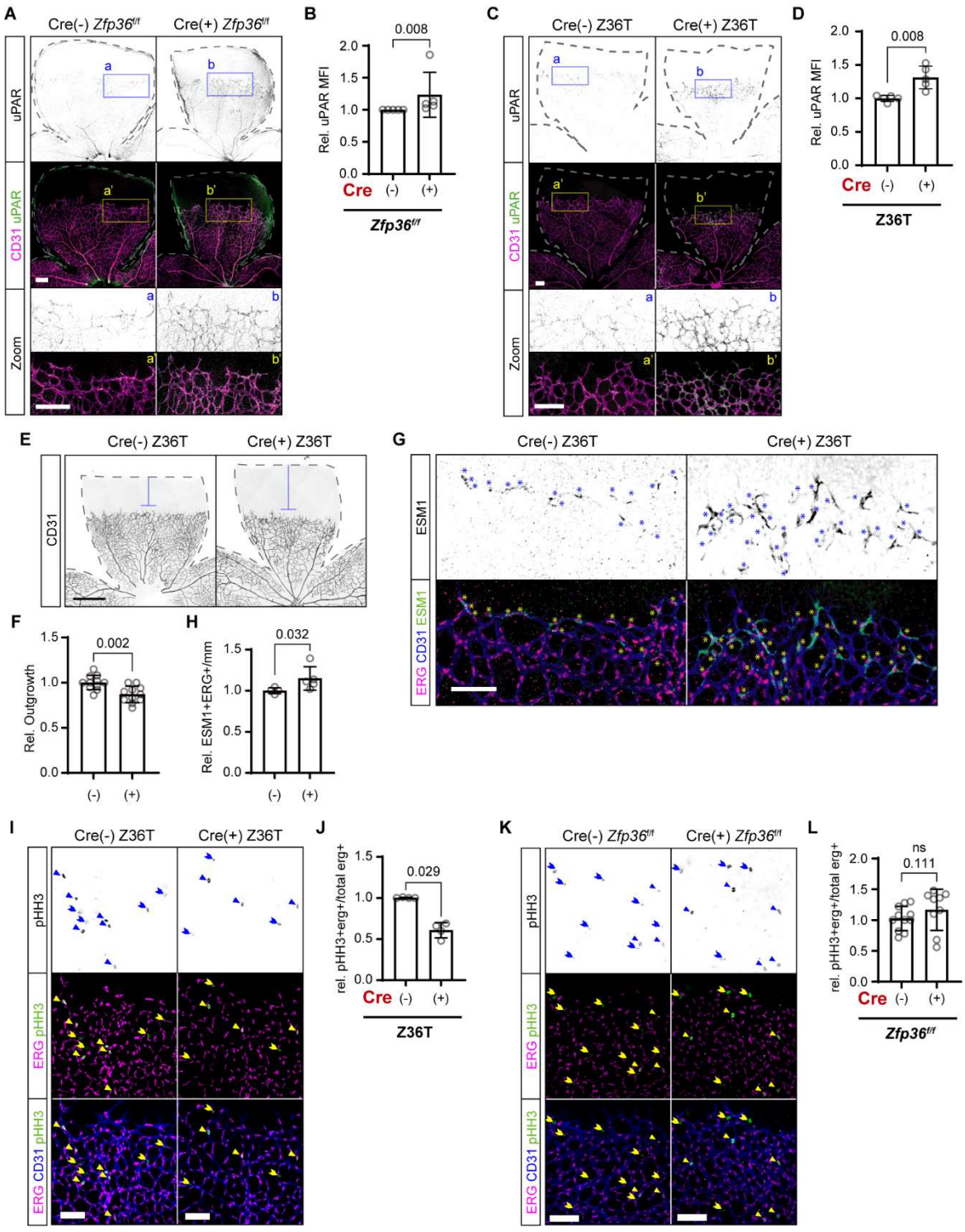

Supplemental Figure 3.1 - Increased severity of ZFP family member triple EC-KO involves additional changes in cell cycle.

(A) Representative uPAR and CD31 IHC of TAM fed inducible *Cdh5*-Cre *Zfp36*$^{f/f}$ mice. Dashed lines outline retina area (low magnification scale bar = 200 μm; zoom scale bar = 100 μm). **(B)**

Quantification of uPAR MFI ± SD within CD31+ area of TAM fed inducible *Cdh5*-Cre *Zfp36*$^{f/f}$ mice relative to respective littermate Cre(-) controls (n = 5 replicates each; pairs from 5 independent litters). Statistical analysis was performed using Mann-Whitney test. **(C)** Representative uPAR and CD31 IHC of TAM fed Z36T mice. Dashed lines outline retina area (low magnification scale bar = 300 μm; zoom scale bar = 100 μm). **(D)** Quantification of uPAR MFI ± SD within CD31+ area of TAM fed Z36T mice relative to respective littermate Cre(-) controls (n = 4 animals each). Statistical analysis was performed using Mann-Whitney test. **(E)** Representative CD31 IHC of TAM fed Z36T mice. Dashed lines outline retina area and blue bracket indicates angiogenic outgrowth based on remaining retina area (scale bar = 500 μm). **(F)** Quantification of outgrowth (CD31+ area/total area) averaged per animal of TAM Z36T mice retina relative to average littermate control (mean ± SD; n = 11 animals each, derived from 5 independent litters). **(G)** Representative CD31, ESM1, and ERG immunohistochemistry of TAM fed Z36T mice. Asterisks indicate ESM1+ ERG (scale bar = 100 μm). **(H)** Quantification of ESM1+ ERG normalized to width of angiogenic front (mm) of TAM fed Z36T mice relative to average littermate control (mean ± SD; n = 4 Cre(-) and 5 Cre(+) animals, derived from 3 independent litters). **(I)** Representative IHC of pHH3, ERG, and CD31 from TAM fed Z36T mice. pHH3^{+}ERG^{+}(arrowheads) and pHH3^{+}ERG^{-} (chevrons) are indicated (scale bar = 100 μm). **(J)** Quantification of pHH3^{+} ERG normalized to total ERG of TAM fed Z36T mice relative to average littermate control (mean ± SD; n = 4 animals each, derived from 3 independent litters). Statistical analysis was performed using Mann-Whitney test. **(K)** Representative IHC of pHH3, ERG, and CD31 from TAM fed CDH5-Cre *zfp36*$^{f/f}$ mice. pHH3^{+}ERG^{+}(arrowheads) and pHH3^{+}ERG^{-} (chevrons) cells are indicated (scale bar = 100 μm). **(L)** Quantification of pHH3^{+} ERG normalized to total ERG of TAM fed CDH5-Cre *zfp36*$^{f/f}$ mice relative to average littermate control (mean ± SD; n = 11 Cre(-) and 9 Cre(+) animals, derived from >3 independent litters). Statistical analysis performed using Mann-Whitney test.

3.7 REFERENCES

1. Rappl, P., Brüne, B., and Schmid, T. (2021). Role of tristetraprolin in the resolution of inflammation. Biology (Basel) 10. 10.3390/biology10010066.

2. Stahl, A., Connor, K.M., Sapieha, P., Chen, J., Dennison, R.J., Krah, N.M., Seaward, M.R., Willett, K.L., Aderman, C.M., Guerin, K.I., et al. (2010). The mouse retina as an angiogenesis model. Invest. Ophthalmol. Vis. Sci. 51, 2813–2826. 10.1167/iovs.10-5176.

3. Zarkada, G., Howard, J.P., Xiao, X., Park, H., Bizou, M., Leclerc, S., Künzel, S.E., Boisseau, B., Li, J., Cagnone, G., et al. (2021). Specialized endothelial tip cells guide neuroretina vascularization and blood-retina-barrier formation. Dev. Cell 56, 2237-2251.e6. 10.1016/j.devcel.2021.06.021.

4. Chavkin, N.W., Genet, G., Poulet, M., Jeffery, E.D., Marziano, C., Genet, N., Vasavada, H., Nelson, E.A., Acharya, B.R., Kour, A., et al. (2022). Endothelial cell cycle state determines propensity for arterial-venous fate. Nat. Commun. 13, 5891. 10.1038/s41467-022-33324-7.

5. Al-Souhibani, N., Al-Ahmadi, W., Hesketh, J.E., Blackshear, P.J., and Khabar, K.S.A. (2010). The RNA-binding zinc-finger protein tristetraprolin regulates AU-rich mRNAs involved in breast cancer-related processes. Oncogene 29, 4205–4215. 10.1038/onc.2010.168.

6. Brash, J.T., Bolton, R.L., Rashbrook, V.S., Denti, L., Kubota, Y., and Ruhrberg, C. (2020). Tamoxifen-Activated CreERT Impairs Retinal Angiogenesis Independently of Gene Deletion. Circ. Res. 127, 849–850. 10.1161/CIRCRESAHA.120.317025.

7. Hofmann, J.J., and Luisa Iruela-Arispe, M. (2007). Notch expression patterns in the retina: An eye on receptor-ligand distribution during angiogenesis. Gene Expr. Patterns 7, 461–470. 10.1016/j.modgep.2006.11.002.

8. Briot, A., Civelek, M., Seki, A., Hoi, K., Mack, J.J., Lee, S.D., Kim, J., Hong, C., Yu, J., Fishbein, G.A., et al. (2015). Endothelial NOTCH1 is suppressed by circulating lipids and antagonizes inflammation during atherosclerosis. J. Exp. Med. 212, 2147–2163. 10.1084/jem.20150603.

9. High, F.A., Lu, M.M., Pear, W.S., Loomes, K.M., Kaestner, K.H., and Epstein, J.A. (2008). Endothelial expression of the Notch ligand Jagged1 is required for vascular smooth muscle development. Proc Natl Acad Sci USA 105, 1955–1959. 10.1073/pnas.0709663105.

10. Manderfield, L.J., High, F.A., Engleka, K.A., Liu, F., Li, L., Rentschler, S., and Epstein, J.A. (2012). Notch activation of Jagged1 contributes to the assembly of the arterial wall. Circulation 125, 314–323. 10.1161/CIRCULATIONAHA.111.047159.

11. Breikaa, R.M., Denman, K., Ueyama, Y., McCallinhart, P.E., Khan, A.Q., Agarwal, G., Trask, A.J., Garg, V., and Lilly, B. (2022). Loss of Jagged1 in mature endothelial cells causes vascular dysfunction with alterations in smooth muscle phenotypes. Vascul. Pharmacol. 145, 107087. 10.1016/j.vph.2022.107087.

12. Rocha, S.F., Schiller, M., Jing, D., Li, H., Butz, S., Vestweber, D., Biljes, D., Drexler, H.C.A., Nieminen-Kelhä, M., Vajkoczy, P., et al. (2014). Esm1 modulates endothelial tip cell behavior and vascular permeability by enhancing VEGF bioavailability. Circ. Res. 115, 581–590. 10.1161/CIRCRESAHA.115.304718.

13. Tung, J.J., Tattersall, I.W., and Kitajewski, J. (2012). Tips, stalks, tubes: notch-mediated cell fate determination and mechanisms of tubulogenesis during angiogenesis. Cold Spring Harb. Perspect. Med. 2, a006601. 10.1101/cshperspect.a006601.

14. Benedito, R., and Hellström, M. (2013). Notch as a hub for signaling in angiogenesis. Exp. Cell Res. 319, 1281–1288. 10.1016/j.yexcr.2013.01.010.

15. Mack, J.J., and Iruela-Arispe, M.L. (2018). NOTCH regulation of the endothelial cell phenotype. Curr. Opin. Hematol. 25, 212–218. 10.1097/MOH.0000000000000425.

16. Caolo, V., van den Akker, N.M.S., Verbruggen, S., Donners, M.M.P.C., Swennen, G., Schulten, H., Waltenberger, J., Post, M.J., and Molin, D.G.M. (2010). Feed-forward signaling by membrane-bound ligand receptor circuit: the case of NOTCH DELTA-like 4 ligand in endothelial cells. J. Biol. Chem. 285, 40681–40689. 10.1074/jbc.M110.176065.

17. Leslie, J.D., Ariza-McNaughton, L., Bermange, A.L., McAdow, R., Johnson, S.L., and Lewis, J. (2007). Endothelial signalling by the Notch ligand Delta-like 4 restricts angiogenesis. Development 134, 839–844. 10.1242/dev.003244.

18. Dou, G.-R., Wang, Y.-C., Hu, X.-B., Hou, L.-H., Wang, C.-M., Xu, J.-F., Wang, Y.-S., Liang, Y.-M., Yao, L.-B., Yang, A.-G., et al. (2008). RBP-J, the transcription factor downstream of Notch receptors, is essential for the maintenance of vascular homeostasis in adult mice. FASEB J. 22, 1606–1617. 10.1096/fj.07-9998com.

19. Phng, L.-K., Potente, M., Leslie, J.D., Babbage, J., Nyqvist, D., Lobov, I., Ondr, J.K., Rao, S., Lang, R.A., Thurston, G., et al. (2009). Nrarp coordinates endothelial Notch and Wnt signaling to control vessel density in angiogenesis. Dev. Cell 16, 70–82. 10.1016/j.devcel.2008.12.009.

20. Mack, J.J., Mosqueiro, T.S., Archer, B.J., Jones, W.M., Sunshine, H., Faas, G.C., Briot, A., Aragón, R.L., Su, T., Romay, M.C., et al. (2017). NOTCH1 is a mechanosensor in adult arteries. Nat. Commun. 8, 1620. 10.1038/s41467-017-01741-8.

21. Shah, A.V., Birdsey, G.M., Peghaire, C., Pitulescu, M.E., Dufton, N.P., Yang, Y., Weinberg, I., Osuna Almagro, L., Payne, L., Mason, J.C., et al. (2017). The endothelial transcription factor ERG mediates Angiopoietin-1-dependent control of Notch signalling and vascular stability. Nat. Commun. 8, 16002. 10.1038/ncomms16002.

22. Hofmann, J.J., and Iruela-Arispe, M.L. (2007). Notch signaling in blood vessels: who is talking to whom about what? Circ. Res. 100, 1556–1568. 10.1161/01.RES.0000266408.42939.e4.

23. Desroches-Castan, A., Cherradi, N., Feige, J.-J., and Ciais, D. (2011). A novel function of Tis11b/BRF1 as a regulator of Dll4 mRNA 3'-end processing. Mol. Biol. Cell 22, 3625–3633. 10.1091/mbc.E11-02-0149.

24. Hellström, M., Phng, L.-K., Hofmann, J.J., Wallgard, E., Coultas, L., Lindblom, P., Alva, J., Nilsson, A.-K., Karlsson, L., Gaiano, N., et al. (2007). Dll4 signalling through Notch1 regulates formation of tip cells during angiogenesis. Nature 445, 776–780. 10.1038/nature05571.

25. Suchting, S., Freitas, C., le Noble, F., Benedito, R., Bréant, C., Duarte, A., and Eichmann, A. (2007). The Notch ligand Delta-like 4 negatively regulates endothelial tip cell formation and vessel branching. Proc Natl Acad Sci USA 104, 3225–3230. 10.1073/pnas.0611177104.

26. Pitulescu, M.E., Schmidt, I., Giaimo, B.D., Antoine, T., Berkenfeld, F., Ferrante, F., Park, H., Ehling, M., Biljes, D., Rocha, S.F., et al. (2017). Dll4 and Notch signalling couples sprouting angiogenesis and artery formation. Nat. Cell Biol. 19, 915–927. 10.1038/ncb3555.

27. Benedito, R., Roca, C., Sörensen, I., Adams, S., Gossler, A., Fruttiger, M., and Adams, R.H. (2009). The notch ligands Dll4 and Jagged1 have opposing effects on angiogenesis. Cell 137, 1124–1135. 10.1016/j.cell.2009.03.025.

28. Kempers, L., van der Bijl, I., van Stalborch, A.-M.D., Ponsioen, B., and Margadant, C. (2021). Fast *in vitro* protocol for the visualization and quantitative high-throughput analysis of sprouting angiogenesis by confocal microscopy. STAR Protocols 2, 100690. 10.1016/j.xpro.2021.100690.

29. Sörensen, I., Adams, R.H., and Gossler, A. (2009). DLL1-mediated Notch activation regulates endothelial identity in mouse fetal arteries. Blood 113, 5680–5688. 10.1182/blood-2008-08-174508.

30. Qiu, L.-Q., Stumpo, D.J., and Blackshear, P.J. (2012). Myeloid-specific tristetraprolin deficiency in mice results in extreme lipopolysaccharide sensitivity in an otherwise minimal phenotype. J. Immunol. 188, 5150–5159. 10.4049/jimmunol.1103700.

31. Hodson, D.J., Janas, M.L., Galloway, A., Bell, S.E., Andrews, S., Li, C.M., Pannell, R., Siebel, C.W., MacDonald, H.R., De Keersmaecker, K., et al. (2010). Deletion of the RNA-binding proteins ZFP36L1 and ZFP36L2 leads to perturbed thymic development and T lymphoblastic leukemia. Nat. Immunol. 11, 717–724. 10.1038/ni.1901.

32. Lizama, C.O., Hawkins, J.S., Schmitt, C.E., Bos, F.L., Zape, J.P., Cautivo, K.M., Borges Pinto, H., Rhyner, A.M., Yu, H., Donohoe, M.E., et al. (2015). Repression of arterial genes in hemogenic endothelium is sufficient for haematopoietic fate acquisition. Nat. Commun. 6, 7739. 10.1038/ncomms8739.

33. Hao, Y., Hao, S., Andersen-Nissen, E., Mauck, W.M., Zheng, S., Butler, A., Lee, M.J., Wilk, A.J., Darby, C., Zager, M., et al. (2021). Integrated analysis of multimodal single-cell data. Cell 184, 3573-3587.e29. 10.1016/j.cell.2021.04.048.

34. Bogen, S., Pak, J., Garifallou, M., Deng, X., and Muller, W.A. (1994). Monoclonal antibody to murine PECAM-1 (CD31) blocks acute inflammation *in vivo*. J. Exp. Med. 179, 1059–1064. 10.1084/jem.179.3.1059.

35. Sörensen, I., Adams, R.H., and Gossler, A. (2009). DLL1-mediated Notch activation regulates endothelial identity in mouse fetal arteries. Blood 113, 5680–5688. 10.1182/blood-2008-08-174508.

36. Mancini, S.J.C., Mantei, N., Dumortier, A., Suter, U., MacDonald, H.R., and Radtke, F. (2005). Jagged1-dependent Notch signaling is dispensable for hematopoietic stem cell self-renewal and differentiation. Blood 105, 2340–2342. 10.1182/blood-2004-08-3207.

37. Schindelin, J., Arganda-Carreras, I., Frise, E., Kaynig, V., Longair, M., Pietzsch, T., Preibisch, S., Rueden, C., Saalfeld, S., Schmid, B., et al. (2012). Fiji: an open-source platform for biological-image analysis. Nat. Methods 9, 676–682. 10.1038/nmeth.2019.

38. Hao, Y., Hao, S., Andersen-Nissen, E., Mauck, W.M., Zheng, S., Butler, A., Lee, M.J., Wilk, A.J., Darby, C., Zager, M., et al. (2021). Integrated analysis of multimodal single-cell data. Cell 184, 3573-3587.e29. 10.1016/j.cell.2021.04.048.

39. Dobin, A., Davis, C.A., Schlesinger, F., Drenkow, J., Zaleski, C., Jha, S., Batut, P., Chaisson, M., and Gingeras, T.R. (2013). STAR: ultrafast universal RNA-seq aligner. Bioinformatics 29, 15–21. 10.1093/bioinformatics/bts635.

CHAPTER 4

4.1 INTRODUCTION

This chapter presents unpublished work that is related to additional targets of ZFP36 binding and kinase signaling involved in stabilizing ZFP36 induction. Nearly 10% of the eukaryotic genome encodes mRNA with AREs, but the presence of these motifs does not guarantee a destabilizing function.[1] Both genetic and physiological conditions will influence ARE-directed mRNA degredation. Several groups, including ours, have identified targets of ZFP36 mRNA binding with CLIP-seq experiments, particularly those involved in regulating metabolism downstream growth factor stimulation.[2-4] We have confirmed at least one of these targets enolase 2 (ENO2) shows increased abundance in the angiogenic front of retina from endothelial specific ZFP36 KO mice.[3] Glycolysis is the primary energy-producing mechanism in endothelial cells ostensibly to allow oxygen diffusion to vascularized tissues.[5] Indeed, it has been shown that a glycolytic switch occurs at the onset and is essential for transdifferentiation to endothelial lineage.[6] During angiogenesis competitive glycolysis is important in tip and stalk cell determination and can independently dictate position in the sprouting hierarchy as cells double-silenced for Notch signaling and glycolysis rate-limiting enzyme PFKB3 were less able to present as angiogenic tip cells in mosaic analysis.[7-9] However, whether glycolytic target binding or if ZFP36 regulates metabolism downstream specific VEGF stimulation in ECs has yet to be determined.

We observed previously in immunoblot analysis of ZFP36, the presence of multiple molecular weight bands, implying post-translational modifications. It has previously been reported that ZFP36 can be phosphorylated by various kinases that can affect stability and activity.[10-13] Recombinant ZFP36 was found to be a substrate for numerous kinases *in vitro* including extracellular signal-regulated kinase (ERK), cJun N-terminal kinase (JNK), Protein kinase B (AKT) and MAPK p38.[14,15] We sought to confirm phosphorylation status downstream VEGF and the effects of inhibiting VEGF-activated kinases on ZFP36 induction.

ECs are particularly sensitive to microenvironmental changes, and transcriptional drift when transitioning cells to *in vitro* conditions is well documented.[16] Analysis in CDH5-Cre *zfp36*$^{f/f}$ mice showed increased JAG1 and ENO2 at the angiogenic front, while our *in vitro ZFP36* KO HUVECs data for ENO2 are not significantly different from biological replicate matched controls. The angiogenic front is an active site for mitogenic stimulation of ECs, so it would make sense to see changes in ZFP36 targets in those areas. However, we also observed increased EC JAG1 in CDH5-Cre *zfp36*$^{f/f}$ and Z36T mice descending aorta; a canonically quiescent endothelium where theoretically there should be little ZFP36 activity. We were interested in examining whether ZFP26 expression is flow sensitive.

4.2 RESULTS

4.2.1 *ZFP36* KO does not alter early metabolic response to VEGF in ECs.

We sought to determine whether glycolytic targets are among those involved in ZFP36 mRNA mediated decay downstream VEGF stimulation of ECs. Several glycolysis pathway targets were identified in CLIP-seq analysis of Zfp36/l1/l2 triple-KO MEFs, including hexokinase 2 (HK2), glucose transporter 1 (GLUT1), 6-phosphofructo-2-kinase/fructose-2,6-bisphosphatase (PFKB3), and enolase 2 (ENO2) (Figure 4.1A). We performed VEGF stimulation and immunoblot analysis of these targets in control versus *ZFP36* KO HUVECs and observed a large amount of variability across biological replicates (Figure 4.1B-D). Additionally, the individual proteins did not correlate with each other, indicating that global changes to metabolism at this time point, at least on the protein level, appeared unchanged in response to 1 h VEGF stimulation in control and KO ECs. We did observe at least in one replicate there was a large relative increase in GLUT1 in ZFP36 KO HUVECs, however this did not correspond to similarly large increase in transcriptional changes (Figure 4.1E) nor did it correspond to large increase glucose uptake as observed through proxy fluorescence intensity of non-metabolizable 2-NBDG (Figure 4.1F). It is important to note that changes in overall glucose intake do not indicate whether the glucose is utilized or instead

stored,[17] so we performed a glycolytic activity assay in a subset of biological replicates. Similarly, we observed large variability in oxygen consumption rate (OCR), extracellular acidification rate (ECAR), and proton efflux rates (PER) between control and experimental groups across biological replicates (Figure 4.1F). This led to large variation in overall differences in metabolism in control and *ZFP36* KO ECs (Figure 4.1G-I). In the biological replicate observed to have a nearly 4-fold change of ENO2 protein (replicate 5) in ZFP36 KO ECs with 1 h VEGF stimulation, we observed a corresponding increase in overall basal glycolysis after adding mitochondrial inhibitor Rotenone/Antimycin A (Rot/AA). However, this experimental group (KO + V) in other biological replicates did not repeat this trend. The only consistent trend between all conditions was that VEGF did not significantly change the basal OCR, ECAR nor PER overtime within each sample during the 1h incubation period (Figure 4.1I).

4.2.2 Kinase inhibition changes the induction of ZFP36 in endothelial cells.

To examine the importance of various kinases to ZFP36 induction, we first confirmed the phosphorylation status. There are no available commercial phospho-ZFP36 antibodies. To circumvent this, we utilized a protein phosphatase to release phosphate groups from all phosphorylated serine, threonine, and tyrosine residues, thereby phosphorylation status can be detected via immunoblot analysis through a shift in molecular weight when using an antibody for total ZFP36. Multi-target activity is important since we were unable to identify specific phospho-sites of ZFP36 downstream 1 h VEGF stimulation. With lambda phosphatase (λ-PP) treatment of lysates from VEGF stimulated HUVECs, we observed a consistent molecular weight change of approximately 2 kDa (Figure 4.2A-C).

With confirmation that ZFP36 phosphorylation occurred during VEGF-mediated induction, we next were interested in seeing which, if any, kinases, previously reported to phosphorylate ZFP36, can modify this induction. For this we utilized several kinase inhibitors and pre-incubated for 6 h before stimulating with VEGF for 1 h (Figure 4.2D). HUVECs treated with PI3K and AKT

kinase inhibitors alone had a significant increase in ZFP36 seemingly independent of VEGF stimulation (Figure 4.2F-G). While statistically still significantly increased with VEGF stimulation, each biological replicate has different induction magnitude with VEGF stimulation, therefore the differences between VEGF stimulated experimental groups were masked by making quantification relative to vehicle treated DMSO controls (Figure 4.2G). Quantification relative to VEGF treated DMSO control revealed a significant decrease in ZFP36 protein with ERK1/2 and p38 inhibition (Figure 4.2H).

4.2.3 Shear stress *in vitro* reduces ZFP36 expression.

To analyze the effects of *in vitro* culture and flow to ZFP36 we analyzed previous published RNAseq data.[16] We observed that *ZFP36* is expressed approximately 1-fold higher in freshly isolated HUVECs compared to static cultured cells (Figure 4.3A, 4.3B). This change was only rescued in culture with short term re-exposure to orbital flow (Figure 4.3B). With longer flow exposure (8-48h) HUVECs down regulate ZFP36 expression. This decrease was confirmed at the protein level by immunoblot of Control and *ZFP36* KO HUVECs lysates harvested after 24 h orbital flow, where we observed an average 5-fold decrease in control HUVECs exposed to flow Figure 4.3C).

4.3 DISCUSSION

Endothelial cells in general are highly glycolytic. A seminal paper by De Bock et al. has shown 2h in VEGF growth medium increases radioactive [5-^{3}H]-D-glucose glycolytic flux by upregulating PFKFB3.[18] This increased glycolysis was further shown to be necessary for proper angiogenic sprouting. In our hands, we did not observe an upregulation with 1 h VEGF stimulation using ECAR as a proxy for glycolytic rate, which corresponds to the relatively stable level of glycolysis targets at the protein level. Our rationale for choosing this time point is ZFP36 induction downstream VEGF occurs at a relatively rapid rate (peak protein expression at 1h), but perhaps changes to metabolism take longer to resolve. Glycolysis is a large determinant in the shuffling of

tip and stalk cells, which on average take approximately 4 h.[8] It would be interesting to observe whether measuring glycolysis for a longer duration might resolve differences in experimental outcomes. Also, as our measurements are performed on whole cell monolayers, we are unable to discriminate between tip-like or stalk-like phenotypes and may be diluting overall relative contribution of ZFP36 to metabolic changes. *In vivo*, we were able to detect ENO2 increased in developing retina of TTP EC-KO mice, but this increase appears to be relatively concentrated at the retinal angiogenic front.[3] Models, that have isolated ECs *in vitro* based on expression of tip-cell marker CD34, have observed glycolysis is significantly lower when compared to non-tip cells.[19,20] Considering these data further reinforces the need for complementary *in vivo* work to truly grasp the contributions of each molecular player for coordinating a complicated physiological process such as angiogenesis.[21]

In addition to glucose being utilized for energy production through generation of ATP, endothelial cells undergoing activation also utilize mobilized glycolytic intermediates for other biosynthetic pathways for proliferative biomass production. For instance, the pentose phosphate pathway diverts glucose for nucleotide biosynthesis by producing intermediate ribose-5-phosphate (R5P), and for redox control during fatty acid biosynthesis through generation of NADPH. As ECs form new vessels into hypoxic tissues redox control is especially important for preventing endothelial demise.[22] Vascular maturation and mural cell recruitment have also been shown to rely on R5P mediated upregulation of elastin synthesis, though the exact molecular mechanism is currently unknown.[23] In addition, glycolytic intermediates can also be channeled to the hexosamine biosynthesis pathway, which generates carbohydrates for O- and N-glycosylation of proteins. Glycosylation has already been linked to functionality VEGFR2 and Notch1 signaling as both receptors' activity can be impacted by glycosylation status.[24-26] We did not measure these particular metabolites and therefore cannot eliminate the possibility of this alternative means for glucose utilization.

Importantly, the CLIP-seq targets examined to bind with ZFP36 were identified in the MEFs under the context of general serum stimulation. Enolase 2 is primarily expressed in neuronal lineage, whereas endothelial cells are reported to express primarily enolase 1 especially in response to oxidative stress.[27,28] Glycolysis can also differ depending on endothelial subtype, as arterial ECs can be relatively more oxidative than glycolytic microvascular ECs.[18,29] Accordingly, cell type specific features will be important to consider in pursuing future experiments regarding conserved changes in metabolism.

While metabolic targets don't seem to be replicated in our model, we do observe consistent kinase interactions. We observed that ZFP36 phosphorylation and induction dynamics appear dependent on active p38 and ERK1/2. Inversely we observed PI3K/Akt inhibition led to an increase overall amount of protein independent from VEGF stimulation. This matches with previously published data showing that akt-quiescent cells following mTOR inhibition form ZFP36:14-3-3 protein complexes, stabilizing ZFP36.[30] Serum starvation has been shown to reduce mTOR signaling, therefore the combination our experimental model of overnight starvation with AKT inhibition could explain this phenomenon.[31] Considering these significant changes in overall ZFP36 protein abundance depending on phosphorylation states, it would be interesting to test whether these correspond to altered mRNA binding/decay.

ZFP36 appears to decrease when assessing global transcriptional changes in response to *in vitro* manipulation.[16] Furthermore, this decrease was exacerbated by trying to reintroduce shear stress in culture. These differences stress the importance of validating the fidelity of *in vitro* findings with *in vivo* models. While ENO2 was observed to be increased at the retinal angiogenic front, whether this translates to overall changes in endothelial metabolism downstream VEGF mediated activation has yet to be established and would require further study.

4.4 – AUTHOR CONTRIBUTIONS

Conceptualization, HLS and MLIA; Methodology, HLS, GS; Validation, HLS; Formal Analysis, HLS; Investigation HLS; Resources AP; Writing – Original Draft, HLS; Writing – Review & Editing HLS, ACC, HRC, TAV, and MLIA; Funding Acquisition, HLS and MLIA; Supervision, HRC, TAV, and MLIA.

4.5 – METHODS

4.5.1 Resource availability

Materials used in this study are commercially available details can be found in key resource table (Table 4.1).

4.5.2 Experimental models

Endothelial cells (HUVECs, HAECs, and HDMECs) were cultured with 10% fetal bovine serum (FBS) (Omega Scientific #FB-11) in either MCDB-131 (VEC Technologies; MCDB131-WOFBS) or EBM-2 Basal Medium (Lonza; CC-3156) supplemented with 1% penicillin/streptomycin and EGM-2 supplements (Lonza; CC-4176) sans kit FBS. Cells were housed in humidified incubator at 37°C with 5% CO_2 and atmospheric oxygen.

4.5.3 Method details

Lentivirus production and infection

Lentivirus particles were produced in 293T cells by co-transfecting with a construct of interest and second-generation packaging plasmids psPAX2 and pMD2.G (Addgene; gift from Didier Trono). At 24 and 48 hours, lentivirus-rich medium was collected and pooled. After centrifuging 1250 rpm for 5 min, supernatant was filtered (0.22 μm) and aliquot for single use and frozen at -80°C for long term storage. For transduction on HUVECs, aliquots were applied directly to cells overnight in the presence of 8 μg/mL polybrene. Infected cells were cultured in regular growth medium for 48 h prior to beginning puromycin (1 mg/mL) antibiotic selection where applicable.

VEGF stimulation and inhibitor treatments

Stock recombinant Human $VEGFA_{165}$ (VEGF) (Peprotech) was prepared in sterile molecular grade water in single-use aliquots. After washing cells once with serum-free media, cells were serum starved overnight followed by direct application of DMSO vehicle control or kinase inhibitor pretreatment – SCH772984 (10 μM), SP600125 (5 μM), LY294002 (20 μM), MK-2206 (10 μM), U0126 (10 μM), or LY2228820 (10 μM). After 6 h incubation, VEGF or vehicle control was directly added for a final concentration of 100 ng/mL for 1 h before harvesting protein lysates.

Cell lysis and immunoblotting

Cells were lysed in modified RIPA buffer (50 mM Tris pH8, 150 mM NaCl, 0.5% w/v Na-Desoxycholate, 1% w/v Triton-X100, 0.1% w/v SDS, 200 μM Na_3VO_4, 1x protease inhibitor cocktail) after washing once with cold 1xPBS. Lysates were then denatured with Laemmli buffer for 10 min at 95°C. Denatured protein lysates were separated by SDS-PAGE gradient (4–20%) gel (Bio-Rad) and transferred using 20 min semi-dry transfer using Trans-blot Turbo (Bio-Rad) onto nitrocellulose membranes. Blots were ponceau stained for total protein normalization before blocking for 1 h and incubated overnight at 4°C with primary antibodies (see Key Resource Table). HRP-conjugated secondary antibodies (1:10,000) were applied in species dependent manner at room temperature for 1 h. Immuno-complexes were detected by enhanced chemiluminescence with SuperSignal™ West Pico PLUS or Femto Maximum Sensitivity Substrate (Thermo Fisher) using ChemiDoc Imaging system (Bio-Rad). Quantification of bands by densitometry analysis was performed using ImageLab Software (Bio-Rad).

Quantitative RT-PCR

Total RNA from cell culture was extracted and purified using RNeasy mini kit (Qiagen) according to manufacturer's instructions. Complementary DNA synthesis was performed with Superscript III reverse transcription First-Strand synthesis kit (Invitrogen). qPCR was performed for each sample in duplicate and gene expression was normalized with the housekeeping gene (HPRT) and

relative expression calculated using the ΔΔCt method. Primer sets were synthesized by Integrated DNA Technologies, Inc (Primer sequences listed in key resource table).

Glucose uptake assay

Confluent HUVECs were serum starved overnight in MCDB-131 without FBS. The following day, cells were washed 1x with KRH buffer then switched to phenol-free EBM (Lonza) without supplements + VEGF (100ng/mL) for 2 h before adding fluorescent d-glucose analog 2-NBDG at a final concentration of 200 μM per well.[32] After 20 min, fluorescence intensity was measured. To normalize cells were washed once with ice-cold 1xPBS and cell lysis was performed using RIPA buffer. Protein concentration was measured using Bradford Assay (Thermo Fisher) according to manufacturer's instructions.

Glycolysis assay

Control or *ZFP36* KO HUVECs were seeded at a density $2x10^4$ cells per well into gelatin-coated Seahorse XF96 culture plate (Agilent). Plate was left in biosafety hood for 1 h at room temperature to promote even cell distribution and reduce edge effects. The next day media was changed to serum free media and incubated for 5 h in humidified incubator at 37°C with 5% CO_2 before changing to assay medium and transferring to non-CO_2 incubator at 37°C for 1 h (~6h cumulative time serum free). Oxygen consumption rate (OCR), extracellular acidification rate (ECAR), and proton efflux rate (PER) were measured for three cycles (3 min mixing time directly to 3 min measurement time) for basal glycolysis, six cycles (3 min mixing time, 4 min wait time, and 3 min measurement time) post VEGF port injection (final concentration 100ng/mL) for induced glycolysis, three cycles (3 min mixing time directly to 3 min measurement time) post Rotenone/Antimycin A (Rot/AA; 500 nM), port injection, and finally five cycles (3 min mixing time directly to 3 min measurement time) post port injection of glycolysis inhibitor 2-deoxy-D glucose (2-DG; 50 mM). For normalization, CyQUANT (Thermo Fisher) assay was performed directly in XF96 culture plate to measure DNA content per well.

Lambda phosphatase treatment

Lysates protein concentration was determined by Bradford assay according to manufacturer instructions. Samples were aliquoted and diluted to the same concentration to be treated directly with or without λ-PP (400 U) for 2 h at 30°C. Afterwards, lysates were then denatured and loaded equally for western blotting.

Shear stress

HUVECs were seeded to confluence in 6-well culture plates. The following day media was changed to contain 4% dextran (w/v) and put under orbital rotation at 130 rpm or left static in a humidified incubator at 37°C with 5% CO_2 and atmospheric oxygen. Following 24 h incubation the center of each well was removed with cell scraper and washed with 1x PBS to avoid region not subjected to uniform laminar shear stress before lysis.[33]

Quantification and statistical analysis

Statistical parameters were calculated using Prism 8 (Graphpad) and are specified in figure legends. All significant results, defined as having a p-value < 0.05, are specified for each figure.

Table 4.1 Key resource table

REAGENT or RESOURCE	SOURCE	IDENTIFIER
Antibodies		
Rabbit polyclonal anti-ENO2	Cell Signaling Tech	Cat#9536; RRID: AB_2099308
Mouse monoclonal anti-GAPDH	Millipore Sigma	Cat#MAB374; RRID: AB_2107445
Rabbit polyclonal anti-GLUT1	Millipore Sigma	Cat# 07-1401 RRID: AB_11212210
Rabbit monoclonal anti-Hexokinase II	Cell Signaling Tech	Cat#2867 RRID: AB_2232946
Rabbit monoclonal anti-PFKFB3	Cell Signaling Tech	Cat#13123 RRID: AB_2617178
Rabbit monoclonal anti-phospho-VR2 (Tyr1175)	Cell Signaling Tech	Cat#2478; RRID: AB_31377
Rabbit monoclonal anti-VR2	Cell Signaling Tech	Cat#2479; RRID: AB_2212507

Rabbit monoclonal anti-ZFP36	Cell Signaling Tech	Cat#71632; RRID: AB_2799806
Bacterial and virus strains		
lentiCRISPR v2	Sanjana et al.[33]	Cat#52961; RRID:Addgene_52961
Biological samples		
Human umbilical vein endothelial cells	Lonza	Cat# C2517A; Lot# 21TL169354 (1), 21TL195719 (2), 0000632996 (3), 20TL293905 (4), 0000296747 (5)
Chemicals, peptides, and recombinant proteins		
2.5% Trypsin, 10x	Corning	Cat#MT25054CI
Puromycin	Invitrogen	Cat#ANTPR1
Polybrene	Millipore Sigma	Cat#TR-1003-G
$VEGFA_{165}$	Peprotech	Cat#100-20
2-NBDG	Cayman Chemical	Cat#110465
cOmplete™ EDTA-free Protease Inhibitor Cocktail	Sigma-Aldrich	Cat#11873580001
Triton-X100	Thermo Fisher	Cat#BP151500
Tween-20	Sigma-Aldrich	Cat#P9416
Restore™ Western Blot Stripping Buffer	Thermo Fisher	Cat#21059
Lambda Protein Phosphatase	New England Biolabs, Inc.	Cat#P0753S
SCH772984	Selleck Chemicals	Cat#S7101
SP600125	Selleck Chemicals	Cat#S1460
LY294002	MedChem Express	Cat#HY-10108
MK-2206	Selleck Chemicals	Cat#S1078
U0126	Selleck Chemicals	Cat#S1102
LY2228820	Selleck Chemicals	Cat#S1494
Dextran from *Leuconostoc* spp.	Sigma-Aldrich	Cat#31392
Critical commercial assays		
RNeasy Plus Micro Kit	Qiagen	Cat#74034
RNeasy Mini Kit	Qiagen	Cat#74104
Trans-Blot® Turbo™ RTA Midi Nitrocellulose Transfer Kit	Bio-Rad	Cat#1704271
Thermo Scientific Pierce Detergent Compatible Bradford Assay	Fisher Scientific	Cat#PI23246
CyQUANT™ Cell Proliferation Assay	Thermo Fisher	Cat#C7026
4–20% Mini-PROTEAN® TGX™ Precast Protein Gels	Bio-Rad	Cat#4561095, 4561094
Superscript™ III First-Strand Synthesis System	Invitrogen	Cat#18080051
SsoAdvanced Universal SYBR® Green Supermix	Bio-Rad	Cat#1725274
Seahorse XF Glycolytic Rate Assay Kit	Agilent	Cat#103344-100

Deposited data		
HUVEC RNAseq	Afshar et al.[16]	GSE158081
Experimental models: Cell lines		
Lenti-X 293T	Takara	Cat#632180
Oligonucleotides		
Primer: Human_*HPRT*-Forward: GCCCTGGCGTCGTGATTAGT	Mack et al.[35]	N/A
Primer: Human_*HPRT*- Reverse: AGCAAGACGTTCAGTCCTGTC	Mack et al.[35]	N/A
Primer: Human_*GLUT1* Forward: CGTAGAGTACACTGCCTGCC	This paper	N/A
Primer: Human_*GLUT1*- Reverse: CAAGTATCTCCCCAGTCCCG	This paper	N/A
gRNA *ZFP36* Forward: CACCGTGCCCGTGCCATCCGACCA	This paper	N/A
gRNA *ZFP36* Reverse: AAACTGGTCGGATGGCACGGGCAC	This paper	N/A
Recombinant DNA		
psPAX2	Addgene	Cat# 12260 RRID: Addgene_12260
pMD2.G	Addgene	Cat# 12259 RRID: Addgene_12259
Software and algorithms		
FIJI	Schindelin et al.[36]	RRID:SCR_002285
Imaris (v9.9.0)	Bitplane	RRID:SCR_007370
NIS Elements	Nikon	RRID:SCR_014329
Image Lab Software	BioRad	RRID:SCR_014210
CFX Manager (v3.1)	BioRad	RRID:SCR_017251
Seahorse Wave Desktop Software (v2.6)	Agilent	RRID:SCR_014526
BioRender	BioRender	RRID:SCR_018361
Adobe Illustrator	Adobe	RRID:SCR_010279
Prism 9	Graphpad	RRID:SCR_002798
BioTek Gen5	Agilent	RRID:SCR_017317
Other		
Agilent Seahorse XF Pro Analyzer	Agilent	Cat#S7855A
BioTek Synergy H1 Microplate Reader	Agilent	Cat#SH1M2-SN RRID:SCR_019748

4.6 FIGURES

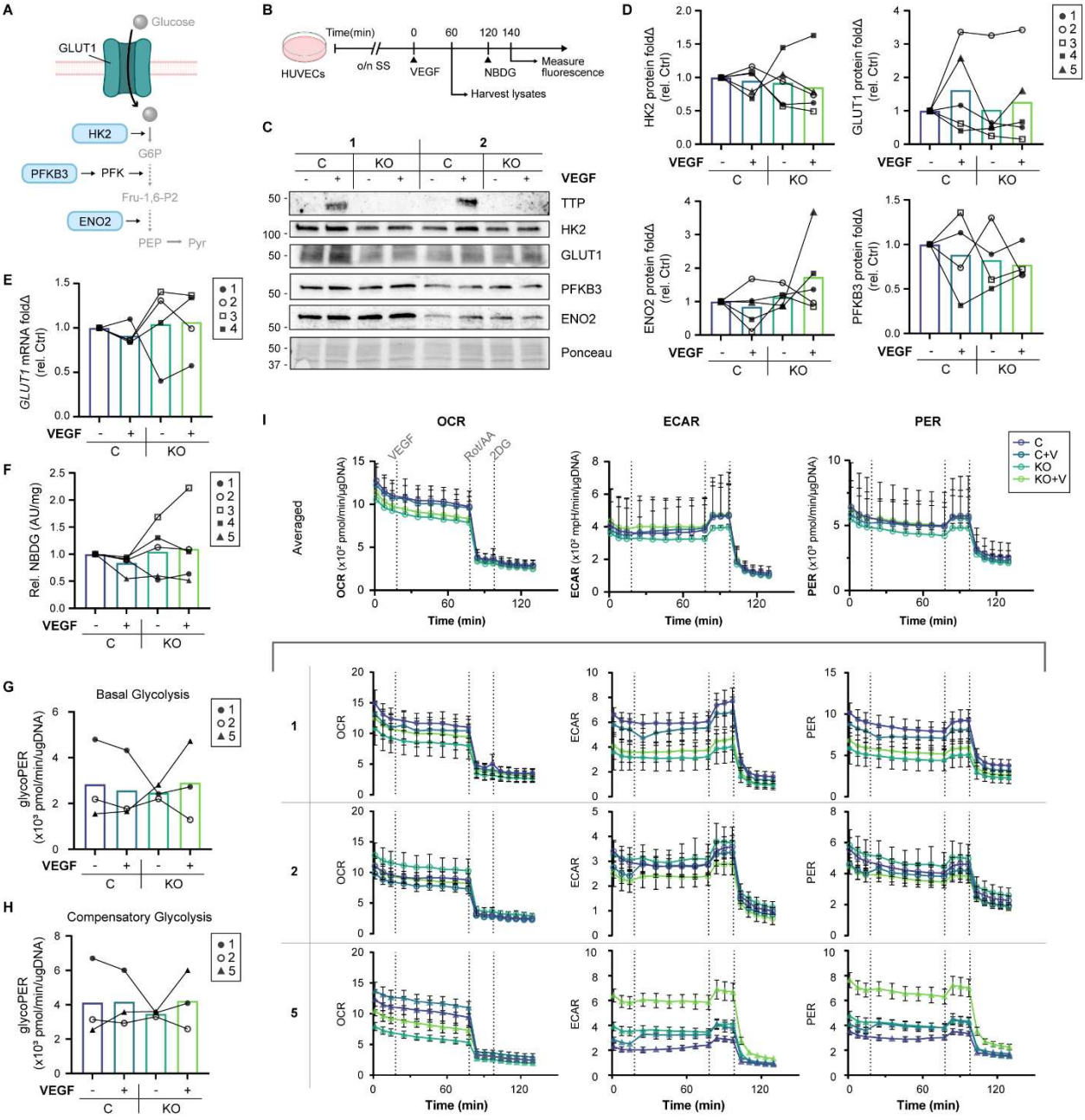

Figure 4.1 – Metabolic variability in biological replicates of *ZFP36* KO HUVECs.

(A) Targets GLUT1 and glycolytic enzymes (boxed) identified in MEF CLIP-seq data (PRJNA943291) overlayed with abbreviated glycolysis metabolites. Dashed arrows indicate there are several other metabolites that are generated in between. **(B)** Experimental design of VEGF treatment of control or *ZFP36* KO HUVECs for immunoblot analysis or NBDG uptake assay. Following overnight serum starvation lysates are harvested after 1 h of VEGF stimulation or left for an extra hour before 20 min NBDG incubation. **(C)** Representative ponceau staining and

immunoblots from two biological replicates of control or *ZFP36* KO HUVECs after 1h with or without VEGF stimulation of ZFP36, HK2, GLUT1, PFKB3, and ENO2. **(D)** Quantification of HK2, GLUT1, PFKB3, and ENO2 protein fold change (Δ) ± SD relative to vehicle treated control. Values are normalized to total protein from Ponceau staining. Mean (bar) and individual biological replicates are shown, with connecting lines for each (n = 5 biological replicates). **(E)** Quantification of *GLUT1* mRNA mean fold change (Δ) ± SD by qPCR from control and *ZFP36* KO HUVECs after 1 h with or without VEGF stimulation for normalized to *HPRT* (n = 4 biological replicates). Statistics: Kruskal-Wallis with post-hoc Dunn's multiple comparison test – NS. **(F)** Quantification of NBDG fluorescence (Mean ± SD) normalized to total protein and relative to vehicle treated control in *ZFP36* KO HUVECs treated with or without VEGF for 2 h 20 min cumulative time. Mean (bar) and individual biological replicates are shown, with connecting lines for each (n = 5 biological replicates). **(G)** Quantification of basal glycolysis and **(H)** compensatory glycolysis in control and *ZFP36* KO cells from (F). Mean (bar) and individual biological replicates are shown, with connecting lines for each (n = 3 biological replicates). Statistics run exclusively on biological replicate data sets: Kruskal-Wallis with post-hoc Dunn's tests - NS. **(I)** Quantification of oxygen consumption rate (OCR), extracellular acidification rate (ECAR), and proton efflux rate (PER) in HUVECs overtime. Vertical dashed lines indicate times of addition for VEGF (100 ng/mL), Rotenone/Antimycin A (Rot/AA; 500 nM), and 2-deoxy-D glucose (2-DG; 50 mM). Data shown are averaged values ± SD normalized to total DNA from biological replicates (n = 3), which are subdivided to each biological replicate (n = 6 technical replicates each) to show biological variability. Abbreviations: 2-(7-Nitro-2,1,3-benzoxadiazol-4-yl)-D-glucosamine (NBDG), control (C or Ctrl), *ZFP36* KO (KO) hexokinase 2 (HK2), glucose transporter 1 (GLUT1), 6-phosphofructo-2-kinase/fructose-2,6-bisphosphatase (PFKB3), enolase 2 (ENO2). HUVEC lots tested: 21TL169354 (1), 21TL195719 (2), 0000632996 (3), 20TL293905 (4), 0000296747 (5).

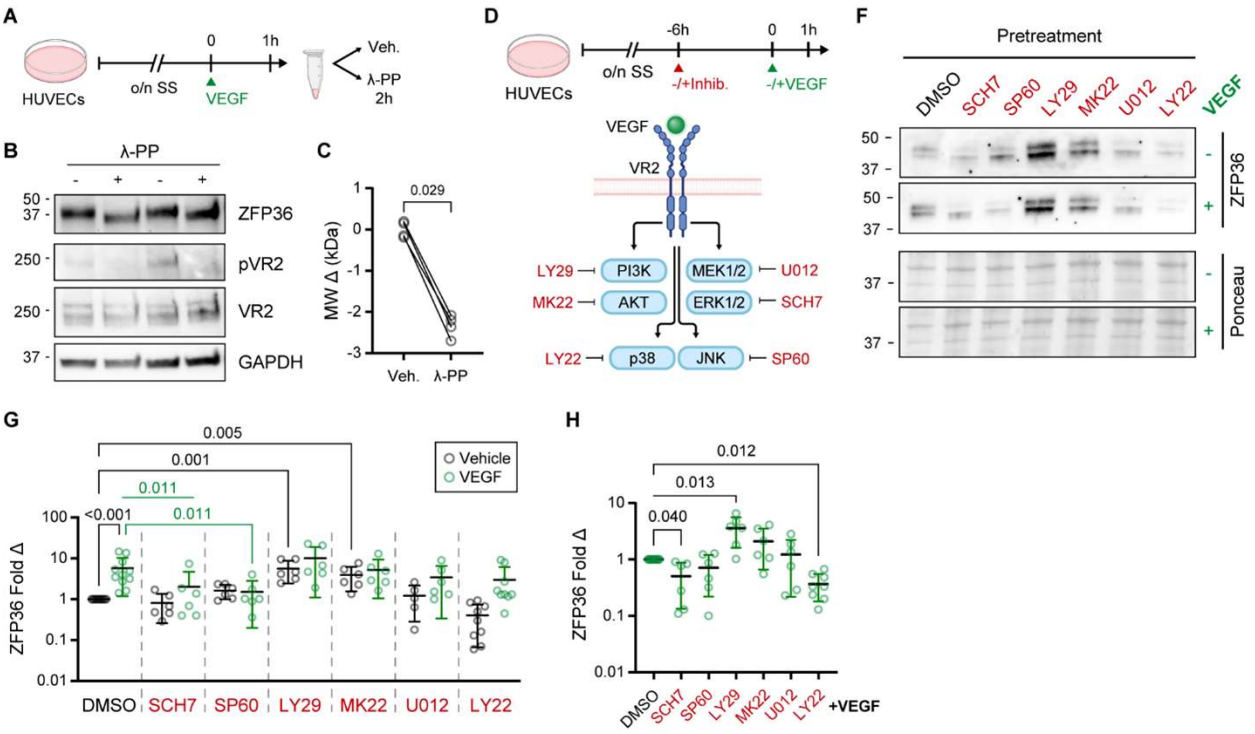

Figure 4.2 – Extrinsic kinase activity impacts endothelial ZFP36 expression.

(A) Experimental design of lambda phosphatase (λ-PP) treatment of HUVEC protein lysates harvested following overnight serum starvation and subsequent stimulation with VEGF for 1h. **(B)** Representative immunoblots of ZFP36, phospho-VEGFR2 (pVR2), VEGFR2 (VR2), and GAPDH from HUVEC lysates harvested and treated with λ-PP (n = 2 technical replicates). **(C)** Quantification of ZFP36 molecular weight (MW) change (Δ) with λ-PP treatment of lysates. Data shown as individual replicates with connecting line between matched samples (n = 4 technical replicates). Statistics: Mann Whitney test. **(D)** Experimental design of kinase inhibitor experiments. HUVECs are pretreated with inhibitors or DMSO control for 6h before stimulation with VEGF for 1h and harvesting of protein lysates. Inhibitors used and their respective targets downstream VEGFR2 activation are shown in red. **(F)** Representative immunoblots of ZFP36 after kinase inhibitor experiments with corresponding Ponceau stain. **(G)** Quantification of ZFP36 protein mean fold change (Δ) ± SD relative to replicate respective DMSO and Vehicle treated lysates. Individual replicates shown for each group are normalized to total protein from Ponceau stain (n = 5-11 replicates with minimum of 4 biological replicates). Statistics: Kruskal-Wallis with post-hoc uncorrected Dunn's test. **(H)** Repeat quantification of ZFP36 protein mean fold change (Δ) ± SD relative to replicate respective DMSO and VEGF treated lysates to account for variable biological replicate sensitivity to VEGF stimulation. Individual replicates shown for each group are normalized to total protein from Ponceau stain (n = 5-11 replicates with minimum of 4 biological

replicates). Statistics: Kruskal-Wallis with post-hoc uncorrected Dunn's test. Statistics: One-way Anova with post-hoc Holm-Šídák multiple comparisons test. Abbreviations: SCH772984 (SCH7), SP600125 (SP60), LY294002 (LY29), MK-2206 (MK22), U0126 (U012), LY2228820 (LY22).

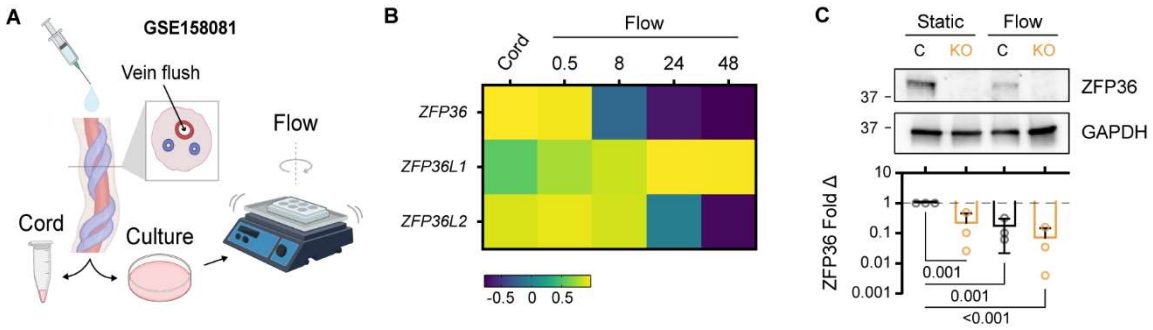

Figure 4.3 – *In vitro* shear stress reduces endothelial ZFP36 expression.

(A) Experimental design of HUVEC isolation and culture from human umbilical vein flushes previously published (GSE158081). Cord isolated HUVECs were split for direct mRNA sequencing (Cord) and for culture. HUVECs were passaged several times before submitting to shear stress using orbital shaker. **(B)** Average mRNA fold change of *ZFP36*, *ZFP36L1*, and *ZFP36L2* directly isolated cord RNA and flow treated HUVECs overtime relative to static cultured cells. **(C)** Representative immunoblots of ZFP36 and GAPDH in control and *ZFP36* KO HUVECs with or without exposure to orbital flow for 24 h, and quantification of ZFP36 protein mean fold change (Δ) ± SD relative to Control static HUVECs (n = 3 biological replicates).

4.7 REFERENCES

1. Chen, C.Y., and Shyu, A.B. (1995). AU-rich elements: characterization and importance in mRNA degradation. Trends Biochem. Sci. 20, 465–470. 10.1016/s0968-0004(00)89102-1.

2. Cook, M.E., Bradstreet, T.R., Webber, A.M., Kim, J., Santeford, A., Harris, K.M., Murphy, M.K., Tran, J., Abdalla, N.M., Schwarzkopf, E.A., et al. (2022). The ZFP36 family of RNA binding proteins regulates homeostatic and autoreactive T cell responses. Sci. Immunol. 7, eabo0981. 10.1126/sciimmunol.abo0981.

3. Cicchetto, A.C., Jacobson, E.C., Sunshine, H., Wilde, B.R., Krall, A.S., Jarrett, K.E., Sedgeman, L., Turner, M., Plath, K., Iruela-Arispe, M.L., et al. (2023). ZFP36-mediated mRNA decay regulates metabolism. Cell Rep. 42, 112411. 10.1016/j.celrep.2023.112411.

4. Matheson, L.S., Petkau, G., Sáenz-Narciso, B., D'Angeli, V., McHugh, J., Newman, R., Munford, H., West, J., Chakraborty, K., Roberts, J., et al. (2022). Multiomics analysis couples mRNA turnover and translational control of glutamine metabolism to the differentiation of the activated CD4+ T cell. Sci. Rep. 12, 19657. 10.1038/s41598-022-24132-6.

5. Rohlenova, K., Veys, K., Miranda-Santos, I., De Bock, K., and Carmeliet, P. (2018). Endothelial cell metabolism in health and disease. Trends Cell Biol. 28, 224–236. 10.1016/j.tcb.2017.10.010.

6. Lai, L., Reineke, E., Hamilton, D.J., and Cooke, J.P. (2019). Glycolytic switch is required for transdifferentiation to endothelial lineage. Circulation 139, 119–133. 10.1161/CIRCULATIONAHA.118.035741.

7. Arima, S., Nishiyama, K., Ko, T., Arima, Y., Hakozaki, Y., Sugihara, K., Koseki, H., Uchijima, Y., Kurihara, Y., and Kurihara, H. (2011). Angiogenic morphogenesis driven by dynamic and heterogeneous collective endothelial cell movement. Development 138, 4763–4776. 10.1242/dev.068023.

8. Jakobsson, L., Franco, C.A., Bentley, K., Collins, R.T., Ponsioen, B., Aspalter, I.M., Rosewell, I., Busse, M., Thurston, G., Medvinsky, A., et al. (2010). Endothelial cells dynamically compete for the tip cell position during angiogenic sprouting. Nat. Cell Biol. 12, 943–953. 10.1038/ncb2103.

9. Schoors, S., De Bock, K., Cantelmo, A.R., Georgiadou, M., Ghesquière, B., Cauwenberghs, S., Kuchnio, A., Wong, B.W., Quaegebeur, A., Goveia, J., et al. (2014). Partial and transient reduction of glycolysis by PFKFB3 blockade reduces pathological angiogenesis. Cell Metab. 19, 37–48. 10.1016/j.cmet.2013.11.008.

10. Marchese, F.P., Aubareda, A., Tudor, C., Saklatvala, J., Clark, A.R., and Dean, J.L.E. (2010). MAPKAP kinase 2 blocks tristetraprolin-directed mRNA decay by inhibiting CAF1 deadenylase recruitment. J. Biol. Chem. 285, 27590–27600. 10.1074/jbc.M110.136473.

11. Clement, S.L., Scheckel, C., Stoecklin, G., and Lykke-Andersen, J. (2011). Phosphorylation of tristetraprolin by MK2 impairs AU-rich element mRNA decay by preventing deadenylase recruitment. Mol. Cell. Biol. 31, 256–266. 10.1128/MCB.00717-10.

12. Brook, M., Tchen, C.R., Santalucia, T., McIlrath, J., Arthur, J.S.C., Saklatvala, J., and Clark, A.R. (2006). Posttranslational regulation of tristetraprolin subcellular localization and protein stability by p38 mitogen-activated protein kinase and extracellular signal-regulated kinase pathways. Mol. Cell. Biol. 26, 2408–2418. 10.1128/MCB.26.6.2408-2418.2006.

13. Deleault, K.M., Skinner, S.J., and Brooks, S.A. (2008). Tristetraprolin regulates TNF TNF-alpha mRNA stability via a proteasome dependent mechanism involving the combined action of the ERK and p38 pathways. Mol. Immunol. 45, 13–24. 10.1016/j.molimm.2007.05.017.

14. Cao, H., Dzineku, F., and Blackshear, P.J. (2003). Expression and purification of recombinant tristetraprolin that can bind to tumor necrosis factor-alpha mRNA and serve as a substrate for mitogen-activated protein kinases. Arch. Biochem. Biophys. 412, 106–120. 10.1016/s0003-9861(03)00012-2.

15. Cao, H., and Lin, R. (2008). Phosphorylation of recombinant tristetraprolin *in vitro*. Protein J. 27, 163–169. 10.1007/s10930-007-9119-7.

16. Afshar, Y., Ma, F., Quach, A., Jeong, A., Sunshine, H.L., Freitas, V., Jami-Alahmadi, Y., Helaers, R., Li, X., Pellegrini, M., et al. (2023). Transcriptional drifts associated with environmental changes in endothelial cells. eLife 12. 10.7554/eLife.81370.

17. Nakrani, M.N., Wineland, R.H., and Anjum, F. (2023). Physiology, Glucose Metabolism. In StatPearls (StatPearls Publishing).

18. De Bock, K., Georgiadou, M., Schoors, S., Kuchnio, A., Wong, B.W., Cantelmo, A.R., Quaegebeur, A., Ghesquière, B., Cauwenberghs, S., Eelen, G., et al. (2013). Role of PFKFB3-driven glycolysis in vessel sprouting. Cell 154, 651–663. 10.1016/j.cell.2013.06.037.

19. Siemerink, M.J., Klaassen, I., Vogels, I.M.C., Griffioen, A.W., Van Noorden, C.J.F., and Schlingemann, R.O. (2012). CD34 marks angiogenic tip cells in human vascular endothelial cell cultures. Angiogenesis 15, 151–163. 10.1007/s10456-011-9251-z.

20. Yetkin-Arik, B., Vogels, I.M.C., Neyazi, N., van Duinen, V., Houtkooper, R.H., van Noorden, C.J.F., Klaassen, I., and Schlingemann, R.O. (2019). Endothelial tip cells *in vitro* are less glycolytic and have a more flexible response to metabolic stress than non-tip cells. Sci. Rep. 9, 10414. 10.1038/s41598-019-46503-2.

21. Nowak-Sliwinska, P., Alitalo, K., Allen, E., Anisimov, A., Aplin, A.C., Auerbach, R., Augustin, H.G., Bates, D.O., van Beijnum, J.R., Bender, R.H.F., et al. (2018). Consensus guidelines for the use and interpretation of angiogenesis assays. Angiogenesis 21, 425–532. 10.1007/s10456-018-9613-x.

22. Ushio-Fukai, M. (2006). Redox signaling in angiogenesis: role of NADPH oxidase. Cardiovasc. Res. 71, 226–235. 10.1016/j.cardiores.2006.04.015.

23. Facchinello, N., Astone, M., Audano, M., Oberkersch, R.E., Spizzotin, M., Calura, E., Marques, M., Crisan, M., Mitro, N., and Santoro, M.M. (2022). Oxidative pentose phosphate pathway controls vascular mural cell coverage by regulating extracellular matrix composition. Nat. Metab. 4, 123–140. 10.1038/s42255-021-00514-4.

24. Potente, M., and Carmeliet, P. (2017). The link between angiogenesis and endothelial metabolism. Annu. Rev. Physiol. 79, 43–66. 10.1146/annurev-physiol-021115-105134.

25. Pandey, A., Niknejad, N., and Jafar-Nejad, H. (2021). Multifaceted regulation of Notch signaling by glycosylation. Glycobiology 31, 8–28. 10.1093/glycob/cwaa049.

26. Markowska, A.I., Jefferies, K.C., and Panjwani, N. (2011). Galectin-3 protein modulates cell surface expression and activation of vascular endothelial growth factor receptor 2 in human endothelial cells. J. Biol. Chem. 286, 29913–29921. 10.1074/jbc.M111.226423.

27. Ji, H., Wang, J., Guo, J., Li, Y., Lian, S., Guo, W., Yang, H., Kong, F., Zhen, L., Guo, L., et al. (2016). Progress in the biological function of alpha-enolase. Animal Nutrition 2, 12–17. 10.1016/j.aninu.2016.02.005.

28. Aaronson, R.M., Graven, K.K., Tucci, M., McDonald, R.J., and Farber, H.W. (1995). Non-neuronal enolase is an endothelial hypoxic stress protein. J. Biol. Chem. 270, 27752–27757.

29. Parra-Bonilla, G., Alvarez, D.F., Al-Mehdi, A.-B., Alexeyev, M., and Stevens, T. (2010). Critical role for lactate dehydrogenase A in aerobic glycolysis that sustains pulmonary microvascular endothelial cell proliferation. Am. J. Physiol. Lung Cell. Mol. Physiol. 299, L513-22. 10.1152/ajplung.00274.2009.

30. Marderosian, M., Sharma, A., Funk, A.P., Vartanian, R., Masri, J., Jo, O.D., and Gera, J.F. (2006). Tristetraprolin regulates Cyclin D1 and c-Myc mRNA stability in response to rapamycin in an Akt-dependent manner via p38 MAPK signaling. Oncogene 25, 6277–6290. 10.1038/sj.onc.1209645.

31. Pirkmajer, S., and Chibalin, A.V. (2011). Serum starvation: caveat emptor. Am J Physiol, Cell Physiol 301, C272-9. 10.1152/ajpcell.00091.2011.

32. Zou, C., Wang, Y., and Shen, Z. (2005). 2-NBDG as a fluorescent indicator for direct glucose uptake measurement. J. Biochem. Biophys. Methods 64, 207–215. 10.1016/j.jbbm.2005.08.001.

33. Warboys, C.M., Ghim, M., and Weinberg, P.D. (2019). Understanding mechanobiology in cultured endothelium: A review of the orbital shaker method. Atherosclerosis 285, 170–177. 10.1016/j.atherosclerosis.2019.04.210.

34. Sanjana, N.E., Shalem, O., and Zhang, F. (2014). Improved vectors and genome-wide libraries for CRISPR screening. Nat. Methods 11, 783–784. 10.1038/nmeth.3047.

35. Mack, J.J., Mosqueiro, T.S., Archer, B.J., Jones, W.M., Sunshine, H., Faas, G.C., Briot, A., Aragón, R.L., Su, T., Romay, M.C., et al. (2017). NOTCH1 is a mechanosensor in adult arteries. Nat. Commun. 8, 1620. 10.1038/s41467-017-01741-8.

36. Schindelin, J., Arganda-Carreras, I., Frise, E., Kaynig, V., Longair, M., Pietzsch, T., Preibisch, S., Rueden, C., Saalfeld, S., Schmid, B., et al. (2012). Fiji: an open-source platform for biological-image analysis. Nat. Methods 9, 676–682. 10.1038/nmeth.2019.

CHAPTER 5

CONCLUSION

The endothelium and its adaptive plasticity are a cornerstone of maintaining cardiovascular health. This is critical as cardiovascular complications are a key feature in numerous pathologies. My dissertation research adds another component to the complex mechanisms involved in directing endothelial activation for mounting angiogenic response.

My work directly links VEGF and Notch signaling through rapid post-transcriptional regulation. Canonical VEGF:VEGFR2 signaling potently induces transient expression of mRNA-binding protein ZFP36 in endothelial cells. Of the binding targets identified in CLIP-seq experiments we validated ZFP36 binds and regulated JAG1 expression downstream VEGF stimulation. Using *in vitro* models, we were able to confirm species conserved 3'UTR-ARE *JAG1* mRNA binding by ZFP36. As a functional consequence of upregulated JAG1 from *ZFP36* KO, endothelial cells presented an increase sprouting phenotype consistent with observed decreased Notch1 signaling. This was an important finding since otherwise cells in monolayer cultures did not display any overt changes to proliferation, migration, nor metabolism.

Critically, we validated our *in vitro* findings *in vivo*. It is well known that transcriptional drift occurs ex vivo. We've experienced this firsthand when trying to match previously published work in other cell types. Paramount to our *in vitro* findings, we observed *in vivo* a persistent phenotype of increased overall EC JAG1 expression because of endothelial specific ZFP36 KO. This increase of JAG1 leads to delayed retinal angiogenesis, a process dependent on VEGF-Notch1 cross talk. While we were unable to validate metabolic changes in response to ZFP36 ablation *in vitro* we did confirm conserved kinase regulatory activity on ZFP36 dynamics, though we did not explore downstream consequences to mRNA stability. Furthermore, we reinforce the importance of microenvironment, as reintroducing fluid flow to endothelial cells dramatically changes the transcriptional properties of endothelial cells including changes in expression of ZFP36 family members.

Our work validates that in addition to anti-inflammatory functions, ZFP36 acts as a mitogenic rheostat for rapid post-transcriptional control of transcripts with relevant functions in endothelial angiogenic response.

In summary, the information presented in this dissertation details and confirmation VEGF mediated ZFP36 interaction with JAG1 and its critical relevance to endothelial biology. With many additional potential targets for ZFP36-binding, this work will hopefully spark future examination of this potent post-transcriptional mechanism for other facets of regulating endothelial plasticity.